SANDIA REPORT
SAND2015-20818
Unlimited Release
Printed January 2015

Motion Measurement for Synthetic Aperture Radar

Armin W. Doerry

Prepared by
Sandia National Laboratories
Albuquerque, New Mexico 87185 and Livermore, California 94550

Sandia National Laboratories is a multi-program laboratory managed and operated by Sandia Corporation, a wholly owned subsidiary of Lockheed Martin Corporation, for the U.S. Department of Energy's National Nuclear Security Administration under contract DE-AC04-94AL85000.

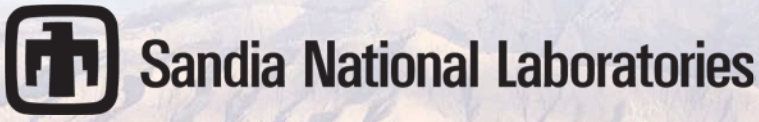

Issued by Sandia National Laboratories, operated for the United States Department of Energy by Sandia Corporation.

Available to DOE and DOE contractors from

U.S. Department of Energy
Office of Scientific and Technical Information
P.O. Box 62
Oak Ridge, TN 37831

Telephone: (865) 576-8401
Facsimile: (865) 576-5728
E-Mail: reports@adonis.osti.gov
Online ordering: http://www.osti.gov/bridge

Available to the public from

U.S. Department of Commerce
National Technical Information Service
5285 Port Royal Rd.
Springfield, VA 22161

Telephone: (800) 553-6847
Facsimile: (703) 605-6900
E-Mail: orders@ntis.fedworld.gov
Online order: http://www.ntis.gov/help/ordermethods.asp?loc=7-4-0#online

SAND2015-20818
Unlimited Release
Printed January 2015

Motion Measurement for Synthetic Aperture Radar

Armin Doerry
ISR Mission Engineering
Sandia National Laboratories
Albuquerque, NM 87185-0519

Abstract

Synthetic Aperture Radar (SAR) measures radar soundings from a set of locations typically along the flight path of a radar platform vehicle. Optimal focusing requires precise knowledge of the sounding source locations in 3-D space with respect to the target scene. Even data driven focusing techniques (i.e. autofocus) requires some degree of initial fidelity in the measurements of the motion of the radar. These requirements may be quite stringent especially for fine resolution, long ranges, and low velocities. The principal instrument for measuring motion is typically an Inertial Measurement Unit (IMU), but these instruments have inherent limited precision and accuracy. The question is "How good does an IMU need to be for a SAR across its performance space?" This report analytically relates IMU specifications to parametric requirements for SAR.

Acknowledgements

The preparation of this report is the result of an unfunded research and development activity.

Although this report is an independent effort, it draws heavily from limited-release documentation generated under a CRADA with General Atomics - Aeronautical System, Inc. (GA-ASI), and under the Joint DoD/DOE Munitions Program Memorandum of Understanding.

Sandia National Laboratories is a multi-program laboratory managed and operated by Sandia Corporation, a wholly owned subsidiary of Lockheed Martin Corporation, for the U.S. Department of Energy's National Nuclear Security Administration under contract DE-AC04-94AL85000.

Contents

Foreword

This report details the results of an academic study. It does not presently exemplify any operational systems with respect to modes, methodologies, or techniques.

Classification

The specific mathematics and algorithms presented herein do not bear any release restrictions or distribution limitations.

This distribution limitations of this report are in accordance with the classification guidance detailed in the memorandum “Classification Guidance Recommendations for Sandia Radar Testbed Research and Development”, DRAFT memorandum from Brett Remund (Deputy Director, RF Remote Sensing Systems, Electronic Systems Center) to Randy Bell (US Department of Energy, NA-22), February 23, 2004. Sandia has adopted this guidance where otherwise none has been given.

This report formalizes preexisting informal notes and other documentation on the subject matter herein.

Glossary (Acronyms)

ARW	Angle Random Walk
DGPS	Differential GPS
DOA	Direction of Arrival
EGI	Embedded GPS/INS
EKF	Extended Kalman Filter
FOG	Fiber Optic Gyro
GMTI	Ground Moving Target Indicator [Radar]
GPS	Global Positioning System
HAINS	High Accuracy INS
IMU	Inertial Measurement Unit
INS	Inertial Measurement System
IPR	Impulse Response
KF	Kalman Filter
LFM	Linear Frequency Modulation
MEMS	Micro-Electrical-Mechanical System
NED	North, East, Down [coordinate frame]
PGA	Phase Gradient Autofocus
PPM	Parts Per Million
PSD	Power Spectral Density
RLG	Ring Laser Gyro
RW	Random Walk
SAR	Synthetic Aperture Radar
VRW	Velocity Random Walk
WGN	White Gaussian Noise
2-D	2-Dimensional
3-D	3-Dimensional

1 Introduction

Synthetic Aperture Radar (SAR) is a concept whereby radar soundings at different points along a radar's flight path are coherently processed to form a radar reflectance map of the ground with much finer resolution that what is otherwise achieved from a single radar pulse.

Proper processing of the collection of radar soundings requires precise knowledge of the spatial location and orientation of the radar antenna with respect to the target scene for each and every pulse sounding. If knowledge of radar's relative position were exact, then the image could be formed with perfect focus (ignoring atmospheric effects). The challenge for SAR processing is then typically reduced to finding efficient approximations to ideal processing, but the processing is nevertheless deterministic.

The greatest challenge to an overall SAR system then is acquiring knowledge of the radar's relative position to the target scene during the data collection. This function is called Motion Measurements (MoMeas), or Navigation. Instruments that perform this function are expensive and complex. Maximal accuracy and precision needs to be measured with inherently inaccurate and imprecise instruments. This is the most difficult part of the entire SAR operation and processing.

High-performance SAR systems require high-performance motion measurement, or navigation data. Kim, et al.[1], describe the fundamental operation of navigation system used by many SAR systems designed and built by Sandia National Laboratories.

At the core of the navigation system is an Inertial Navigation System (INS), which uses an IMU. Often, additional instruments are used to aid the IMU and mitigate its weaknesses. Two basic INS configurations exist.

1. Gyro-stabilized platform INS, and
2. Strapdown INS.

We will limit our attention to strapdown INS.

Purpose of this report

The fundamental question for SAR system design is

"How good does the navigation need to be for SAR?"

This rapidly becomes the question

"How good does the IMU need to be for SAR?"

The purpose in answering these questions is to assess

1. What quality of IMU does a particular SAR system design need?

2. What is the expected SAR performance envelope for a particular IMU?

Inferring SAR performance from IMU parameters is not quite as easy as one might initially think. This report nevertheless tries to do so, but the author readily admits that a lot of hand-waving is offered along the way.

This report is intended to provide a first-cut indication of the adequacy of a particular IMU for a given application's performance space… but only a first cut… It does not purport to substitute for detailed instrument testing and validation.

Assumptions

During the discussion below we will make a number of assumptions to simplify this study. These include

- All accelerometers have essentially equal performance.

- All angular sensors have essentially equal performance.

- The quality of motion measurement is isotropic. No directions are measured with any better inherent fidelity than any other directions.

We make these assumptions to simplify our analysis, but stipulate that not all directions and rotational axes are of equal significance to the radar.

2 Inertial Measurement Basics

An IMU is an instrument designed to provide relative position and attitude information. Consequently it typically consists of

- 3 accelerometers arranged to provide orthogonal acceleration measurements to provide a 3-D acceleration vector, and
- 3 gyros arranged to provide orthogonal angular displacement (rotation) information to provide a 3-D orientation vector. More commonly, the component sensor is a 'rate gyro' that measures angular velocity instead of angular displacement itself.

Excellent discussions of inertial navigation are given by Woodman[2], and in an edited article by Kuritsky and Goldstein.[3] A good text on the subject of inertial navigation is by Titterton and Weston.[4]

With some foresight, we will initially consider two distinct coordinate frames, namely

1. The native IMU coordinate frame, and
2. The ultimate coordinate frame for which we desire motion measurements. We will call this the "radar" coordinate frame. (For the purposes of this report, the term "radar frame", or "radar coordinate frame", is merely a convenience to delineate it from the IMU coordinate frame.)

2.1 Two Dimensions

We first consider a 2-D case to establish some basic concepts. The basic configuration is shown in Figure 1.

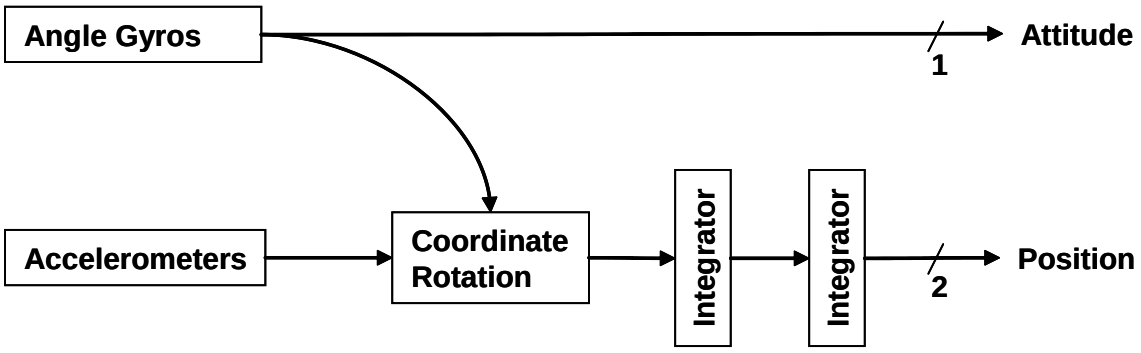

Figure 1. Simplified 2-D inertial measurement unit architecture.

In the 2-D IMU coordinate frame, defined by the x' and y' axes, we define the basic motion parameters as

$a_{x'}$ = acceleration in IMU's x' direction,
$a_{y'}$ = acceleration in IMU's y' direction, and
θ = orientation of the radar coordinate frame with respect to the IMU axis. (1)

We can rotate the accelerations to the radar coordinate frame via

$$\begin{bmatrix} a_x \\ a_y \end{bmatrix} = \begin{bmatrix} \cos\theta & \sin\theta \\ -\sin\theta & \cos\theta \end{bmatrix} \begin{bmatrix} a_{x'} \\ a_{y'} \end{bmatrix}. \tag{2}$$

In vector notation this may be written as

$$\mathbf{a} = \mathbf{R}\,\mathbf{a}' \tag{3}$$

where

$\mathbf{a} = \begin{bmatrix} a_x \\ a_y \end{bmatrix}$ = acceleration vector in radar frame,
$\mathbf{a}' = \begin{bmatrix} a_{x'} \\ a_{y'} \end{bmatrix}$ = acceleration vector in IMU frame, and
$\mathbf{R} = \begin{bmatrix} \cos\theta & \sin\theta \\ -\sin\theta & \cos\theta \end{bmatrix}$ = the rotation vector that relates the two frames. (4)

In general, $a_{x'}$, $a_{y'}$, and θ are all functions of time. Consequently, acceleration vector **a** and rotational vector **R** are also functions of time.

Acceleration is integrated to find the velocity vector, that is

$$\mathbf{v}(t) = \int_{t_0}^{t} \mathbf{a}(\tau)\,d\tau + \mathbf{v}(t_0). \tag{5}$$

Velocity is in turn integrated to find the position vector, that is

$$\mathbf{p}(t) = \int_{t_0}^{t} \mathbf{v}(\tau)\,d\tau + \mathbf{p}(t_0). \tag{6}$$

To proceed with an error analysis we distinguish between 'true' values, and 'measurement' values that are indicated from the instruments themselves. Consequently we identify

$$\begin{aligned}&\mathbf{a}_t(t) = \mathbf{R}_t(t)\mathbf{a}'_t(t) \text{ = true acceleration, based on true motion components, and}\\ &\mathbf{a}_m(t) = \mathbf{R}_m(t)\mathbf{a}'_m(t) \text{ = measured acceleration, indicated by the instruments,}\end{aligned} \tag{7}$$

where the rotation matrices are

$$\begin{aligned}&\mathbf{R}_t(t) = \begin{bmatrix} \cos\theta_t(t) & \sin\theta_t(t) \\ -\sin\theta_t(t) & \cos\theta_t(t) \end{bmatrix}, \text{ and}\\ &\mathbf{R}_m(t) = \begin{bmatrix} \cos\theta_m(t) & \sin\theta_m(t) \\ -\sin\theta_m(t) & \cos\theta_m(t) \end{bmatrix}.\end{aligned} \tag{8}$$

We generally relate measured to true accelerations as

$$\begin{aligned}&\mathbf{a}_m(t) = \mathbf{a}_t(t) + \mathbf{a}_\varepsilon(t), \text{ and}\\ &\theta_m(t) = \theta_t(t) + \theta_\varepsilon(t),\end{aligned} \tag{9}$$

where error quantities are given as

$$\begin{aligned}&\mathbf{a}_\varepsilon(t) \text{ = the error in acceleration measurements, and}\\ &\theta_\varepsilon(t) \text{ = the error in angular orientation measurement.}\end{aligned} \tag{10}$$

Without loss of generality, we may define the initial reference time as $t_0 = 0$. Consequently, the velocity vectors are specifically

$$\begin{aligned}&\mathbf{v}_t(t) = \int_0^t \mathbf{a}_t(\tau)d\tau + \mathbf{v}_t(0), \text{ and}\\ &\mathbf{v}_m(t) = \int_0^t \mathbf{a}_m(\tau)d\tau + \mathbf{v}_m(0),\end{aligned} \tag{11}$$

and the position vectors are specifically

$$\begin{aligned}&\mathbf{p}_t(t) = \int_0^t \mathbf{v}_t(\tau)d\tau + \mathbf{p}_t(0), \text{ and}\\ &\mathbf{p}_m(t) = \int_0^t \mathbf{v}_m(\tau)d\tau + \mathbf{p}_m(0).\end{aligned} \tag{12}$$

This allows the position and velocity errors to be calculated as

$$\mathbf{p}_\varepsilon(t) = \mathbf{p}_m(t) - \mathbf{p}_t(t) = \int_0^t (\mathbf{v}_m(\tau) - \mathbf{v}_t(\tau))d\tau + \mathbf{p}_\varepsilon(0), \text{ and}$$

$$\mathbf{v}_\varepsilon(t) = \mathbf{v}_m(t) - \mathbf{v}_t(t) = \int_0^t (\mathbf{a}_m(\tau) - \mathbf{a}_t(\tau))d\tau + \mathbf{v}_\varepsilon(0). \tag{13}$$

Clearly, differences between true and measured accelerations determine the ultimate range error. But the acceleration error is a function of both the IMU accelerometer values as well as the IMU's angular orientation, namely

$$\mathbf{a}_\varepsilon(t) = \mathbf{a}_m(t) - \mathbf{a}_t(t) = \mathbf{R}_m(t)\mathbf{a}'_m(t) - \mathbf{R}_t(t)\mathbf{a}'_t(t). \tag{14}$$

We further identify that the rotation matrix used in calculations is a function of the measured angular orientations, which includes any angular errors, namely

$$\mathbf{R}_m(t) = \begin{bmatrix} \cos(\theta_t(t) + \theta_\varepsilon(t)) & \sin(\theta_t(t) + \theta_\varepsilon(t)) \\ -\sin(\theta_t(t) + \theta_\varepsilon(t)) & \cos(\theta_t(t) + \theta_\varepsilon(t)) \end{bmatrix}. \tag{15}$$

For expedience, we will hereafter assume that the IMU frame is aligned with the radar frame, that is $\theta_t(t) = 0$. As a practical matter, we may also generally assume IMU instruments of sufficient quality that angular errors are small, namely

$$|\theta_\varepsilon(t)| << 1. \tag{16}$$

This allows the simplified approximation

$$\mathbf{R}_m(t) = \begin{bmatrix} \cos\theta_\varepsilon(t) & \sin\theta_\varepsilon(t) \\ -\sin\theta_\varepsilon(t) & \cos\theta_\varepsilon(t) \end{bmatrix} \approx \begin{bmatrix} 1 & \sin\theta_\varepsilon(t) \\ -\sin\theta_\varepsilon(t) & 1 \end{bmatrix} \tag{17}$$

or

$$\mathbf{R}_m(t) \approx \mathbf{I} + \begin{bmatrix} 0 & \sin\theta_\varepsilon(t) \\ -\sin\theta_\varepsilon(t) & 0 \end{bmatrix}. \tag{18}$$

Note that for the true rotation matrix,

$$\mathbf{R}_t(t) = \mathbf{I}. \tag{19}$$

Consequently, we identify and calculate rotation error matrix as

$$\mathbf{R}_{\varepsilon}(t) = (\mathbf{R}_m(t) - \mathbf{R}_t(t)) \approx \begin{bmatrix} 0 & \sin\theta_{\varepsilon}(t) \\ -\sin\theta_{\varepsilon}(t) & 0 \end{bmatrix}. \tag{20}$$

This allows us to relate the effective acceleration error as

$$\mathbf{a}_{\varepsilon}(t) = (\mathbf{I} + \mathbf{R}_{\varepsilon}(t))\mathbf{a}'_m(t) - \mathbf{a}'_t(t) \tag{21}$$

which can be expanded to

$$\mathbf{a}_{\varepsilon}(t) = \mathbf{a}'_m(t) - \mathbf{a}'_t(t) + \mathbf{R}_{\varepsilon}(t)\mathbf{a}'_m(t) \tag{22}$$

and further manipulated to

$$\mathbf{a}_{\varepsilon}(t) = \mathbf{a}'_{\varepsilon}(t) + \mathbf{R}_{\varepsilon}(t)(\mathbf{a}'_t(t) + \mathbf{a}'_{\varepsilon}(t)) \tag{23}$$

and finally to

$$\mathbf{a}_{\varepsilon}(t) = \mathbf{a}'_{\varepsilon}(t) + \mathbf{R}_{\varepsilon}(t)\mathbf{a}'_t(t) + \mathbf{R}_{\varepsilon}(t)\mathbf{a}'_{\varepsilon}(t). \tag{24}$$

After all this, some important observations include

- An acceleration error in the radar frame can be induced by instrument acceleration errors.
- An acceleration error in the radar frame can also be induced by a real acceleration with an instrument angular orientation error.
- Any acceleration error, by whatever source, will integrate into a measured velocity error, and ultimately a radar measured position error.

2.2 Three Dimensions

We now increase the complexity of our model to 3 dimensions, and presume that the angular sensor is now a rate gyro. This configuration is shown in Figure 2.

In the 3-D IMU coordinate frame, the basic angular rate sensor parameters are

$\omega_{x'}$ = angular velocity about the x' direction,
$\omega_{y'}$ = angular velocity about the y' direction, and
$\omega_{z'}$ = angular velocity about the z' direction. (25)

We recognize that these are generally functions of time. However, we will omit the typical function notation for clarity in the subsequent development.

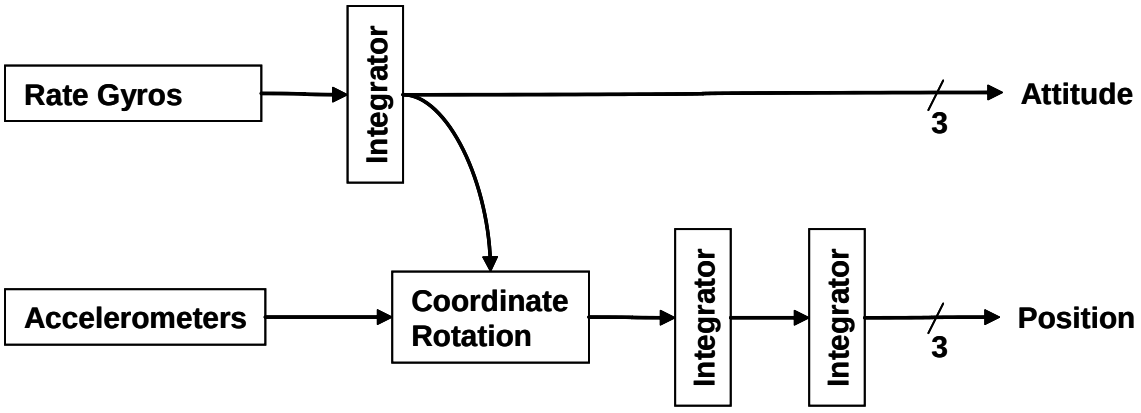

Figure 2. Simplified 3-D inertial measurement unit architecture.

The actual rotation parameters to orient the acceleration components into a useful coordinate frame are somewhat more problematic, as the rotations about the various axes are not commutative. The order of the rotations about the various axes makes a difference to the final orientation. Consider some rotations defined as

$$\begin{aligned} \theta_{x'} &= \text{rotation angle about the } x' \text{ axis,} \\ \theta_{y'} &= \text{rotation angle about the } y' \text{ axis, and} \\ \theta_{z'} &= \text{rotation angle about the } z' \text{ axis.} \end{aligned} \tag{26}$$

The final orientation of a coordinate frame depends on the order in which the rotations are applied. Applying rotations in the order $\theta_{z'}, \theta_{y'}, \theta_{x'}$ produces the following net rotation matrix,

$$\mathbf{R} = \begin{bmatrix} 1 & 0 & 0 \\ 0 & \cos\theta_{x'} & \sin\theta_{x'} \\ 0 & -\sin\theta_{x'} & \cos\theta_{x'} \end{bmatrix} \begin{bmatrix} \cos\theta_{y'} & 0 & -\sin\theta_{y'} \\ 0 & 1 & 0 \\ \sin\theta_{y'} & 0 & \cos\theta_{y'} \end{bmatrix} \begin{bmatrix} \cos\theta_{z'} & \sin\theta_{z'} & 0 \\ -\sin\theta_{z'} & \cos\theta_{z'} & 0 \\ 0 & 0 & 1 \end{bmatrix}, \tag{27}$$

or the combined result

$$\mathbf{R} = \begin{bmatrix} \cos\theta_{y'}\cos\theta_{z'} & \cos\theta_{y'}\sin\theta_{z'} & -\sin\theta_{y'} \\ \begin{pmatrix} \sin\theta_{x'}\sin\theta_{y'}\cos\theta_{z'} \\ -\cos\theta_{x'}\sin\theta_{z'} \end{pmatrix} & \begin{pmatrix} \sin\theta_{x'}\sin\theta_{y'}\sin\theta_{z'} \\ +\cos\theta_{x'}\cos\theta_{z'} \end{pmatrix} & \sin\theta_{x'}\cos\theta_{y'} \\ \begin{pmatrix} \cos\theta_{x'}\sin\theta_{y'}\cos\theta_{z'} \\ +\sin\theta_{x'}\sin\theta_{z'} \end{pmatrix} & \begin{pmatrix} \cos\theta_{x'}\sin\theta_{y'}\sin\theta_{z'} \\ -\sin\theta_{x'}\cos\theta_{z'} \end{pmatrix} & \cos\theta_{x'}\cos\theta_{y'} \end{bmatrix}. \tag{28}$$

A different order of rotations would yield a different net rotation matrix. However, for very small rotations, this becomes the differential rotation matrix

$$\delta\mathbf{R} = \begin{bmatrix} 1 & \delta\theta_{z'} & -\delta\theta_{y'} \\ -\delta\theta_{z'} & 1 & \delta\theta_{x'} \\ \delta\theta_{y'} & -\delta\theta_{x'} & 1 \end{bmatrix} = \mathbf{I} + \begin{bmatrix} 0 & \delta\theta_{z'} & -\delta\theta_{y'} \\ -\delta\theta_{z'} & 0 & \delta\theta_{x'} \\ \delta\theta_{y'} & -\delta\theta_{x'} & 0 \end{bmatrix}. \tag{29}$$

We now define the differential component as

$$\delta\boldsymbol{\Theta} = \begin{bmatrix} 0 & \delta\theta_{z'} & -\delta\theta_{y'} \\ -\delta\theta_{z'} & 0 & \delta\theta_{x'} \\ \delta\theta_{y'} & -\delta\theta_{x'} & 0 \end{bmatrix}. \tag{30}$$

Recall that the rotation matrix, as well as its components, is generally a function of time. This lets us set up the equation

$$\frac{d}{dt}\mathbf{R}(t) = \lim_{\delta t \to 0} \frac{\mathbf{R}(t+\delta t) - \mathbf{R}(t)}{\delta t} = \lim_{\delta t \to 0} \frac{\mathbf{R}(t)\delta\mathbf{R}(t) - \mathbf{R}(t)}{\delta t} = \mathbf{R}(t) \lim_{\delta t \to 0} \frac{\delta\boldsymbol{\Theta}}{\delta t}. \tag{31}$$

But we can expand the limit, and define the angular velocity matrix as

$$\boldsymbol{\Omega}(t) = \lim_{\delta t \to 0} \frac{\delta\boldsymbol{\Theta}}{\delta t} = \begin{bmatrix} 0 & \omega_{z'}(t) & -\omega_{y'}(t) \\ -\omega_{z'}(t) & 0 & \omega_{x'}(t) \\ \omega_{y'}(t) & -\omega_{x'}(t) & 0 \end{bmatrix}. \tag{32}$$

Consequently, by combining these results, we have the differential equation

$$\frac{d}{dt}\mathbf{R}(t) = \mathbf{R}(t)\boldsymbol{\Omega}(t) \tag{33}$$

which has the solution

$$\mathbf{R}(t) = \mathbf{R}(0)\exp\left(\int_0^t \boldsymbol{\Omega}(\tau)\, d\tau\right). \tag{34}$$

Typically, for SAR, we do not expect large rotations during a synthetic aperture. Consequently, for angular rates and times *t* that lead to small angular displacements, for the purposes of this report we can expand the exponential and approximate

$$\mathbf{R}(t) \approx \mathbf{R}(0)\left(\mathbf{I} + \int_0^t \boldsymbol{\Omega}(\tau)\, d\tau\right). \tag{35}$$

This can be expanded to the approximation

$$\mathbf{R}(t) \approx \mathbf{R}(0)\begin{bmatrix} 1 & \int_0^t \omega_{z'}(\tau)d\tau & -\int_0^t \omega_{y'}(\tau)d\tau \\ -\int_0^t \omega_{z'}(\tau)d\tau & 1 & \int_0^t \omega_{x'}(\tau)d\tau \\ \int_0^t \omega_{y'}(\tau)d\tau & -\int_0^t \omega_{x'}(\tau)d\tau & 1 \end{bmatrix}. \tag{36}$$

Of course, for small angular displacements, this is merely

$$\mathbf{R}(t) \approx \mathbf{R}(0)\begin{bmatrix} 1 & \Delta\theta_{z'}(t) & -\Delta\theta_{y'}(t) \\ -\Delta\theta_{z'}(t) & 1 & \Delta\theta_{x'}(t) \\ \Delta\theta_{y'}(t) & -\Delta\theta_{x'}(t) & 1 \end{bmatrix} \tag{37}$$

where the angular displacements are

$$\Delta\theta_{x'}(t) = \int_0^t \omega_{x'}(\tau)d\tau,$$

$$\Delta\theta_{y'}(t) = \int_0^t \omega_{y'}(\tau)d\tau, \text{ and}$$

$$\Delta\theta_{z'}(t) = \int_0^t \omega_{z'}(\tau)d\tau. \tag{38}$$

Nevertheless we will define the appropriate true angular displacements as

$\Delta\theta_{x',t}(t)$ = true rotation angle about the x' axis,
$\Delta\theta_{y',t}(t)$ = true rotation angle about the y' axis, and
$\Delta\theta_{z',t}(t)$ = true rotation angle about the z' axis. (39)

The true rotation matrix is then given by

$$\mathbf{R}_t(t) \approx \mathbf{R}_t(0)\begin{bmatrix} 1 & \Delta\theta_{z',t}(t) & -\Delta\theta_{y',t}(t) \\ -\Delta\theta_{z',t}(t) & 1 & \Delta\theta_{x',t}(t) \\ \Delta\theta_{y',t}(t) & -\Delta\theta_{x',t}(t) & 1 \end{bmatrix}. \tag{40}$$

Furthermore, the measured angular displacements are defined as

$\Delta\theta_{x',m}(t)$ = measured rotation angle about the x' axis,
$\Delta\theta_{y',m}(t)$ = measured rotation angle about the y' axis, and
$\Delta\theta_{z',m}(t)$ = measured rotation angle about the z' axis. (41)

The measured rotation matrix is then given by

$$\mathbf{R}_m(t) \approx \mathbf{R}_m(0)\begin{bmatrix} 1 & \Delta\theta_{z',m}(t) & -\Delta\theta_{y',m}(t) \\ -\Delta\theta_{z',m}(t) & 1 & \Delta\theta_{x',m}(t) \\ \Delta\theta_{y',m}(t) & -\Delta\theta_{x',m}(t) & 1 \end{bmatrix}. \tag{42}$$

The error in the rotation matrix is given by

$$\mathbf{R}_\varepsilon(t) = \mathbf{R}_m(t) - \mathbf{R}_t(t). \tag{43}$$

This is expanded to

$$\mathbf{R}_\varepsilon(t) = \begin{pmatrix} (\mathbf{R}_t(0) + \mathbf{R}_\varepsilon(0))\begin{bmatrix} 1 & \Delta\theta_{z',m}(t) & -\Delta\theta_{y',m}(t) \\ -\Delta\theta_{z',m}(t) & 1 & \Delta\theta_{x',m}(t) \\ \Delta\theta_{y',m}(t) & -\Delta\theta_{x',m}(t) & 1 \end{bmatrix} \\ -\mathbf{R}_t(0)\begin{bmatrix} 1 & \Delta\theta_{z',t}(t) & -\Delta\theta_{y',t}(t) \\ -\Delta\theta_{z',t}(t) & 1 & \Delta\theta_{x',t}(t) \\ \Delta\theta_{y',t}(t) & -\Delta\theta_{x',t}(t) & 1 \end{bmatrix} \end{pmatrix} \tag{44}$$

and then manipulated to

$$\mathbf{R}_\varepsilon(t) = \begin{pmatrix} \mathbf{R}_t(0)\begin{bmatrix} 0 & \Delta\theta_{z',\varepsilon}(t) & -\Delta\theta_{y',\varepsilon}(t) \\ -\Delta\theta_{z',\varepsilon}(t) & 0 & \Delta\theta_{x',\varepsilon}(t) \\ \Delta\theta_{y',\varepsilon}(t) & -\Delta\theta_{x',\varepsilon}(t) & 0 \end{bmatrix} \\ +\mathbf{R}_\varepsilon(0)\begin{bmatrix} 1 & \Delta\theta_{z',m}(t) & -\Delta\theta_{y',m}(t) \\ -\Delta\theta_{z',m}(t) & 1 & \Delta\theta_{x',m}(t) \\ \Delta\theta_{y',m}(t) & -\Delta\theta_{x',m}(t) & 1 \end{bmatrix} \end{pmatrix}. \tag{45}$$

where the respective errors between measured and true component values are then

$\Delta\theta_{x',\varepsilon}(t) = \Delta\theta_{x',m}(t) - \Delta\theta_{x',t}(t)$ = error angle about the x' axis,
$\Delta\theta_{y',\varepsilon}(t) = \Delta\theta_{y',m}(t) - \Delta\theta_{y',t}(t)$ = error rotation angle about the y' axis, and
$\Delta\theta_{z',\varepsilon}(t) = \Delta\theta_{z',m}(t) - \Delta\theta_{z',t}(t)$ = error rotation angle about the z' axis. (46)

We will again assume small angular errors, namely

$$\begin{aligned}
&\left|\Delta\theta_{x',\varepsilon}(t)\right| << 1, \\
&\left|\Delta\theta_{y',\varepsilon}(t)\right| << 1, \text{ and} \\
&\left|\Delta\theta_{z',\varepsilon}(t)\right| << 1.
\end{aligned} \tag{47}$$

Based on previous approximations, the rotation matrix error can be reasonably approximated as

$$\mathbf{R}_{\varepsilon}(t) = \mathbf{R}_{\varepsilon}(0) + \mathbf{R}_{t}(0)\begin{bmatrix} 0 & \Delta\theta_{z',\varepsilon}(t) & -\Delta\theta_{y',\varepsilon}(t) \\ -\Delta\theta_{z',\varepsilon}(t) & 0 & \Delta\theta_{x',\varepsilon}(t) \\ \Delta\theta_{y',\varepsilon}(t) & -\Delta\theta_{x',\varepsilon}(t) & 0 \end{bmatrix}. \tag{48}$$

To be a little more explicit, in terms of angular rate errors,

$$\mathbf{R}_{\varepsilon}(t) = \mathbf{R}_{\varepsilon}(0) + \mathbf{R}_{t}(0)\begin{bmatrix} 0 & \int_0^t \omega_{z',\varepsilon}(\tau)d\tau & -\int_0^t \omega_{y',\varepsilon}(\tau)d\tau \\ -\int_0^t \omega_{z',\varepsilon}(\tau)d\tau & 0 & \int_0^t \omega_{x',\varepsilon}(\tau)d\tau \\ \int_0^t \omega_{y',\varepsilon}(\tau)d\tau & -\int_0^t \omega_{x',\varepsilon}(\tau)d\tau & 0 \end{bmatrix}, \tag{49}$$

where we have substituted the angular displacements with integrated angular rates, namely

$$\begin{aligned}
\Delta\theta_{x',\varepsilon}(t) &= \int_0^t \omega_{x',\varepsilon}(\tau)d\tau, \\
\Delta\theta_{y',\varepsilon}(t) &= \int_0^t \omega_{y',\varepsilon}(\tau)d\tau, \text{ and} \\
\Delta\theta_{z',\varepsilon}(t) &= \int_0^t \omega_{z',\varepsilon}(\tau)d\tau.
\end{aligned} \tag{50}$$

Furthermore, out of convenience we will also assume $\mathbf{R}_{t}(0) = \mathbf{I}$.

Now, in the 3-D IMU coordinate frame, we define the basic acceleration sensor parameters as

$a_{x'}$ = acceleration in x' direction,

$a_{y'}$ = acceleration in y' direction, and

$a_{z'}$ = acceleration in z' direction. (51)

Consequently, the acceleration vector is constructed as

$$\mathbf{a}' = \begin{bmatrix} a_{x'} \\ a_{y'} \\ a_{z'} \end{bmatrix}. \tag{52}$$

With respect to true and measured values, it remains true that

$$\mathbf{a}_\varepsilon(t) = \mathbf{a}_m(t) - \mathbf{a}_t(t) = \mathbf{R}_m(t)\mathbf{a}'_m(t) - \mathbf{R}_t(t)\mathbf{a}'_t(t) \tag{53}$$

which can be expanded to

$$\mathbf{a}_\varepsilon(t) = (\mathbf{R}_t(t) + \mathbf{R}_\varepsilon(t))\mathbf{a}'_m(t) - \mathbf{R}_t(t)\mathbf{a}'_t(t) = \mathbf{R}_\varepsilon(t)\mathbf{a}'_m(t) + \mathbf{R}_t(t)\mathbf{a}'_\varepsilon(t) \tag{54}$$

and then approximated as

$$\mathbf{a}_\varepsilon(t) \approx \mathbf{R}_\varepsilon(t)\mathbf{a}'_t(t) + \mathbf{R}_t(t)\mathbf{a}'_\varepsilon(t). \tag{55}$$

For expedience, in this development we will ignore the effects of gravity and other effects such as earth rotation, etc. Recall that in an inertial coordinate frame the velocity and position errors are

$$\mathbf{v}_\varepsilon(t) = \int_0^t \mathbf{a}_\varepsilon(\tau)d\tau + \mathbf{v}_\varepsilon(0), \text{ and}$$

$$\mathbf{p}_\varepsilon(t) = \int_0^t \mathbf{v}_\varepsilon(\tau)d\tau + \mathbf{p}_\varepsilon(0). \tag{56}$$

Some observations then include

- An acceleration error in the radar frame can be induced by instrument acceleration errors.
- An acceleration error in the radar frame can also be induced by real acceleration with an instrument angular orientation error.
- Any net acceleration error, by whatever source, will integrate into a measured velocity error, and ultimately a radar measured position error, and finally a range error to the target reference point.

2.3 Effects of Gravity

The forces working on an IMU include gravity, which will in fact be measured by the accelerometers. Consequently, since gravity is a component of the accelerations apparent to the accelerometers, the measured accelerations need to be corrected for gravity acceleration in order to be useful for motion measurement. Gravity acceleration would be perfectly subtracted if the measured accelerations of the instruments were perfect. However, gravity acceleration will in fact be subtracted imperfectly due to errors in the knowledge of the IMU orientation.

With respect to true and measured values, both will have gravity components. However, we are interested in accelerations where the effects of gravity are subtracted. Recall that the acceleration error is calculated to be

$$\mathbf{a}_\varepsilon(t) = \mathbf{a}_m(t) - \mathbf{a}_t(t) = \mathbf{R}_m(t)\mathbf{a}'_m(t) - \mathbf{R}_t(t)\mathbf{a}'_t(t). \tag{57}$$

This was manipulated to

$$\mathbf{a}_\varepsilon(t) = \mathbf{R}_t(t)\mathbf{a}'_\varepsilon(t) + \mathbf{R}_\varepsilon(t)\mathbf{a}'_m(t) \approx \mathbf{R}_t(t)\mathbf{a}'_\varepsilon(t) + \mathbf{R}_\varepsilon(t)\mathbf{a}'_t(t). \tag{58}$$

However, now the true and measured accelerations include gravity. We can explicitly show the effects of gravity by manipulating this to

$$\mathbf{a}_\varepsilon(t) \approx \mathbf{R}_t(t)\mathbf{a}'_\varepsilon(t) + \mathbf{R}_\varepsilon(t)\left(\mathbf{a}'_t(t) - \mathbf{a}'_g(t)\right) + \mathbf{R}_\varepsilon(t)\mathbf{a}'_g(t). \tag{59}$$

where

$\mathbf{a}'_g(t)$ = acceleration due to gravity in the IMU coordinate frame. (60)

We note that the calculus to find radar velocity needs to be on the acceleration after gravity has been removed, that is, the acceleration used to find radar motion integrates the quantity $\left(\mathbf{a}'_t(t) - \mathbf{a}'_g(t)\right)$. Specifically, the radar velocity calculation needs to be

$$\mathbf{v}_t(t) = \int_0^t \mathbf{R}_t(\tau)\left(\mathbf{a}'_t(\tau) - \mathbf{a}'_g(\tau)\right)d\tau + \mathbf{v}_t(0). \tag{61}$$

Consequently, a radar at constant velocity will exhibit $\left(\mathbf{a}'_t(t) - \mathbf{a}'_g(t)\right) = 0$. This means that gravity will still influence the net acceleration error via an angular orientation measurement error.

Note that the gravity acceleration vector $\mathbf{a}'_g(t)$ is a function of time because the orientation of the IMU coordinate frame with respect to the earth's surface may in

general also be a function of time. However the magnitude and earth-centric direction of this vector is constant, at least to the degree that gravity is constant.

Note also that since

$$g = \left|\mathbf{a}'_g(t)\right| \approx 9.8\,\mathrm{m/s^2}, \tag{62}$$

it is not unreasonable to expect that gravity is a strong contributor to motion measurement errors. In fact, we would expect it to often swamp any other non-gravity accelerations.

For example, consider a 0.02 degree error in the presumed direction of gravity. This will generate an erroneous 0.0017 $\mathrm{m/s^2}$ horizontal acceleration indication. After 10 seconds, this results in a 17 cm position error. At Ku-band this represents 18.9 wavelengths (for a round-trip), enough to cause fairly severe misfocus, and unacceptable residual migration at resolutions finer than this value.

2.4 Other Effects

Other contributors to acceleration and angular measurement errors might include

- Gravity anomalies

  Gravity in general varies in both direction and magnitude with latitude, longitude, altitude, earth topography, tides, and lateral density variations. Magnitude variations may be up to about 0.7%.[5]

- Tidal effects

  The gravitational attraction of the moon itself will cause up to a 0.0004 degree deflection of the gravity vector during a day. (This is calculated from the moon's gravitational attraction being approximately 3.38×10^{-6} that of earth's gravity.)

- Earth rotation effects

  The earth rotates at about 15.04 degrees/hour (360 degrees per sidereal day, which is approximately 23.9344 hours). This is significant with respect to most gyro specs.

- Coriolis effect

  In physics, the Coriolis effect is an apparent deflection of moving objects when they are viewed from a rotating frame of reference, such as the earth. It is mathematically deduced from the law of inertia.

Some of these are easily compensated, others are not, and others yet may not be worth compensating, depending on the requirements of motion measurement.

“If you do not change direction, you may end up where you are heading.”
-- Lao Tzu

3 The Nature of IMU Errors

IMUs vary considerably in the fidelity of their outputs. They are generally classified into three different major grades.

Navigation Grade IMUs, sometimes called High Accuracy Inertial Navigation Systems (HAINS), are the highest quality IMUs and are generally designed for long-term accuracy guidance and control applications. Typical applications include aircraft navigation. An example of this is the Honeywell HG-9900 Navigation Grade IMU.[6]

Tactical Grade IMUs are of lesser quality than the Navigation Grade IMUs. Typical applications include shorter term missile guidance and control, and sensor orientation. Examples include the Northrop Grumman LN-200 Fiber Optic IMU,[7] Honeywell HG-1700 IMU,[8] and the Honeywell HG-1900 MEMS IMU.[9]

The lowest quality IMUs go by names such as Automotive Grade, and MEMS grade. That is not to say that they aren't useful; just that they are of lesser precision and accuracy than the other major grades. An example is the Honeywell HG-1930 MEMS IMU.[10]

Some technologies lend themselves more to one grade than another. For example, Ring Laser Gyro (RLG) components tend to be found in Navigation Grade IMUs, whereas Fiber Optic Gyro (FOG) components tend to be found in Tactical Grade IMUs[11], and Micro-Electro-Mechanical Systems (MEMS) components tend to be found in Automotive Grade IMUs. That is not to say that these relationships are exclusive, nor that other technologies for angle or rate sensing aren't also useful. For example, The Honeywell HG-1900 contains MEMS components but offers performance in many respects comparable to other Tactical Grade IMUs.

A good discussion of inertial sensor technologies is given by Lawrence.[12]

There are substantial cost differences between these various technologies and IMU grades, hence the desire to use something 'good enough' but not excessively expensive.

We also note that IMU outputs typically feed an Extended Kalman Filter (EKF) that uses independent position/motion measurements to aid the IMU and help estimate IMU errors. More on this later.

For the following discussion, we employ an initial error model similar to that presented by Flenniken, et al.[13,14]

3.1 Accelerometer Errors

An accelerometer is designed to measure acceleration. There are generally three accelerometers in an IMU, oriented in an orthogonal manner to measure acceleration in a 3-D space. We initially model the measured acceleration in a particular direction as

$$a_m = \begin{pmatrix} (1+\beta)a_t + \beta_a|a_t| + \beta_n {a_t}^2 + a_\perp \sin(\varphi_m + \varphi_n) \\ + b_{a,0} + n_{a,q} + n_{a,0} + n_{a,1} + n_{a,2} \end{pmatrix} \tag{63}$$

where

a_t = true acceleration in the desired measurement direction,
β = scale factor error.
β_a = scale factor asymmetry,
β_n = scale factor nonlinearity,
$a_\perp$ = true acceleration in the orthogonal (perpendicular) direction,
φ_m = angular misalignment error,
φ_n = angular nonorthogonality error,
$b_{a,0}$ = constant bias error,
$n_{a,q}$ = quantization noise,
$n_{a,0}$ = white noise error (velocity random walk error source),
$n_{a,1}$ = flicker noise error,
$n_{a,2}$ = acceleration random walk error. (64)

We identify the acceleration error as

$$a_\varepsilon = a_m - a_t = \begin{pmatrix} \beta a_t + \beta_a|a_t| + \beta_n {a_t}^2 + a_\perp \sin(\varphi_m + \varphi_n) \\ + b_{a,0} + n_{a,q} + n_{a,0} + n_{a,1} + n_{a,2} \end{pmatrix}. \tag{65}$$

3.1.1 Scale Factor Error

While scale factor errors, misalignment error, and nonorthogonality error can generally be calibrated to insignificance for SAR applications, they may not always be so calibrated, and residual errors may exist.

Scale factor errors are often lumped together into a single 'scale factor accuracy' number. Consequently

$$\left(\beta a_t + \beta_a|a_t| + \beta_n {a_t}^2\right) = \mathrm{B}(a_t)\, a_t \tag{66}$$

where

$\mathrm{B}(a_t)$ = scale factor perturbation function. (67)

Accelerometer specifications typically limit $|\mathrm{B}(a_t)|$ to some number of Parts Per Million (PPM), typically up to several hundred PPM for tactical grade IMU accelerometers. This means that the degree to which this affects acceleration measurements, in fact depends on acceleration. In any case, scale factor accuracy is limited to

$$|\mathrm{B}(a_t)| \le \mathrm{B}_{\max}. \tag{68}$$

Note that the true acceleration a_t is a function of time, as the flight path of the IMU is a function of time. The actual position error change is a double integration of this rate, namely

$$p_\varepsilon = \int_0^T\int \mathrm{B}(a_t)\, a_t dtdt. \tag{69}$$

This position error is bounded by

$$p_\varepsilon \le \int_0^T\int |\mathrm{B}(a_t)\, a_t| dtdt \le \mathrm{B}_{\max}\int_0^T\int |a_t| dtdt. \tag{70}$$

The acceleration error accumulated is clearly dependent on the degree of maneuver in the radar's flight path. In addition, there is gravity. For benign flight paths, especially straight and level, nearly constant velocity flight paths, $|a_t|$ remains rather small in lateral directions, and is effectively gravity in the vertical direction. This makes scale factors a relatively insignificant contributor to lateral acceleration errors over typical synthetic aperture times. However, gravity is a fairly large acceleration and furthermore is persistent during the synthetic aperture. Woodman[2] states "In most applications the magnitude of g is much greater than the mean absolute acceleration of the IMU itself."

The contribution of gravity depends on the direction of interest, and is given by

$$p_\varepsilon \le \mathrm{B}_{\max}\int_0^T\int g\sin\psi dtdt = \mathrm{B}_{\max} g\sin\psi \frac{T^2}{2}. \tag{71}$$

Airborne SAR grazing angles may be as shallow as low-single-digit degrees, or as steep as perhaps 60 degrees, and sometimes more. We note that from a given altitude, a depression angle of 5 degrees will intersect the ground approximately ten times farther away than at a depression angle of 60 degrees. For a given azimuth resolution, then the synthetic aperture for the shallow grazing angle will be ten times longer than for the steep

grazing angle. Furthermore, the projection of gravity in those directions will also differ by approximately a factor of ten.

So, the largest position error in the direction of the target will likely occur at the shallowest grazing angle, where the synthetic aperture is the longest.

Example 1

> Consider the IMU on a platform where accelerations are dominated by gravity, and SAR imaging is at a grazing angle of 5 degrees. If scale factor accuracy were 300 PPM, then after 10 seconds, the net position error in the direction of the target scene may be as high as 0.013 m. This is typically easily accommodated by autofocus operations.

Example 2

> Consider the IMU on a platform where accelerations are dominated by gravity, and SAR imaging is at a grazing angle of 5 degrees. If scale factor accuracy were 300 PPM, then after 100 seconds, the net position error in the direction of the target scene may be as high as 1.3 m. This is typically not easily accommodated by autofocus operations for fine resolution SAR.

To be sure, we have considered just gravity to calculate this error bound. Additional accelerations will compound this.

In any case, accelerometer scale factor errors can be expected to contribute to position errors more so for maneuvering platforms, non-benign flight paths, and longer synthetic apertures.

Anecdote:

The LN-200 scale factor accuracy is specified by the manufacturer as 100-5000 PPM., depending on IMU grade. Other sources indicate nonlinearity of 50.0 $\mu g/g^2$.[1]

3.1.2 Misalignment and Nonorthogonality Errors

An accelerometer alignment error (misalignment) allows the accelerometer to measure acceleration along an axis different than what is presumed. A nonorthogonality error causes an improper correction for the actual nonorthogonality. Both errors cause an improper acceleration measurement, by allowing orthogonal accelerations to perturb true acceleration measurements, and ultimately yield accumulated position errors. This again allows coupling of undesired accelerations such as gravity in undesired directions.

The resultant acceleration error in this case is bounded by

$$a_\varepsilon \le a_\perp \sin(\varphi_m + \varphi_n). \tag{72}$$

As with scale factor errors, an angular error due to misalignment or nonorthogonality will allow a portion of gravity to integrate into a position error, which we bound as

$$p_{\varepsilon} \le g \sin(\phi_m + \phi_n) \frac{T^2}{2} . \tag{73}$$

Example 1

> Consider the IMU on a platform that exhibits misalignment and nonorthogonality errors that were limited to 0.1 mrad (21 arcsec.). With 1 g of orthogonal acceleration, then after 10 seconds, the net position error may change by as much as 0.049 m. This is typically easily accommodated by autofocus operations.

Example 2

> Consider the IMU on a platform that exhibits misalignment and nonorthogonality errors that were limited to 0.1 mrad (21 arcsec.). With 1 g of orthogonal acceleration, then after 100 seconds, the net position error may change by as much as 4.9 m. This is typically not easily accommodated by autofocus operations for fine resolutions.

Again, to be sure, we have considered just gravity to calculate this error bound. Additional accelerations will compound this.

Nevertheless, misalignment or nonorthogonality errors can be expected to contribute to position errors more so for maneuvering platforms, non-benign flight paths, and longer synthetic apertures.

Anecdote:

The LN-200 misalignment is specified to be 20-200 arcsec., depending on IMU grade.[1]

3.1.3 Constant Bias Error

This bias term $b_{a,0}$ is also sometimes called the 'random' bias term. It is considered a constant while the accelerometer is operating, but will vary with random value from one unit turn-on (power-up) to the next.

This term is readily estimated by the EKF and thereby removed from the measurements.

Anecdote

The LN-200 manufacturer specifies this value as 300-3000 μg (1-sigma), depending on IMU grade.

3.1.4 Noise Errors

Scale factor errors, misalignment error, and nonorthogonality error can generally be calibrated to insignificance for SAR applications. The constant bias error can generally be adequately mitigated via an alignment procedure and adaptation of the EKF. This leaves the four noise terms of our model. The error model then is reduced to

$$a_\varepsilon \approx n_{a,q} + n_{a,0} + n_{a,1} + n_{a,2}\,. \tag{74}$$

Of these noise terms, an Allan variance (see Appendix A) analysis shows that different components dominate on different time scales. Since SAR synthetic apertures typically last from single digit seconds to perhaps 100 seconds or so, and IMU sampling frequencies are in the range of 100 Hz or higher, then quantization noise can be expected to be a small contributor to the overall error. With respect to the other terms, we identify the following parameters with customary units in parentheses.

$$\begin{aligned} N &= \text{white noise parameter responsible for angular random walk } (\mu g/\sqrt{Hz}\,),\\ B &= \text{bias instability parameter } (\mu g\,), \text{ and}\\ K &= \text{acceleration random walk parameter } (\mu g/s^{1/2}\,). \end{aligned} \tag{75}$$

From these we identify the following two-sided noise power spectral densities.

$$S_N(f) = N^2 \quad (\mu g)^2/Hz\ , \tag{76}$$

$$S_B(f) = \frac{B^2}{2\pi|f|} \quad (\mu g)^2/Hz\,, \text{ and} \tag{77}$$

$$S_K(f) = \frac{K^2}{(2\pi f)^2} \quad (\mu g)^2/Hz\,. \tag{78}$$

Of course, the PSD of the accumulated independent noise terms is the sum of these PSDs.

Example

We illustrate the characteristics of these noise components with a hypothetical accelerometer with the following parameters.

$$\begin{aligned} N &= 50\ \mu g/\sqrt{Hz}\,,\\ B &= 50\ \mu g\,, \text{ and}\\ K &= 5\ \mu g/s^{1/2}\,. \end{aligned} \tag{79}$$

The resulting PSD is illustrated in Figure 3.

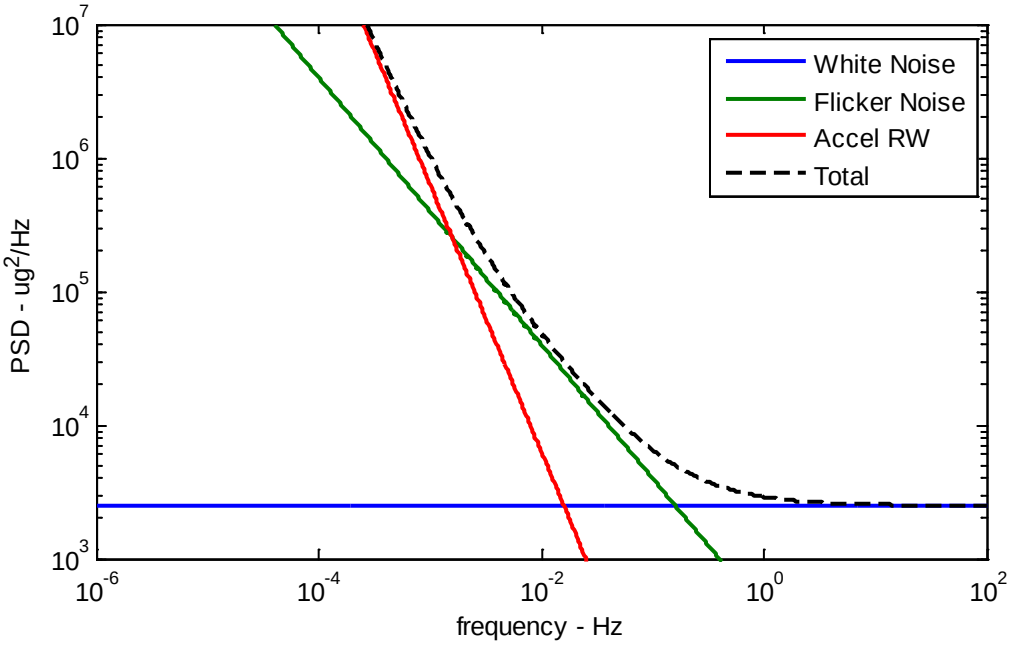

Figure 3. Hypothetical accelerometer noise PSD.

We offer the following observations and comments.

- The example is typical with respect to what can be found in the literature with respect to the following. The noise PSD in the frequency region of greatest interest to SAR image formation ($10^{-2} < f < 10^{2}$) is typically dominated by white noise at the higher end, and by flicker noise at the lower end of this range. Acceleration random walk probably does not contribute meaningful variations to the bias during typical synthetic apertures, but may when aperture times enter triple-digit seconds.

- Noise parameters are often not reported on manufacturer data sheets. However, some values can be found elsewhere in the literature, especially for N and B. Information on the parameter K is much more scarce.

- These parameters can be determined via Allan variance measurements (see Appendix A). Published Allan variance plots can sometimes be found in the literature.

Anecdote

The LN-200 manufacturer's data sheet doesn't specify these parameters. Other sources specify for the LN-200 the values $N = 50\ \mu g/\sqrt{Hz}$, and $B = 50\ \mu g$.[1]

3.1.5 Comprehensive Accelerometer Error Model

Collecting the results of the previous discussion, we somewhat reduce the accelerometer error model to

$$a_\varepsilon = |a_t| \mathrm{B}_{\max} + a_\perp \sin(\varphi_m + \varphi_n) + n_{a,0} + n_{a,1} + n_{a,2}\,. \tag{80}$$

The relevant accelerometer errors are collected and modeled in Figure 4. Note that the constant bias error is omitted as it is easily filtered, and quantization error is omitted as inconsequential to the time scales of interest.

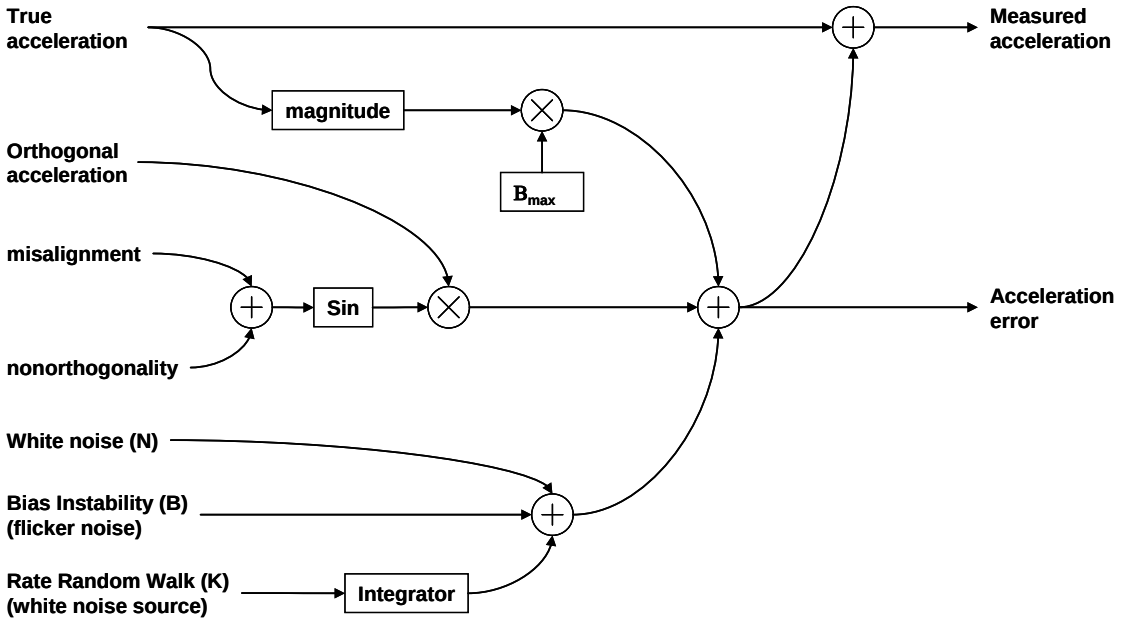

Figure 4. Accelerometer model with error sources.

3.2 Rate Gyro Errors

A rate gyro is designed to measure angular velocity. There are generally three rate gyros in an IMU, oriented in an orthogonal manner to measure angular velocity in a 3-D space. We initially model the measured angular velocity around a particular axis in a particular direction as

$$\omega_m = \begin{pmatrix} (1+\gamma)\omega_t + \gamma_a|\omega_t| + \gamma_n {\omega_t}^2 + \omega_\perp \sin(\phi_m + \phi_n) \\ + b_{\omega,0} + n_{\omega,q} + n_{\omega,0} + n_{\omega,1} + n_{\omega,2} \end{pmatrix} \tag{81}$$

where

ω_t = true angular rate in the desired measurement direction,
γ = scale factor error.
γ_a = scale factor asymmetry,
γ_n = scale factor nonlinearity,
$\omega_\perp$ = true angular rate in the orthogonal (perpendicular) direction,
ϕ_m = angular misalignment error,
ϕ_n = angular nonorthogonality error,
$b_{\omega,0}$ = constant bias error,
$n_{\omega,q}$ = quantization noise,
$n_{\omega,0}$ = white noise error (angular random walk error source),
$n_{\omega,1}$ = flicker noise error,
$n_{\omega,2}$ = rate random walk error. (82)

We identify the angular rate error as

$$\omega_\varepsilon = \omega_m - \omega_t = \begin{pmatrix} \gamma\omega_t + \gamma_a|\omega_t| + \gamma_n {\omega_t}^2 + \omega_\perp \sin(\phi_m + \phi_n) \\ + b_{\omega,0} + n_{\omega,q} + n_{\omega,0} + n_{\omega,1} + n_{\omega,2} \end{pmatrix}. \tag{83}$$

3.2.1 Scale Factor Error

While scale factor errors, misalignment error, and nonorthogonality error can generally be calibrated to insignificance for SAR applications, they may not always be so calibrated, and residual errors may exist.

Scale factor errors are often lumped together into a single ‘scale factor accuracy’ number. Consequently

$$\left(\gamma\omega_t + \gamma_a|\omega_t| + \gamma_n{\omega_t}^2\right) = \Gamma(\omega_t)\,\omega_t \tag{84}$$

where

$\Gamma(\omega_t)$ = scale factor perturbation function. (85)

Gyro specifications typically limit $|\Gamma(\omega_t)|$ to some number of PPM, typically up to several hundred PPM for tactical grade IMU gyros. This means that the degree to which this affects angular rate, in fact depends on angular rate. In any case, scale factor accuracy is limited to

$$|\Gamma(\omega_t)| \le \Gamma_{\max}. \tag{86}$$

Note that ω_t is a function of time, as the flight path of the IMU is a function of time. The actual angular error change is an integration of this rate, namely

$$\Delta\theta_\varepsilon = \int_0^T \Gamma(\omega_t)\,\omega_t dt. \tag{87}$$

This angular error is bounded by

$$\Delta\theta_\varepsilon \le \int_0^T |\Gamma(\omega_t)\,\omega_t| dt \le \Gamma_{\max} \int_0^T |\omega_t| dt. \tag{88}$$

The angular error accumulated is clearly dependent on the degree of maneuver in the radar's flight path. For benign flight paths, especially straight and level flight paths, $|\omega_t|$ remains rather small, making scale factors a relatively insignificant contributor to gyro rate errors over typical synthetic aperture times. However, this may not be the case on maneuvering platforms.

If we assume that the orientation of the rate-gyro is approximately the same at beginning and end of the synthetic aperture, then

$$\int_0^T \omega_t dt \approx 0. \tag{89}$$

but the integral of the magnitude of the rate is

$$\int_0^T |\omega_t| dt \approx 2\Delta\theta_d \tag{90}$$

where

$\Delta\theta_d$ = the accumulated angular displacement in one direction. (91)

Consequently, we can calculate a bound on the accumulated angular error as

$$\Delta\theta_\varepsilon \le \Gamma_{\max} 2\Delta\theta_d . \tag{92}$$

Recall that an angular error that affects the presumed direction of gravity allows gravity to couple into a lateral acceleration. Such an error is any that yields an elevation direction error. The resultant gravity coupling in turn is double-integrated into a position error, which for small errors becomes

$$p_\varepsilon \le \int_0^T\int g\sin(\Delta\theta_\varepsilon)dtdt \le g\frac{T^2}{2}\sin(2\Gamma_{\max}\Delta\theta_d). \tag{93}$$

This, of course, assumes that the accumulated angular error is largely accumulated near the beginning of the synthetic aperture. If the angular displacement is given in radians, then this becomes

$$p_\varepsilon \le gT^2\Gamma_{\max}\Delta\theta_d . \tag{94}$$

The relevant angular rates applied to the gyros during a synthetic aperture would be the roll and pitch rates of the aircraft. Of these, the roll extents and rates are usually greater.

Example 1

Consider the IMU on a platform that exhibits a cumulative roll displacement of 30 degrees during a 10 second synthetic aperture. If scale factor accuracy were 100 PPM, then after 10 seconds, the net position error may be as high as 0.051 m. This is typically easily accommodated by autofocus operations.

Example 2

Consider the IMU on a platform that exhibits a cumulative roll displacement of 30 degrees during a 100 second synthetic aperture. If scale factor accuracy were 100 PPM, then after 100 seconds, the net position error may be as high as 5.1 m. This is typically not easily accommodated by autofocus operations.

To be sure, we have run together a number of worst case scenarios to arrive at the error bound. These included absolute worst-case scale factor accuracy, no cancellation of errors with different signs in ω_t, and the entire angular displacement occurring at the beginning of the synthetic aperture.

Nevertheless, scale factor errors can be expected to contribute to position errors more so for maneuvering platforms, non-benign flight paths, and longer synthetic apertures.

Anecdote:

The LN-200 scale factor accuracy is specified by the manufacturer as 100-500 PPM, depending on IMU grade.

3.2.2 Misalignment and Nonorthogonality Errors

A rate-gyro alignment error (misalignment) allows the gyro to measure angular rates around an axis different than what is presumed. A nonorthogonality error causes an improper correction for the actual nonorthogonality. Both errors cause an improper rate-gyro measurement, by allowing orthogonal angular rates to perturb true angular rates, and ultimately yield accumulated angular (attitude) errors. This again allows coupling of undesired accelerations such as gravity in undesired directions.

This angular error in this case is bounded by

$$\Delta\theta_\varepsilon \le \int_0^T \omega_\perp \sin(\phi_m + \phi_n) dt \quad \le \sin(\phi_m + \phi_n)\Delta\theta_d \,. \tag{95}$$

In this case,

$$\Delta\theta_d \text{ = net angular displacement during synthetic aperture.} \tag{96}$$

As with scale factor errors, an angular error due to misalignment or nonorthogonality will allow a portion of gravity to integrate into a position error, which we bound as

$$p_\varepsilon \le gT^2 \frac{\sin(\phi_m + \phi_n)}{2} \Delta\theta_d \,. \tag{97}$$

Example 1

Consider the IMU on a platform that exhibits a net heading change of 30 degrees during a 10 second synthetic aperture. If the misalignment and nonorthogonality errors were limited to 0.1 mrad (21 arcsec.), then after 10 seconds, the net position error may change by as much as 0.026 m. This is typically easily accommodated by autofocus operations.

Example 2

Consider the IMU on a platform that exhibits a net heading change of 30 degrees during a 100 second synthetic aperture. If the misalignment and nonorthogonality errors were limited to 0.1 mrad (21 arcsec.), then after 100 seconds, the net

position error may change by as much as 2.61 m. This is typically not easily accommodated by autofocus operations at fine resolutions.

Again, to be sure, we have assumed a worst case scenario to arrive at the error bound. This included the entire angular displacement occurring at the beginning of the synthetic aperture.

Nevertheless, misalignment or nonorthogonality errors can be expected to contribute to position errors more so for maneuvering platforms, non-benign flight paths, and longer synthetic apertures.

Anecdote:

The LN-200 gyro misalignment is specified to be 20-200 arcsec., depending on IMU grade.[1]

3.2.3 Constant Bias Error

This bias term $b_{\omega,0}$ is also sometimes called the 'random' bias term. It is considered a constant while the gyro is operating, but will vary with random value from one unit turn-on (power-up) to the next.

This term is readily estimated by the EKF and thereby removed from the measurements.

Anecdote

The LN-200 manufacturer specifies this value as 0.5-3 $^\circ/h$ (1-sigma), depending on IMU grade.

3.2.4 Noise Errors

Scale factor errors, misalignment error, and nonorthogonality error can generally be calibrated to insignificance for SAR applications. The constant bias error can generally be adequately mitigated via an alignment procedure and adaptation of the EKF. This leaves the four noise terms of our model. The error model then is reduced to

$$\omega_\varepsilon \approx n_{\omega,q} + n_{\omega,0} + n_{\omega,1} + n_{\omega,2}\,. \tag{98}$$

Of these noise terms, an Allan variance analysis shows that different components dominate on different time scales. Since SAR synthetic apertures typically last from single digit seconds to perhaps 100 seconds or so, and IMU sampling frequencies are in the range of 100 Hz or higher, then quantization noise can be expected to be a small contributor to the overall error.

With respect to the other terms, we identify the following parameters with customary units in parentheses.

N = white noise parameter responsible for angular random walk ($^\circ/\sqrt{h}$)
B = bias instability parameter ($^\circ/h$).
K = rate random walk parameter ($^\circ/h^{3/2}$). (99)

From these we identify the following two-sided noise power spectral densities.

$$S_N(f) = 3600N^2 \quad (^\circ/h)^2/Hz \ . \tag{100}$$

$$S_B(f) = \frac{B^2}{2\pi|f|} \quad (^\circ/h)^2/Hz \ . \tag{101}$$

$$S_K(f) = \frac{K^2}{3600(2\pi f)^2} \quad (^\circ/h)^2/Hz \ . \tag{102}$$

Of course, the PSD of the accumulated independent noise terms is the sum of these PSDs.

Note that $^\circ/h$ can be converted to $^\circ/s$ by dividing by 3600. Of course $(^\circ/h)^2$ can be converted to $(^\circ/s)^2$ by dividing by 3600^2, or 12960000.

Example

We illustrate the characteristics of these noise components with a hypothetical gyro with the following parameters.

N = 0.04 $^\circ/\sqrt{h}$
B = 0.4 $^\circ/h$
K = 0.4 $^\circ/h^{3/2}$. (103)

The resulting PSD is illustrated in Figure 5.

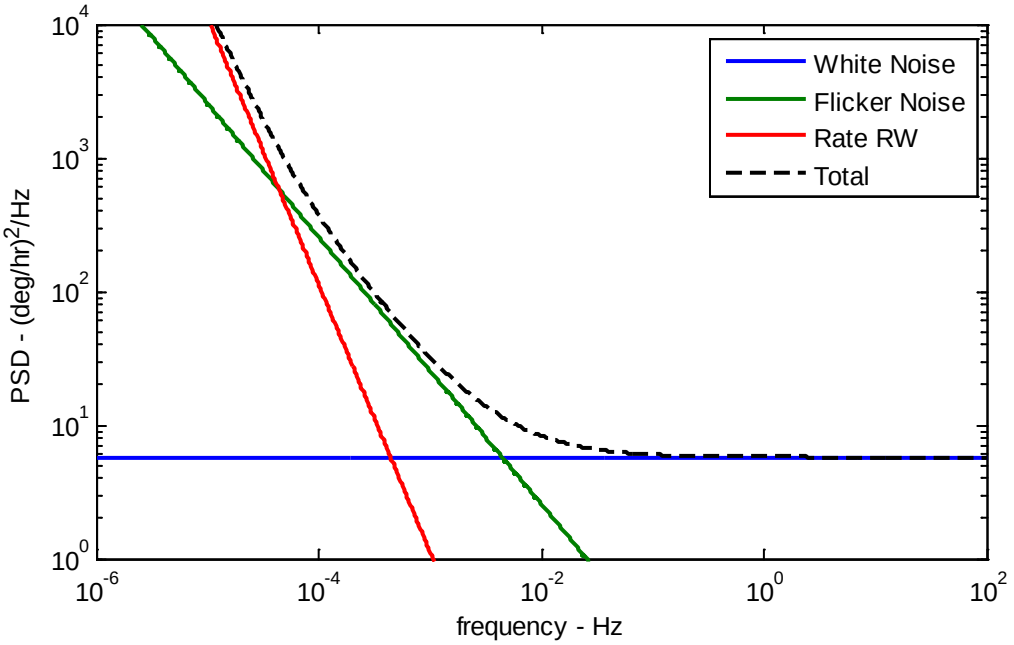

Figure 5. Hypothetical rate gyro noise PSD.

We offer the following observations and comments.

- The example is typical with respect to what can be found in the literature with respect to the following. The noise PSD in the frequency region of greatest interest to SAR image formation ($10^{-2} < f < 10^{2}$) is typically dominated by white noise. Flicker noise may become significant at the lower end of this range, but rate random walk probably does not contribute meaningful variations to the bias during typical synthetic apertures.

- Manufacturers will usually specify N in their data sheets. The parameter B is considerably more scarce, and K is very difficult to find for most IMU gyros.

- These parameters can be determined via Allan variance measurements. Published Allan variance plots can sometimes be found in the literature.

Anecdote

The LN-200 manufacturer's data sheet specifies N = 0.05-0.15 $^\circ/\sqrt{h}$, but not B or K. Other sources specify for the LN-200 the values N = 0.04-0.15 $^\circ/\sqrt{h}$, and B = 0.35 $^\circ/h$.[1] Evidence suggests that the Northrop Grumman LN-200 IMU's gyro performance is dominated by N in the region of interest to SAR.[15,16]

3.2.5 Comprehensive Rate Gyro Error Model

Collecting the results of the previous discussion, we somewhat reduce the rate gyro error model to

$$\omega_\varepsilon = |\omega_t|\Gamma_{\max} + \omega_\perp \sin(\phi_m + \phi_n) + n_{\omega,0} + n_{\omega,1} + n_{\omega,2}\,. \tag{104}$$

The relevant rate gyro errors are collected and modeled in Figure 6. Note that the constant bias error is omitted as it is easily filtered, and quantization error is omitted as inconsequential to the time scales of interest.

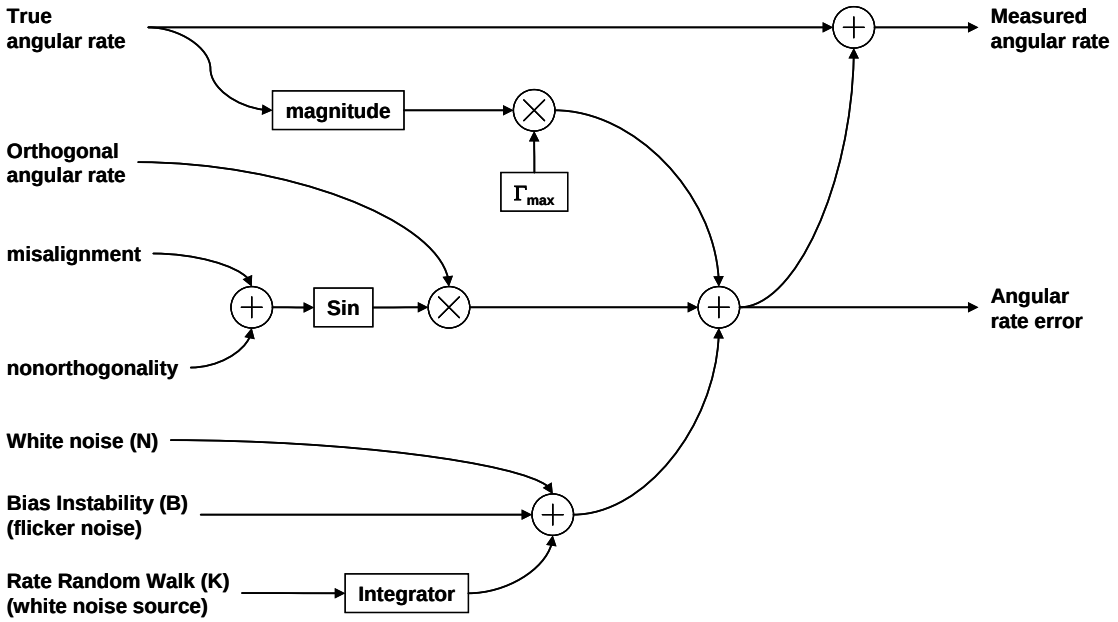

Figure 6. Rate gyro model with error sources.

The parameters of several rate-gyros are compared by Flenniken and Hamm.[17]

3.3 Other Effects

Note that many of these errors parameters themselves are not static, and may depend on environmental conditions, or change over time.

3.3.1 Temperature

Temperature affects both accelerometers and gyros. Optical gyros typically have their light-source wavelength affected by temperature, and the rate of change of temperature. This manifests itself as bias and scale factor variations with temperature. Pavlath[11] shows plots of both. Woodman[2] indicates sensor self-heating is also to be considered. Temperature effects are typically highly nonlinear, but effects can sometimes be compensated with measurements from an internal temper sensor.[18] Kuritsky and Goldstein[3] indicate that gyro bias thermal dependence can just be lumped in with other bias errors, and scale factor thermal dependence for RLGs is just a few PPM.

3.3.2 Vibration

Ideally, vibration is just another motion that needs to be measured by the IMU. Note that for radar, the antenna vibration needs to be measured, so the IMU should be rigidly mounted to the antenna.

Walchco and Mason[19] state "Vibration in a strap-down system can cause many problems with the INS." Kuritsky and Goldstein[3] indicate that vibration affects bias via sensor scale factor asymmetries. They also discuss specific manifestations called "coning" and "sculling" errors. Additionally, vibration frequency is very important. Since the accelerometers and gyros are sampled, excessively high vibration frequencies may alias to lower frequencies.

The usual treatment is to first mitigate any high-frequency resonances in the antenna assembly, and then to isolate the IMU from the vibration (e.g. shock mounting, etc.) Note that if isolation is required, then the entire antenna needs to be isolated. In any case, the vibration environment for the IMU needs to be determined and assessed.

3.3.3 Aging

As with any electronic equipment, one might expect some performance degradation with time.

3.3.4 Hysteresis

Walchco and Mason[19] describe hysteresis as the attribute of IMU parameters (especially biases) changing from one power-up to the next. Manufacturers sometimes call this "bias repeatability."

3.4 Aiding

Determining the orientation and position of the IMU accelerometers and rate gyros within a desired coordinate frame is termed 'alignment' of the IMU. But IMU's will eventually drift away from this alignment with time, due to the aforementioned error sources.

The alignment can often be maintained within some error bounds by monitoring other motion and attitude instruments, comparing their information with that of the IMU instruments, and adjusting IMU data accordingly. The reference measurements thereby 'aid' the IMU. This process is called 'aiding'.

Generally, the aiding instruments provide their 'truth' information at a cost of limited measurement rates, or excessive noisiness, so that their aiding is accomplished mainly in a statistical sense. Combining the aiding measurements to estimate IMU error components is generally done via a Kalman Filter (KF). More properly, since nonlinear functions are employed, the correct structure is termed an 'Extended' Kalman Filter (EKF).

A number of different aiding mechanisms have been employed in various systems. Several are briefly discussed. Others no doubt exist. This is not meant to be a comprehensive discussion of various aiding schemes, but rather just an acknowledgement that a variety of such schemes exist. Their suitability for SAR motion measurement is also not addressed. More comprehensive discussions can be found in the literature. Several are discussed in a chapter in a book by Siouris.[20]

3.4.1 Global Positioning System (GPS)

One of the more popular aiding schemes is GPS. Books have been written about this topic. Useful texts include Kaplan and Hegarty[21], and one by Grewal, et al.[22] In fact, this combination is so popular that they come as single instrument packages known as Embedded GPS/INS (EGI) units. However, even with GPS, a number of options exist. These include, among others

1. C/A code GPS
2. P code GPS
3. Differential GPS (DGPS)
4. Carrier-Phase GPS

One particular problem with GPS updates is that they come typically at one-second intervals, which is much less frequent than IMU data points. The GPS aiding needs to be applied in a manner to not cause large jumps or discontinuities in the motion measurement error. Recall that SAR autofocus works best on low-frequency phase (range) errors. Fuxiang and Zheng[23] describe aiding whereby GPS measurements are

directly compared to IMU calculations to subsequently calculate errors between the two, and allow correction of those errors. Their implementation optimally requires GPS updates to not be applied during the SAR synthetic aperture to avoid large jumps in the error. Alternatively, Kim, et al.[1], discuss aiding with P-Code Carrier-Phase GPS data, and address this by a dual navigator arrangement that couples the GPS to the IMU data via a tracking filter. In this manner, GPS updates can be applied during a synthetic aperture without problematic discontinuities.

Multi-antenna GPS systems have been proposed to facilitate attitude-aiding.

Other GPS-like systems exist. For example, the Russian Republic operates GLONASS; the European Union operates Galileo; India operates IRNSS and China operates BeiDou.

3.4.2 Transfer Alignment from HAINS system

Occasionally, a navigation-grade HAINS system already resides on the aircraft platform carrying the SAR system. In this case, the possibility exists to aid the SAR's indigenous IMU with the HAINS motion estimates. This is referred to as a 'Transfer Alignment'. This is the approach advocated by Kennedy.[24,25]

3.4.3 Star Tracker

Kuritsky and Goldstein[3] discuss aiding with stellar navigation (sighting stars). This is primarily for attitude aiding.

3.4.4 Magnetometer

Heading alignment can be aided by a magnetometer sensing the earth's magnetic field.

3.4.5 Radio Navigation Aids

Position errors can be bounded by traditional navigation systems that include TACAN, LORAN, Omega, VOR, DME, and JTIDS RelNav.

3.4.6 SAR Feedback

The SAR system itself may be used to aid the navigation. This would include clutter-locking and clutter-tracking schemes. Feedback of autofocus information has been postulated as a mechanism to estimate IMU bias errors.

Sequence of contiguous spotlight SAR images in a stripmap have been used to estimate and correct IMU yaw angle errors.[26,27]

Otherwise, the SAR system may in some cases be operated in special modes to measure specific motion parameters, such as velocity.[28]

3.4.7 Other Radar

Secondary radar systems may be used for motion data augmentation, such as Doppler navigation systems. This would include perhaps laser Doppler navigation.

Terrain matching systems can help bound position errors. This includes TERCOM systems.

3.4.8 A Note About S-Turns

As previously stated, an IMU is a collection of instruments that make six independent measurements; three translational motion elements (typically accelerometers), and three rotational motion elements (typically rate gyros). Each of these six instruments has its own biases with independent noise and drifts, i.e. its own error. Furthermore, there are the accumulated errors that also need to be corrected, that is, it is not sufficient to just stop further error growth, but the errors accumulated thus far also need to be corrected.

Consequently there are at least twelve independent unknown errors that need to be corrected by an aiding scheme. Any particular aiding scheme may not be sufficient to estimate and mitigate all of these errors independently. To correct all the unknown independent errors, we need at least that many relevant independent measurements, enough to discern and make observable the individual error components. Furthermore, since measurements are typically functions of errors in all dimensions, unless each error is made observable and identifiable, ambiguity exists for all others.

For example, consider a typical single GPS aiding scheme that provides three dimensions of position information, but not attitude information. We will simplify the subsequent analysis because our interest is to illustrate some points, not to provide detailed algorithmic design equations.

Presume for the moment that there are no rotational errors, that is, the orientation of the IMU is known. This allows GPS position measures to be related to specific IMU acceleration instruments. With multiple GPS measurements, individual motion dimensions and characteristics become observable, including accelerations. Linear motion errors (i.e. position, velocity, and acceleration) can be corrected, and accelerometer biases become apparent and can be compensated.

Now consider accelerations in the presence of small rotational errors. We return to the notation in Section 2, where the measured acceleration was related to instrument acceleration as

$$\mathbf{a}_m(t) = \mathbf{R}_m(t)\mathbf{a}'_m(t). \tag{105}$$

This can be expanded to a dependence on true and error rotations and accelerations as

$$\mathbf{a}_m(t) = (\mathbf{R}_t(t) + \mathbf{R}_\varepsilon(t))(\mathbf{a}'_t(t) + \mathbf{a}'_\varepsilon(t)). \tag{106}$$

For expedience in this development, we will assume that the acceleration errors in the instrument frame are known to be (or adequately modeled as) zero, that is

$$\mathbf{a}'_{\varepsilon}(t) = \mathbf{0}. \tag{107}$$

Furthermore, we will presume that the radar frame is the same as the IMU coordinate frame. This allows

$$\mathbf{R}_t(t) = \mathbf{I}. \tag{108}$$

We will also assume that the rotational error is a constant, as if a significant accumulated error that changes very little more during the time period of interest. This is notated as

$$\mathbf{R}_{\varepsilon}(t) = \mathbf{R}_{\varepsilon}(0). \tag{109}$$

Consequently, the IMU measured accelerations are then related to true accelerations as

$$\mathbf{a}_m(t) = \left(\mathbf{I} + \mathbf{R}_{\varepsilon}(0)\right)\mathbf{a}'_t(t). \tag{110}$$

Expanding the $\left(\mathbf{I} + \mathbf{R}_{\varepsilon}(0)\right)$ term yields the equation

$$\mathbf{a}_m = \begin{bmatrix} 1 & \Delta\theta_{z',\varepsilon} & -\Delta\theta_{y',\varepsilon} \\ -\Delta\theta_{z',\varepsilon} & 1 & \Delta\theta_{x',\varepsilon} \\ \Delta\theta_{y',\varepsilon} & -\Delta\theta_{x',\varepsilon} & 1 \end{bmatrix} \mathbf{a}'_t, \tag{111}$$

where we have dropped the explicit references to time as an argument to the various factors and elements of the equation. This is just to avoid clutter in the equations.

Nevertheless, this equation indicates that a true acceleration is perturbed by instrument orientation errors for any measured acceleration. It also suggests that if for some number of measured values $\mathbf{a}_m$ we can identify corresponding 'truth' values $\mathbf{a}'_t$ divined from an 'aiding' source, then we might be able to identify the various components of the rotation matrix. This is, in fact, the plan.

To proceed, we shall presume for simplicity that these coordinate frames align with the North-East-Down (NED) frame, where

positive *x'* = north,
positive *y'* = east,
positive *z'* = down. (112)

In our NED frame, consider straight and level flight. No horizontal accelerations are present. Only gravity is sensed, and we know it points down. Consequently

$$\mathbf{a}_m = \begin{bmatrix} 1 & \Delta\theta_{z',\varepsilon} & -\Delta\theta_{y',\varepsilon} \\ -\Delta\theta_{z',\varepsilon} & 1 & \Delta\theta_{x',\varepsilon} \\ \Delta\theta_{y',\varepsilon} & -\Delta\theta_{x',\varepsilon} & 1 \end{bmatrix} \begin{bmatrix} 0 \\ 0 \\ g \end{bmatrix} = \begin{bmatrix} -\Delta\theta_{y',\varepsilon} g \\ \Delta\theta_{x',\varepsilon} g \\ g \end{bmatrix}. \tag{113}$$

Note that angular errors about the *x'* and *y'* axes are observable and measurable. These typically correspond to combinations of 'pitch' and 'roll'. However, the rotational error about the *z'* axis is not observable at all. This typically corresponds to 'yaw', and is often referred to as 'heading error'. Heading error is the problem child of GPS aiding. It seems to manifest itself mainly as an antenna pointing error. We discuss this more later.

Now consider a sequence of measurements where we define

$$\mathbf{A}_m = \begin{bmatrix} \mathbf{a}_{m1} & \mathbf{a}_{m2} & \mathbf{a}_{m3} & \ldots \end{bmatrix}. \tag{114}$$

Furthermore, for each measured vector we have a 'truth' vector, which we derive from GPS measurements, and collect as

$$\mathbf{A}'_t = \begin{bmatrix} \mathbf{a}'_{t1} & \mathbf{a}'_{t2} & \mathbf{a}'_{t3} & \ldots \end{bmatrix}. \tag{115}$$

The equation relating the two collections of accelerations is

$$\mathbf{A}_m = \begin{bmatrix} 1 & \Delta\theta_{z',\varepsilon} & -\Delta\theta_{y',\varepsilon} \\ -\Delta\theta_{z',\varepsilon} & 1 & \Delta\theta_{x',\varepsilon} \\ \Delta\theta_{y',\varepsilon} & -\Delta\theta_{x',\varepsilon} & 1 \end{bmatrix} \mathbf{A}'_t. \tag{116}$$

In general, the matrices $\mathbf{A}_m$ and $\mathbf{A}'_t$ are not square, consequently we need to employ the pseudo-inverse to calculate the rotation matrix

$$\begin{bmatrix} 1 & \Delta\theta_{z',\varepsilon} & -\Delta\theta_{y',\varepsilon} \\ -\Delta\theta_{z',\varepsilon} & 1 & \Delta\theta_{x',\varepsilon} \\ \Delta\theta_{y',\varepsilon} & -\Delta\theta_{x',\varepsilon} & 1 \end{bmatrix} = \mathbf{A}_m \left(\mathbf{A}'_t\right)^T \left(\mathbf{A}'_t \left(\mathbf{A}'_t\right)^T\right)^{-1}. \tag{117}$$

This places some special requirements on $\mathbf{A}'_t$. First, we need at least three measurement vectors. Second, the measurement vectors need to be mathematically independent. This implies that no number of measurements of a constant acceleration is suitable for determining the orientation error matrix. We need at least three acceleration situations where the accelerations are different enough to provide mathematically independent conditions. This is required for the pseudo-inverse to exist. Third, to be independent, we need different non-zero horizontal accelerations in both the North and East directions for some of these measurements.

So, this means that we need a variety of accelerations in the horizontal plane, with variations in North and East, to make heading error observable. This implies a maneuvering platform. Since GPS measurements are themselves noisy, and using the pseudo-inverse calculates a least-mean-squared-error fit to the data, we would like many such measurements to help beat down the noise, i.e. uncertainty. Since GPS measurements come at Hz rates, this implies that the maneuvering needs to be over a number of seconds, the more the better. And finally, Since GPS measurements have limited precision relative to the IMU, we need fairly large horizontal accelerations and motions generated to also help overcome the noise in the GPS measurements. For all these reasons, periodic sustained turns with substantial lateral accelerations are desired to mitigate heading errors in GPS-aided inertial navigation systems. These turns may be part of platform course corrections, dog-bone flight paths, racetracks, or may be prescribed S-turns, or any other maneuver that generates many independent-acceleration GPS updates. Anecdotal evidence suggests that with the IMU held rigid to the aircraft body, the IMU needs to see 1/3 -1/2 G minimum for up to 30-60 seconds.

We also note that in an aiding scheme for an IMU, accelerometer errors and angular errors are all calculated simultaneously by the EKF, which seeks to simultaneously minimize the mean-squared-error influence of all IMU errors when compared to multiple GPS measurements.

The natural question to ask is “How do we maintain heading alignment during straight and level flight?” We leave this question with the simplistic answer “with an additional instrument of some sort that makes the heading error observable.” One answer is an aiding scheme that uses SAR stripmaps themselves, as reported by Doerry[26], and Marquette, et al.[27]

As a final note, we address a point of occasional confusion. The term ‘heading’ as applied in this analysis is not to be confused with the direction of travel of the radar. Rather, it is the orientation of the radar about the vertical axis, regardless of the direction of travel.

“Your present circumstances don't determine where you can go;
they merely determine where you start.”
-- Nido Qubein

4 Expected Motion Measurement Error Behavior

In this section we combine the results of the previous two sections, and develop a relationship between IMU instrument errors and the ultimate navigation error of the IMU subsystem.

4.1 Navigator Position Error

The question here is "How do IMU instrument errors affect navigator position error?"

From Section 2 we recall that the net acceleration error was given by

$$\mathbf{a}_\varepsilon(t) \approx \mathbf{R}_t(t)\,\mathbf{a}'_\varepsilon(t) + \mathbf{R}_\varepsilon(t)\,\mathbf{a}'_t(t). \tag{118}$$

where $\mathbf{a}'_t(t)$ includes gravity. This is integrated to find velocity error and position error, that is

$$\begin{aligned}
&\mathbf{v}_\varepsilon(t) = \int_0^t \mathbf{a}_\varepsilon(\tau)d\tau + \mathbf{v}_\varepsilon(0), \text{ and} \\
&\mathbf{p}_\varepsilon(t) = \int_0^t \mathbf{v}_\varepsilon(\tau)d\tau + \mathbf{p}_\varepsilon(0).
\end{aligned} \tag{119}$$

These results can be combined into

$$\mathbf{p}_\varepsilon(t) = \int_0^t\int \mathbf{R}_t(\tau)\mathbf{a}'_\varepsilon(\tau)d\tau d\tau + \int_0^t\int \mathbf{R}_\varepsilon(\tau)\mathbf{a}'_t(\tau)d\tau d\tau + \int_0^t \mathbf{v}_\varepsilon(0)d\tau + \mathbf{p}_\varepsilon(0). \tag{120}$$

To simplify the following analysis, we will assume that at time $t = 0$ we have no velocity, position, or rotation errors. That is

$$\begin{aligned}
&\mathbf{v}_\varepsilon(0) = \mathbf{0}, \\
&\mathbf{p}_\varepsilon(0) = \mathbf{0}, \text{ and} \\
&\mathbf{R}_\varepsilon(0) = \mathbf{0}.
\end{aligned} \tag{121}$$

Furthermore, consistent with our assumption that all accelerometer and rate gyro instruments have equal performance, we will assume that expected error performance does not depend on specific instrument or system orientation. Consequently we will assume the convenience of the IMU instruments oriented in the radar frame. That is

$$\mathbf{R}_t(t) = \mathbf{I}. \tag{122}$$

Combining these yields

$$\mathbf{p}_{\varepsilon}(t) = \int_0^t \int \mathbf{a}'_{\varepsilon}(\tau)\, d\tau d\tau + \int_0^t \int \mathbf{R}_{\varepsilon}(\tau)\mathbf{a}'_{t}(\tau)\, d\tau d\tau \,. \tag{123}$$

We will also assume that accelerations are dominated by gravity. That is

$$\mathbf{a}'_t(t) \approx \mathbf{a}'_g(t). \tag{124}$$

Although we know the magnitude of this vector, we do not necessarily know its orientation in the radar frame. So, for now we will leave the more generic expression $\mathbf{a}'_t(t)$ in the equation, although we will make use of the approximation of this as a constant.

Now consider a specific component of the position error, namely the component in the *y* direction of the radar frame. This error component can be extracted and described as

$$p_{y,\varepsilon}(t) = \int_0^t \int a_{y',\varepsilon}(\tau)\, d\tau d\tau + \int_0^t \int \left(a_{z',t} \int \omega_{x',\varepsilon}(\tau) d\tau - a_{x',t} \int \omega_{z',\varepsilon}(\tau) d\tau \right) d\tau d\tau \,. \tag{125}$$

This allows the expansion to

$$p_{y,\varepsilon}(t) = \int_0^t \int a_{y',\varepsilon}(\tau)\, d\tau d\tau + a_{z',t} \int_0^t \int \int \omega_{x',\varepsilon}(\tau)\, d\tau d\tau d\tau - a_{x',t} \int_0^t \int \int \omega_{z',\varepsilon}(\tau)\, d\tau d\tau d\tau \,. \tag{126}$$

A tacit assumption here is that the angles, and angular rates are in terms of radians rather than degrees.

From Section 3 we recall that the acceleration error and angular rate error in the IMU instruments are given by

$$a_{\varepsilon} = |a_t| \mathrm{B}_{\max} + a_{\perp} \sin(\varphi_m + \varphi_n) + n_{a,0} + n_{a,1} + n_{a,2}\,, \text{ and}$$

$$\omega_{\varepsilon} = |\omega_t| \Gamma_{\max} + \omega_{\perp} \sin(\phi_m + \phi_n) + n_{\omega,0} + n_{\omega,1} + n_{\omega,2}\,. \tag{127}$$

We add some instrument axis subscripts, and combine with the earlier result to yield

$$p_{y,\varepsilon}(t)=\begin{bmatrix} \int_0^t\int\left(\left(a_{y',t}\left|\mathrm{B}_{\max}+a_{y',\perp}\sin(\varphi_m+\varphi_n)+n_{y',a,0}+n_{y',a,1}+n_{y',a,2}\right)d\tau d\tau\right. \\ +a_{z',t}\int_0^t\iint\left(\begin{matrix}\left|\omega_{x',t}\right|\Gamma_{\max}+\omega_{x',\perp}\sin(\phi_m+\phi_n)\\ +n_{x',\omega,0}+n_{x',\omega,1}+n_{x',\omega,2}\end{matrix}\right)d\tau d\tau d\tau \\ -a_{x',t}\int_0^t\iint\left(\begin{matrix}\left|\omega_{z',t}\right|\Gamma_{\max}+\omega_{z',\perp}\sin(\phi_m+\phi_n)\\ +n_{z',\omega,0}+n_{z',\omega,1}+n_{z',\omega,2}\end{matrix}\right)d\tau d\tau d\tau \end{bmatrix}. \tag{128}$$

We note that the perpendicular components are calculated as

$$\begin{aligned} a_{y',\perp}&=\sqrt{{a_{z',t}}^2+{a_{x',t}}^2}\,,\\ \omega_{x',\perp}&=\sqrt{{\omega_{y',t}}^2+{\omega_{z',t}}^2}\,,\text{ and}\\ \omega_{z',\perp}&=\sqrt{{\omega_{x',\perp}}^2+{\omega_{y',t}}^2}\,. \end{aligned} \tag{129}$$

These quantities may be either positive or negative, but the sign is immaterial to our purposes. We also recall that the models for $n_{y',a,2}$, $n_{x',\omega,2}$, and $n_{z',\omega,2}$ are themselves integrals of white noise.

Our assumption of accelerations dominated by gravity constrains

$$\begin{aligned} \left|a_{x',t}\right|&\le g\,,\\ \left|a_{y',t}\right|&\le g\,,\text{ and}\\ \left|a_{z',t}\right|&\le g\,. \end{aligned} \tag{130}$$

Furthermore, even more constraining, we limit

$$\left|a_{y',\perp}\right|\le g\,. \tag{131}$$

While this development was specifically for the *y*-axis component $p_{y,\varepsilon}(t)$, a similar development is readily performed to provide an expression for $p_{x,\varepsilon}(t)$ and $p_{z,\varepsilon}(t)$.

At this point we have related IMU instrument characteristics to position error. The goal is to ultimately develop requirements or limitations for IMU instrument parameters based on allowable limits for position error. This requires knowing the position error limits. Position error limits are calculated in Section 5.

4.2 Navigator Orientation Error

The question here is "How do IMU instrument errors affect navigator orientation error?"

The error in navigator orientation are the elements of the rotation matrix error $\mathbf{R}_\varepsilon(t)$. Recall from Section 2 that this is calculated as

$$\mathbf{R}_\varepsilon(t) = \mathbf{R}_\varepsilon(0) + \mathbf{R}_t(0)\begin{bmatrix} 0 & \int_0^t \omega_{z',\varepsilon}(\tau)d\tau & -\int_0^t \omega_{y',\varepsilon}(\tau)d\tau \\ -\int_0^t \omega_{z',\varepsilon}(\tau)d\tau & 0 & \int_0^t \omega_{x',\varepsilon}(\tau)d\tau \\ \int_0^t \omega_{y',\varepsilon}(\tau)d\tau & -\int_0^t \omega_{x',\varepsilon}(\tau)d\tau & 0 \end{bmatrix}. \qquad (132)$$

As with accelerations, we will assume no initial errors, and the same initial rotation. That is, we will assume

$$\mathbf{R}_\varepsilon(0) = \mathbf{0}, \text{ and}$$
$$\mathbf{R}_t(0) = \mathbf{I}. \qquad (133)$$

This allows the simplification

$$\mathbf{R}_\varepsilon(t) = \begin{bmatrix} 0 & \int_0^t \omega_{z',\varepsilon}(\tau)d\tau & -\int_0^t \omega_{y',\varepsilon}(\tau)d\tau \\ -\int_0^t \omega_{z',\varepsilon}(\tau)d\tau & 0 & \int_0^t \omega_{x',\varepsilon}(\tau)d\tau \\ \int_0^t \omega_{y',\varepsilon}(\tau)d\tau & -\int_0^t \omega_{x',\varepsilon}(\tau)d\tau & 0 \end{bmatrix}. \qquad (134)$$

Consequently, an individual instrument's angular rate error causes growth with time in the angular error itself. Our initial conditions have allowed associating a specific instrument angular rate with a particular angular displacement. Specifically, from Section 2 , the angular displacement errors can be calculated as

$$\Delta\theta_{x',\varepsilon}(t) = \int_0^t \omega_{x',\varepsilon}(\tau)d\tau\,,$$

$$\Delta\theta_{y',\varepsilon}(t) = \int_0^t \omega_{y',\varepsilon}(\tau)d\tau\,, \text{ and}$$

$$\Delta\theta_{z',\varepsilon}(t) = \int_0^t \omega_{z',\varepsilon}(\tau)d\tau\,. \tag{135}$$

From Section 3 we recall that an instrument's angular rate error can be modeled as

$$\omega_\varepsilon = |\omega_t|\Gamma_{\max} + \omega_\perp \sin(\phi_m + \phi_n) + n_{\omega,0} + n_{\omega,1} + n_{\omega,2}\,. \tag{136}$$

Choosing one of the angular displacement error components, for example the *z'* axis, we can compute the angular (orientation) error as

$$\Delta\theta_{z',\varepsilon}(t) = \int_0^t \left(|\omega_{z',t}|\Gamma_{\max} + \omega_{z',\perp}\sin(\phi_m + \phi_n) + n_{z',\omega,0} + n_{z',\omega,1} + n_{z',\omega,2}\right)d\tau\,. \tag{137}$$

As with acceleration, we also recall that the model for $n_{z',\omega,2}$ is itself an integral of white noise. In addition, we identify

$$\omega_{z',\perp} = \sqrt{{\omega_{x',\perp}}^2 + {\omega_{y',t}}^2}\,, \tag{138}$$

and note that the sign may be either positive or negative.

At this point we have related IMU instrument characteristics to orientation error. The goal is to ultimately develop requirements or limitations for IMU instrument parameters based on allowable limits for orientation error. This requires knowing the orientation error limits. Orientation error limits are calculated in Section 5.

"A good hockey player plays where the puck is.
A great hockey player plays where the puck is going to be."
-- Wayne Gretzky

5 Radar Geometry

In this section we examine the effects of motion measurement errors on a SAR image.

The radar uses motion data in two principal manners

1. Motion Compensation of the radar data, and
2. Pointing of the radar antenna.

The aspects of motion measurement used for each is illustrated in Figure 7.

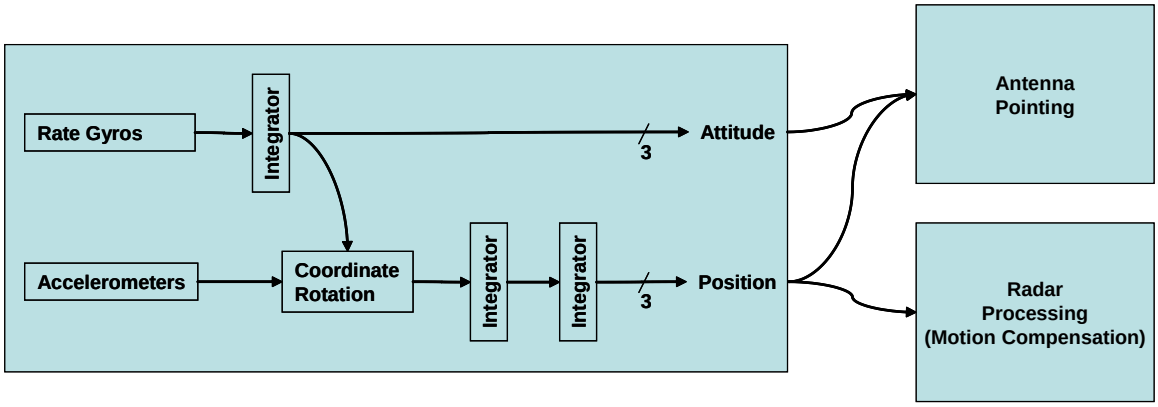

Figure 7. Motion information is used by the radar for two principal purposes, 1) antenna pointing, and 2) motion compensation of the radar data.

5.1 Motion Compensation

A SAR image is composed of pixels, where each pixel corresponds to a specific scene location, and the intensity of the pixel is a function of the echo energy from that scene location. In particular, the optimal estimate of the echo energy is calculated via a matched filter, that is, the raw radar data filtered to that specific location in the minimum mean-squared error sense. The matched filter necessarily compensates for the range to the target point and how it varies during the radar's synthetic aperture, that is a collection of positions along the radar's flight path. An error in measured position corresponds to an error in the matched filter, which alters the echo energy estimate for that location away from optimum.

5.1.1 Range Error

The radar's greatest sensitivity to position error is in the direction towards (or away from) the target location of interest, that is, a line-of-sight range error.

Consequently, we now specifically examine the effects of a range error function on the output of a range-Doppler matched filter.

Consider a radar transmitted signal of the form

$$X_T(t) = \sum_n \text{rect}\left(\frac{t - t_n}{T}\right) \exp\left(j\left(2\pi f_0 (t - t_n) + \phi(t - t_n)\right)\right), \tag{139}$$

where

t = time,
n = pulse number, $-N/2 \le n < N/2$,
t_n = reference time of the nth pulse,
T = pulse width,
f_0 = nominal center frequency of the pulses, and
$\phi(\tau)$ = phase modulation function of the pulse. (140)

We will assume that $\phi(\tau)$ is analytic over the pulse width. This is reasonable for waveforms such as chirps.

Neglecting attenuation, the received signal from a point target is identified as

$$X_R(t) = X_T\left(t - \frac{2}{c} r_s(t)\right), \tag{141}$$

where

$r_s(t) = |\mathbf{r}_s(t)|$, and
$\mathbf{r}_s(t)$ = vector relating the true location of the radar from the target point. (142)

The variation of $\mathbf{r}_s(t)$ in both length and direction defines the synthetic aperture.

The matched filter for the target point will be based on measured position of the radar with respect to the target point, consequently the filter function is

$$X_M(t) = X_T\left(t - \frac{2}{c} r_m(t)\right), \tag{143}$$

where

$r_m(t) = |\mathbf{r}_m(t)|$, and

$\mathbf{r}_m(t)$ = vector relating the measured location of the radar from the target point.

(144)

The optimum matched filter output for that scene location is then identified as

$$x_o = \int_t X_R(t) X_M^*(t) dt \,. \tag{145}$$

This can be expanded to

$$x_o = \int_t \sum_n \left[\begin{array}{l} \text{rect}\left(\dfrac{t - \frac{2}{c} r_s(t) - t_n}{T} \right) \exp\left(j \left(\begin{array}{l} 2\pi f_0 \left(t - \frac{2}{c} r_s(t) - t_n \right) \\ + \varphi\left(t - \frac{2}{c} r_s(t) - t_n \right) \end{array} \right) \right) \\ \times \text{rect}\left(\dfrac{t - \frac{2}{c} r_m(t) - t_n}{T} \right) \exp\left(-j \left(\begin{array}{l} 2\pi f_0 \left(t - \frac{2}{c} r_m(t) - t_n \right) \\ + \varphi\left(t - \frac{2}{c} r_m(t) - t_n \right) \end{array} \right) \right) \end{array} \right] dt \,. \tag{146}$$

If we make the reasonable assumption that the range error isn't too big, that is

$$\frac{2}{c} |r_s(t) - r_m(t)| << T \,, \tag{147}$$

Then the matched filter output can be approximated by

$$x_o \approx \sum_n \int_t \left[\begin{array}{l} \text{rect}\left(\dfrac{t - \frac{2}{c} r_s(t) - t_n}{T} \right) \\ \times \exp\left(j \left(\begin{array}{l} -4\pi \frac{f_0}{c} \left(r_s(t) - r_m(t) \right) \\ + \phi\left(t - \frac{2}{c} r_s(t) - t_n \right) - \phi\left(t - \frac{2}{c} r_m(t) - t_n \right) \end{array} \right) \right) \end{array} \right] dt \,. \tag{148}$$

Another reasonable approximation for this analysis is that the ranges do not vary significantly during any one single pulse. While this is not adequate for high-performance SAR image formation, it will suffice for the analysis at hand. This allows the substitutions

$\mathbf{r}_s(t) \to \mathbf{r}_s(t_n)$, and
$\mathbf{r}_m(t) \to \mathbf{r}_m(t_n)$. (149)

We also define

$\lambda = c/f_0$ = the nominal wavelength of the radar. (150)

The model for the matched filter output becomes

$$x_o \approx \sum_n \exp\left(-j\frac{4\pi}{\lambda}\left(r_s(t_n) - r_m(t_n)\right)\right)\int_t \left[\begin{array}{l} \text{rect}\left(\dfrac{t-\frac{2}{c}r_s(t_n)-t_n}{T}\right) \\ \times \exp\left(j\left(\begin{array}{l}\phi\left(t-\frac{2}{c}r_s(t_n)-t_n\right) \\ -\phi\left(t-\frac{2}{c}r_m(t_n)-t_n\right)\end{array}\right)\right)\end{array}\right] dt\,. \quad (151)$$

We now identify the range error as the difference between measured and true values

$r_\varepsilon(t_n) = r_m(t_n) - r_s(t_n)$. (152)

This allows the matched filter output to become

$$x_o \approx \sum_n \exp\left(j\frac{4\pi}{\lambda}r_\varepsilon(t_n)\right)\int_t \left[\begin{array}{l} \text{rect}\left(\dfrac{t-\frac{2}{c}r_s(t_n)-t_n}{T}\right) \\ \times \exp\left(j\left(\begin{array}{l}\phi\left(t-\frac{2}{c}r_s(t_n)-t_n\right) \\ -\phi\left(t-\frac{2}{c}r_s(t_n)-t_n-\frac{2}{c}r_\varepsilon(t_n)\right)\end{array}\right)\right)\end{array}\right] dt\,. \quad (153)$$

At this point we make the Taylor series expansion

$$\phi\left(t-\frac{2}{c}r_s(t_n)-t_n-\frac{2}{c}r_\varepsilon(t_n)\right) \approx \phi\left(t-\frac{2}{c}r_s(t_n)-t_n\right) - \phi'\left(t-\frac{2}{c}r_s(t_n)-t_n\right)\frac{2}{c}r_\varepsilon(t_n). \quad (154)$$

This allows the matched filter output to be approximated as

$$x_o \approx \sum_n \exp\left(j\frac{4\pi}{\lambda} r_\varepsilon(t_n) \right) \int_t \left[\begin{array}{l} \mathrm{rect}\left(\dfrac{t - \dfrac{2}{c} r_s(t_n) - t_n}{T} \right) \\ \times \exp\left(j\varphi'\left(t - \dfrac{2}{c} r_s(t_n) - t_n \right) \dfrac{2}{c} r_\varepsilon(t_n) \right) \end{array} \right] dt \,. \qquad (155)$$

We identify the integral as the operation of 'range compression'. The exponential outside of the integral is the Doppler term.

For the range resolution of this signal to be determined by the modulation $\phi(\tau)$, then $\phi(\tau)$ needs to have bandwidth substantially larger than that of the pulse itself (i.e. 1/*T*). This is generally the case with modern SAR systems.

For a Linear FM (LFM) chirp waveform, we identify

$$\begin{aligned} &\phi(\tau) = 2\pi \frac{\gamma}{2} \tau^2 \text{, and} \\ &\phi'(\tau) = 2\pi\gamma\tau \,, \end{aligned} \qquad (156)$$

where

$$\gamma \text{ = the chirp rate in Hz/sec.} \qquad (157)$$

For this modulation, the matched filter output will be

$$x_o \approx \sum_n \exp\left(j\frac{4\pi}{\lambda} r_\varepsilon(t_n) \right) \int_t \left[\begin{array}{l} \mathrm{rect}\left(\dfrac{t - \dfrac{2}{c} r_s(t_n) - t_n}{T} \right) \\ \times \exp\left(j\dfrac{4\pi}{c}\gamma \left(t - \dfrac{2}{c} r_s(t_n) - t_n \right) r_\varepsilon(t_n) \right) \end{array} \right] dt \,. \qquad (158)$$

A change of variable allows the simplified form

$$x_o \approx \sum_n \exp\left(j\frac{4\pi}{\lambda} r_\varepsilon(t_n) \right) \int_{t'} \mathrm{rect}\left(\frac{t'}{T} \right) \exp\left(j\frac{4\pi}{c}\gamma r_\varepsilon(t_n) t' \right) dt' \,. \qquad (159)$$

The integration is readily performed, and yields

$$x_o \approx \sum_n \exp\left(j\frac{4\pi}{\lambda} r_\varepsilon(t_n) \right) T \,\mathrm{sinc}\left(\frac{2\gamma T}{c} r_\varepsilon(t_n) \right). \qquad (160)$$

However, we also identify

$$\frac{c}{2\gamma T} = \rho_r \text{ = range resolution of the radar.} \tag{161}$$

This allows the matched filter output to be expressed as

$$x_o \approx T\sum_n \text{sinc}\left(\frac{r_\varepsilon(t_n)}{\rho_r}\right)\exp\left(j\frac{4\pi}{\lambda}r_\varepsilon(t_n)\right). \tag{162}$$

There are two mechanisms by which $r_\varepsilon(t_n)$ influences the matched filter output, and hence SAR image quality,

1. by the phase modulation term $\exp\left(j\frac{4\pi}{\lambda}r_\varepsilon(t_n)\right)$, and

2. by the amplitude, or migration, term $\text{sinc}\left(\frac{r_\varepsilon(t_n)}{\rho_r}\right)$.

For the matched filter to adequately 'integrate', each of these needs to be suitably small, or at least correctable to something suitably small, over the course of the synthetic aperture. Indeed, for negligible error, or $r_\varepsilon(t_n)\approx 0$, we have

$$x_o \approx TN\,. \tag{163}$$

Excessive errors $r_\varepsilon(t_n)$ during the pulse integration interval (synthetic aperture) will result in suboptimal matched filter performance. The issue is really how $r_\varepsilon(t_n)$ varies during the course of the synthetic aperture.

We have made the tacit assumption that phase error is proportional to $r_\varepsilon(t_n)$ alone. The implication is that no other factors influence phase error, such as atmospheric effects along the path between radar and target scene. This is not strictly true, as Dickey, et al.,[29] have shown that phase errors due to atmospheric effects are in fact quite common, and especially significant in long-range SAR images at shallow grazing angles. In such situations, even perfect motion measurement is unable to provide sufficient information to adequately focus a SAR image.

Furthermore, we need to be mindful that there is a difference between real range errors due to position inaccuracies, and apparent range errors due to radar measurements impacted by atmospheric effects.[30] We will ignore these atmospheric effects henceforth.

5.1.2 Relating Range Error to Position Error

The range error from the previous section can be related to vector quantities as

$$r_\varepsilon(t_n) = |\mathbf{r}_m(t_n)| - |\mathbf{r}_s(t_n)| = |\mathbf{r}_s(t_n) + \mathbf{r}_\varepsilon(t_n)| - |\mathbf{r}_s(t_n)|, \tag{164}$$

where the error vector is defined as

$$\mathbf{r}_\varepsilon(t_n) = \mathbf{r}_m(t_n) - \mathbf{r}_s(t_n). \tag{165}$$

We can expand the range error to

$$r_\varepsilon(t_n) = \sqrt{|\mathbf{r}_s(t_n)|^2 + 2\mathbf{r}_s(t_n) \circ \mathbf{r}_\varepsilon(t_n) + |\mathbf{r}_\varepsilon(t_n)|^2} - |\mathbf{r}_s(t_n)|. \tag{166}$$

A Taylor series expansion for small errors allows the approximation

$$r_\varepsilon(t_n) \approx \frac{\mathbf{r}_s(t_n) \circ \mathbf{r}_\varepsilon(t_n)}{|\mathbf{r}_s(t_n)|} + \frac{|\mathbf{r}_\varepsilon(t_n)|^2}{2|\mathbf{r}_s(t_n)|}. \tag{167}$$

For a matched filter implementation, the range error vector is simply the position error vector, namely

$$\mathbf{r}_\varepsilon(t_n) = \mathbf{p}_\varepsilon(t_n). \tag{168}$$

Consequently, we identify the range error itself as

$$r_\varepsilon(t_n) \approx \mathbf{n}_s(t_n) \circ \mathbf{p}_\varepsilon(t_n) + \frac{|\mathbf{p}_\varepsilon(t_n)|^2}{2|\mathbf{r}_s(t_n)|}, \tag{169}$$

where the unit vector in the range direction of $\mathbf{r}_s(t_n)$ is defined as

$$\mathbf{n}_s(t_n) = \frac{\mathbf{r}_s(t_n)}{|\mathbf{r}_s(t_n)|}. \tag{170}$$

Some observations are worth noting.

- Any position error in the direction of the target point translates directly into a range error, and ultimately a phase error. Nice to know that the math backs an obvious behavior.
- Less obvious, any position error in any direction at all translates via a square-law relationship to a range error. That is, for example, a linear position error (say, an along-track constant velocity error) translates into a quadratic range error, and hence a quadratic phase error.

5.1.3 Synthetic Aperture Time

Since range errors may accrue with time, an important question becomes "What is the time period for range errors to accrue?" This is essentially the question "What is the pulse integration interval, or synthetic aperture time?"

For broadside imaging, the synthetic aperture length is given by

$$L_{a,\perp} = \frac{a_w \lambda r_s(t_0)}{2\rho_a}, \tag{171}$$

where

t_0 = the nominal time when the radar is at the center of the synthetic aperture,
ρ_a = the desired azimuth resolution of the SAR image, and
a_w = Impulse Response (IPR) mainlobe broadening factor due to aperture weighting. (172)

Typically for many SAR systems, $a_w \approx 1.2$. More generally, the synthetic aperture length is given approximately by

$$L_a \approx \frac{a_w \lambda r_s(t_0)}{2\rho_a \sin\phi_s}, \tag{173}$$

where

ϕ_s = squint angle from radar platform heading, in the ground plane. (174)

With the radar traveling at some nominal velocity, the synthetic aperture time is given approximately by

$$T_a = \frac{L_a}{v_a} \approx \frac{a_w \lambda r_s(t_0)}{2\rho_a v_a \sin\phi_s}, \tag{175}$$

where

v_a = nominal radar velocity in direction of synthetic aperture. (176)

We note that the synthetic aperture time T_a is a strong function of each of wavelength, imaging geometry, desired resolution, and platform velocity. Figure 8 plots aperture times versus velocity for several ranges, with 0.3 m resolution broadside imaging. Figure 9 plots aperture times versus velocity for several ranges, with 0.1 m resolution broadside imaging.

Some specific examples:

1. For Ku-band, 10 km range, broadside imaging, 0.3 m resolution, and 50 m/s velocity, $T_a \approx 7.2$ seconds.

2. For Ku-band, 25 km range, 45 degree squint imaging, 0.1 m resolution, and 36 m/s velocity, $T_a \approx 106$ seconds.

If position errors accrue with time, then shorter (in time) synthetic apertures will allow less position error changes during a synthetic aperture. This implies that radars on faster vehicles will have lesser problems with drifting IMU errors.

Some published typical aircraft cruising velocities are given in the following table.

Table 1. Typical aircraft cruise velocities.

Aircraft	***Typical Cruise***
Lockheed F-16A Falcon	258 m/s
Lockheed P-3 Orion	170 m/s
Beechcraft King Air	149 m/s
De Havilland DHC-6 Twin Otter	74 m/s
General Atomics MQ-9 Reaper	87 m/s
General Atomics MQ-1 Predator A	36 m/s
AAI RQ-7 Shadow 200	31 m/s (loiter)

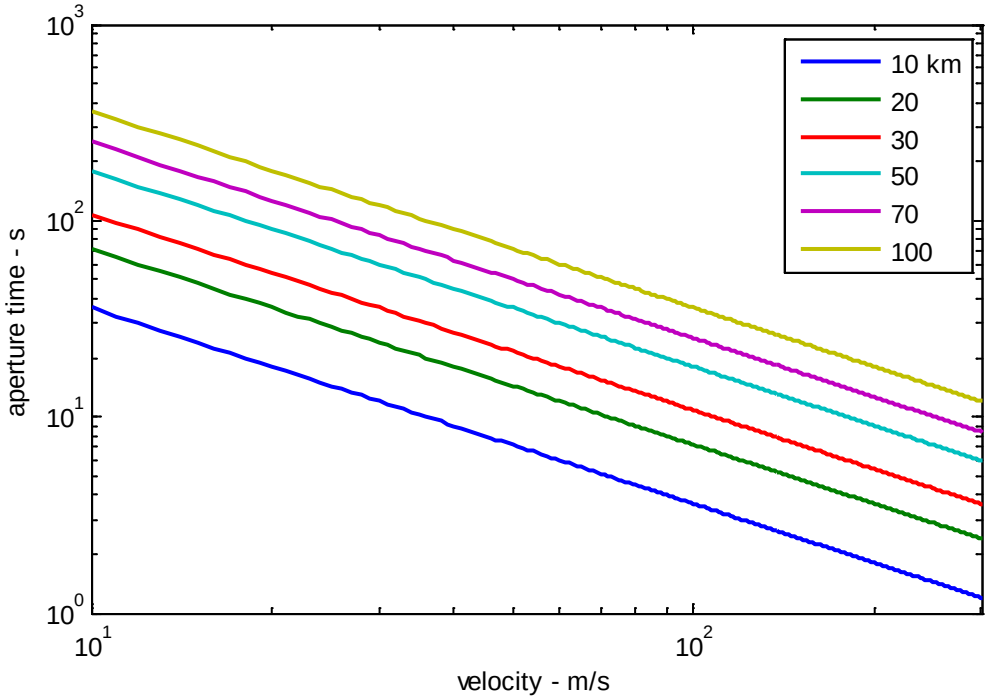

Figure 8. Aperture time versus velocity for broadside imaging at select ranges with 0.3 m resolution.

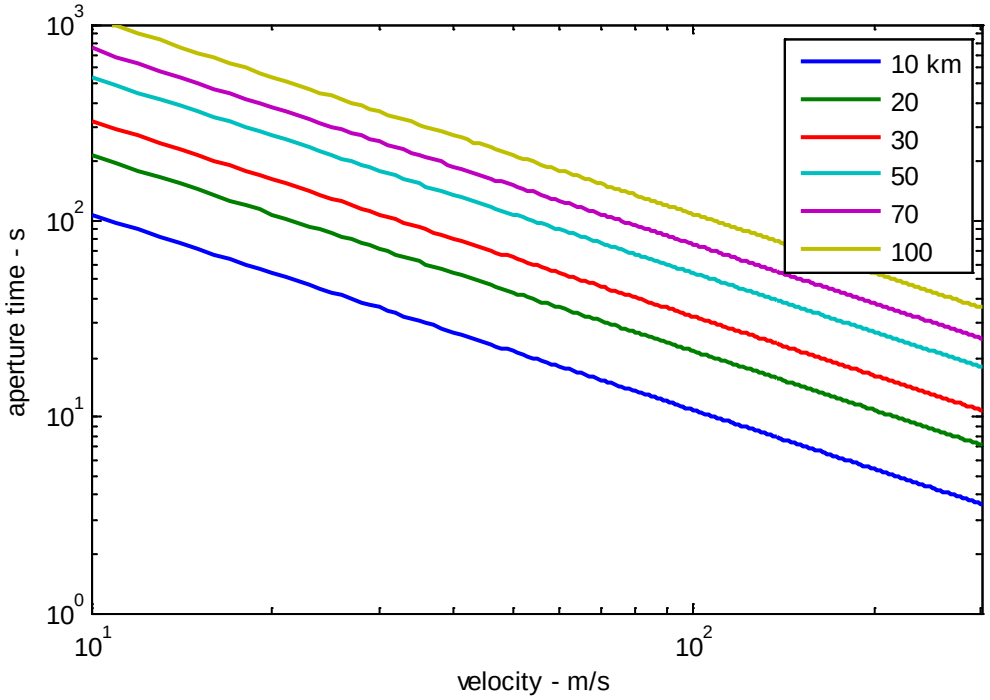

Figure 9. Aperture time versus velocity for broadside imaging at select ranges with 0.1 m resolution.

5.1.4 Limits with Autofocus

We now examine how increasing levels of range error $r_\varepsilon(t_n)$ influence SAR image quality. The key issue with radar geometry is "How much range error is allowable?"

The principal measure of image quality affected by range errors is the IPR. The IPR is discussed in some detail in a prior report.[31]

Most SAR systems deal with the effects of residual motion errors via a blind deconvolution operation on the image. This is generally referred to as 'Autofocus'. Various autofocus schemes and strategies are able to cope with differing amounts of data infidelity. Consequently, the required 'goodness' of the data, and hence the goodness of the motion measurements on which the image is formed, depends strongly on whether autofocus is employed, and what capabilities the particular autofocus algorithm possesses.

5.1.4.1 No Autofocus

In the absence of any autofocus operations, the burden is solely on the navigation system to provide adequately accurate and precise motion measurements. That is, the range error $r_\varepsilon(t_n)$ needs to have negligible consequence on both the migration error term and the phase error term, particularly with respect to focusing the SAR image. To facilitate the following discussion we define several components to the range error, namely

$$\begin{aligned}
&\bar{r}_\varepsilon \approx r_e(t_0) = \text{a representative constant component in } r_\varepsilon(t_n),\\
&\dot{r}_e \approx \frac{d}{dt} r_e(t_0) = \text{the linear range error rate over the synthetic aperture,}\\
&\ddot{r}_e \approx \frac{d^2}{dt^2} r_e(t_0) = \text{the quadratic range error factor over the synthetic aperture,}\\
&\dddot{r}_e \approx \frac{d^3}{dt^3} r_e(t_0) = \text{the cubic range error factor over the synthetic aperture,}\\
&r_\varepsilon^s = \text{a sinusoidal range error factor over the synthetic aperture, and}\\
&r_\varepsilon^r = \text{a random range error factor over the synthetic aperture.}
\end{aligned} \tag{177}$$

Some of these components are more troublesome than others.

Small Constant Range Error

Consider first a small constant range error, where

$$r_\varepsilon(t_n) = \bar{r}_\varepsilon . \tag{178}$$

This would seem to cause the matched filter output to be expressed as

$$x_o \approx T\sum_n \mathrm{sinc}\left(\frac{\bar{r}_\varepsilon}{\rho_r}\right)\exp\left(j\frac{4\pi}{\lambda}\bar{r}_\varepsilon\right). \tag{179}$$

This is an expression for the effects of a range error on the exact pixel corresponding to 'truth'. In general, small 'constant' range errors are reasonably well tolerated. They will generally just shift the SAR image in range by a small amount, which may even be several pixels. To be sure, the constant range error will result in target location error in the range dimension. The range location error will be

$$s_{r,\varepsilon} = \bar{r}_\varepsilon\,. \tag{180}$$

The matched filter output at the displaced range can then be described as

$$x_o \approx T\sum_n \mathrm{sinc}\left(\frac{r_\varepsilon(t_n) - s_{r,\varepsilon}}{\rho_r}\right)\exp\left(j\frac{4\pi}{\lambda}\left(r_\varepsilon(t_n) - s_{r,\varepsilon}\right)\right). \tag{181}$$

This is expanded to

$$x_o \approx T\exp\left(-j\frac{4\pi}{\lambda}s_{r,\varepsilon}\right)\sum_n \mathrm{sinc}\left(\frac{r_\varepsilon(t_n) - s_{r,\varepsilon}}{\rho_r}\right)\exp\left(j\frac{4\pi}{\lambda}r_\varepsilon(t_n)\right). \tag{182}$$

Note that the consequence of a constant component in the range error is to shift the range at which the IPR peaks, and provide a constant phase error, otherwise the shape of the IPR magnitude remains unchanged. That is, the constant component of the range error has no effect on focusing of the SAR image.

Small Linear Range Error

Consider first a small linear range error, where

$$r_\varepsilon(t_n) = \dot{r}_e t_n\,. \tag{183}$$

This would seem to cause the matched filter output at the 'truth' location to be expressed as

$$x_o \approx T\sum_n \mathrm{sinc}\left(\frac{\dot{r}_e t_n}{\rho_r}\right)\exp\left(j\frac{4\pi}{\lambda}\dot{r}_e t_n\right). \tag{184}$$

Neglecting the migration term for the moment, a linear range variation over the synthetic aperture will cause an azimuthal target location shift of

$$s_{a,\varepsilon} = \frac{r_s(t_0)}{L_a \sin\phi_s}\dot{r}_e T_a = \frac{(\rho_a / a_w)}{(\lambda/2)}\dot{r}_e T_a\,. \tag{185}$$

The matched filter output at the displaced azimuth location can then be described as

$$x_o \approx T\sum_n \text{sinc}\left(\frac{r_\varepsilon(t_n)-\dfrac{(\lambda/2)s_{a,\varepsilon}}{(\rho_a/a_w)T_a}t_n}{\rho_r}\right)\exp\left(j\frac{4\pi}{\lambda}\left(r_\varepsilon(t_n)-\frac{(\lambda/2)s_{a,\varepsilon}}{(\rho_a/a_w)T_a}t_n\right)\right). \quad (186)$$

Note that the consequence of a linear component in the range error is to shift the azimuth location at which the IPR peaks, otherwise the shape of the IPR magnitude remains unchanged. That is, the linear component of the range error has no effect on focusing of the SAR image.

Additionally, the range migration at the displaced azimuth location is also zero, that is, the argument of the sinc() function goes to zero when $r_\varepsilon(t_n)=\dot{r}_e t_n$. Effectively, the entire synthetic aperture is pointed to a different azimuth location, but focusing in unimpaired. A constrained linear range error, perhaps due to aiding, is discussed in Appendix E.

Nonlinear Range Errors

While constant and linear range errors might displace the IPR, they do not significantly alter its shape. However, higher order range errors will degrade the shape of the IPR, via both the migration term and the phase term. Consequently, we identify the nonconstant, nonlinear phase error terms as

$$\text{detrend}\left(r_\varepsilon(t_n)\right)=r_\varepsilon(t_n)-\dot{r}_e t_n-\overline{r}_\varepsilon. \quad (187)$$

We define specific nonlinear components of the phase error as

$$\begin{aligned}
r_\varepsilon^q &= \frac{\ddot{r}_e}{2}\left(\frac{T_a}{2}\right)^2 \text{ = the peak quadratic range error over the synthetic aperture,}\\
r_\varepsilon^c &= \frac{\dddot{r}_e}{6}\left(\frac{T_a}{2}\right)^3 \text{ = the peak cubic range error over the synthetic aperture,}\\
r_\varepsilon^s &\text{ = the peak sinusoidal range error over the synthetic aperture, and}\\
r_\varepsilon^r &\text{ = the standard deviation of the random range error over the synthetic aperture.}
\end{aligned} \quad (188)$$

We now examine limitations on these nonlinear terms.

Migration Error

The essential behavior of the migration term that causes SAR image degradation is contained in the deviation due to nonlinear range error. For the migration term, the requirement for a high-fidelity SAR image is then

$$\operatorname{sinc}\left(\frac{\operatorname{detrend}\left(r_\varepsilon\left(t_n\right)\right)}{\rho_r}\right)\approx 1. \tag{189}$$

We may transmogrify the requirement to

$$\max\left(\operatorname{detrend}\left(r_\varepsilon\left(t_n\right)\right)\right)-\min\left(\operatorname{detrend}\left(r_\varepsilon\left(t_n\right)\right)\right)<\rho_r\,. \tag{190}$$

Stated simply, the residual range migration needs to be less than the range resolution over the entire synthetic aperture.

Phase Error

In general, phase error corresponds to range error via

$$\phi_\varepsilon\left(t_n\right)=\left(\frac{4\pi}{\lambda}\right)r_e\left(t_n\right). \tag{191}$$

Nonlinear range errors correspond to nonlinear phase errors. The effects of nonlinear phase errors have been addressed in the literature. See Appendix D for details of these phase error effects.

Corresponding peak phase errors to their range error counterparts are

$$\begin{aligned}
&\phi_\varepsilon^q=\left(4\pi/\lambda\right)r_\varepsilon^q \text{ = the peak quadratic phase error over the synthetic aperture,}\\
&\phi_\varepsilon^c=\left(4\pi/\lambda\right)r_\varepsilon^c \text{ = the peak cubic phase error over the synthetic aperture,}\\
&\phi_\varepsilon^s=\left(4\pi/\lambda\right)r_\varepsilon^s \text{ = the peak sinusoidal phase error over the synthetic aperture, and}\\
&\phi_\varepsilon^r=\left(4\pi/\lambda\right)r_\varepsilon^r \text{ = the standard deviation of the random phase error.}
\end{aligned} \tag{192}$$

While a ‘good’ IPR is somewhat subjective, the following criteria are typical for SAR,

Quadratic Phase Error less than 90 degrees (peak),

Cubic Phase Error less than 30 degrees (peak),

Sinusoidal Phase Error less than 1 degree (peak), and

Random phase error less than 1 degree standard deviation.

This implies range error components over the synthetic aperture at Ku-band as follows,

Quadratic Range Error less than 0.0023 m (peak),

Cubic Range Error less than 0.00075 m (peak),

Sinusoidal Range Error less than 0.000025 m (peak), and

Random Range Error less than 0.000025 m (1-sigma).

5.1.4.2 Conventional Autofocus

Autofocus is typically the blind deconvolution of phase errors from a SAR image. Algorithms to accomplish this are quite varied, with considerable differences in capabilities as well. A popular algorithm with generally good performance is the Phase Gradient Autofocus (PGA) algorithm.[32] As customarily implemented, PGA is able to correct a wide variety of phase error characteristics, limited only by the following constraints:

- Phase errors are confined to the range resolution, that is, no residual migration errors exist.
- Phase errors tend to be low frequency in nature, that is, the dominant effects exhibited are relatively near the IPR mainlobe.

Migration Error

Since PGA, and indeed most autofocus algorithms, operates only on range-compressed data, the constraints of the previous section still apply, namely

$$\max\left(\text{detrend}\left(r_\varepsilon\left(t_n\right)\right)\right) - \min\left(\text{detrend}\left(r_\varepsilon\left(t_n\right)\right)\right) < \rho_r \,. \tag{193}$$

Stated simply, the residual range migration needs to still be less than the range resolution.

Phase Error

PGA, as well as most other algorithms, mask the IPR in azimuth to some degree during the course of operation. This has the effect of limiting the corrective action of autofocus to phase errors that are highly correlated from one sample to the next, that is, errors with primarily low-frequency content, say some fraction of the entire scene being imaged.

Consequently, we can expect autofocus to correct quadratic, cubic, low-frequency sinusoidal, and low-frequency random phase errors. High-frequency sinusoidal phase errors, and high-frequency random phase errors, will generally not be adequately mitigated.

With autofocus, we retain the following typical criteria for SAR,

Sinusoidal Phase Error less than 1 degree (peak), and

Random phase error less than 1 degree standard deviation.

This implies range error components over the synthetic aperture at Ku-band as follows,

Sinusoidal Range Error less than 0.000025 m (peak), and

Random Range Error less than 0.000025 m (1-sigma).

5.1.4.3 *Autofocus with Subaperture Processing*

Subaperture processing typically divides the Doppler processing into coarse azimuth processing and fine azimuth processing.[33] Autofocus is typically only applied to fine azimuth processing, and then in a conventional manner.

Migration Error

Since conventional autofocus is still used in fine azimuth processing, and thereby only operates on range-compressed data, the constraints of the previous section still apply, namely

$$\max\left(\text{detrend}\left(r_\varepsilon\left(t_n\right)\right)\right) - \min\left(\text{detrend}\left(r_\varepsilon\left(t_n\right)\right)\right) < \rho_r \,. \tag{194}$$

Restated simply, the residual range migration needs to still be less than the range resolution.

Phase Error

The application of autofocus only during fine azimuth processing requires that phase errors be adequately low during the subaperture period without benefit of autofocus during the subaperture period.

We define

$$T_{subap} \text{ = the time period of a subaperture,} \tag{195}$$

and note that the subaperture period is usually a small fraction of the total aperture,

$$T_{subap} << T_a \,. \tag{196}$$

Consequently, peak phase errors are constrained during the subaperture period. Phase errors during a subaperture period are related to range error components by

$$\begin{aligned}
&\phi_\varepsilon^q = \left(2\pi/\lambda\right)\left(T_{subap}/2\right)^2 \ddot{r}_e \text{ = the peak quadratic phase error over the subaperture,} \\
&\phi_\varepsilon^c = \left(2\pi/3\lambda\right)\left(T_{subap}/2\right)^3 \dddot{r}_e \text{ = the peak cubic phase error over the subaperture,} \\
&\phi_\varepsilon^s = \left(4\pi/\lambda\right) r_\varepsilon^s \text{ = the peak sinusoidal phase error over the subaperture, and} \\
&\phi_\varepsilon^r = \left(4\pi/\lambda\right) r_\varepsilon^r \text{ = the standard deviation of the random phase error.}
\end{aligned} \tag{197}$$

Additionally, for subaperture image formation algorithms, fine resolution processing is meant to resolve coarse-resolution subimages, generally in azimuth. This implies that the IPR mask that a typical fine-resolution autofocus applies during its execution is smaller than in the case where subapertures are not used. This further implies that a smaller

bandwidth of phase errors is correctable when subapertures are employed. The disparity is generally greater as subaperture lengths increase.

Since subapertures generally overlap significantly, by say 60% or so, the ratio of correctable bandwidths for subaperture techniques versus non-subaperture techniques is about

$$2.5/(\text{subaperture\_length}). \tag{198}$$

For example, for a subaperture length of 64 samples, this corresponds to a reduction of correctable phase error bandwidth to about 4% of the non-subaperture capabilities. This, of course, assumes equal fractional IPR masks.

Of course, if the autofocus operation is applied prior to any subaperture processing, then the limits revert to that for conventional autofocus.

5.1.4.4 Migration Autofocus

At very fine range resolutions, the constraint on residual range migration error often becomes the limiting performance parameter. Consequently, an autofocus algorithm has been developed that corrects for some degree of residual range migration.[34,35] Kirk, et al.[36], describe a "Signal Based Motion Compensation" scheme to also correct radar imagery for excessive motion errors, beyond the mitigation ability of conventional autofocus.

An underlying assumption for this algorithm is that the migration error is a fairly smooth function with some limitations on its slope. This implies a presumption generally of predominantly low-frequency content of the range error.

After migration error correction, a more conventional autofocus operation can be applied, and typically is applied, with its attendant limitations.

The bottom line is that relatively low-frequency migration errors as well as relatively low-frequency phase errors can be corrected with this somewhat more exotic autofocus algorithm.

5.1.4.5 Inverse SAR Techniques

Inverse-SAR (ISAR) presumes a target's motion is unknown to the radar, although the nature of the target (e.g. maritime, land-based, etc.) can often be used to advantage to constrain the problem. Nevertheless, the target's unknown motion adds to the migration and phase errors of the target's echo data, and needs to be compensated to adequately image the target. Complicating this, the general orientation of the synthetic aperture for ISAR is even often unknown.[37,38]

In any case, this is very difficult compared to more conventional SAR, and although operational ISAR systems exist, especially for maritime applications, they virtually all suffer resolution and fidelity limitations compared to high-performance SAR systems.

5.2 Pointing Accuracy and Location Error

There are two issues with antenna pointing. The first is providing a proper and predictable illumination to the scene being imaged. The second is with direction of arrival measurements, such as with multi-phase center Interferometric SAR systems.

5.2.1 Antenna Beam Illumination

An antenna pattern will impart an intensity modulation of the SAR image. This is most noticeable in azimuth, usually because the azimuth beam pattern is often narrower than the elevation beam pattern, and small grazing angles elongate the antenna footprint in range. In the range dimension, echo energy exhibits a loss due to range variation in addition to the elevation antenna pattern. Although large range swaths may indeed exhibit effects of an elevation pointing error, most SAR systems will exhibit effects more likely, and more readily in the azimuth direction. We will confine the analysis in this section to the azimuth case.

Most high-performance SAR systems are designed to compensate the antenna beam pattern in azimuth (and range). Consequently, the intensity modulation as a function of azimuth location in the image is not apparent in a properly functioning SAR (i.e. with no pointing error).

However, if a pointing error exists, then the beam compensation that assumes correct pointing will in fact misapply its correction, thereby altering, but not eliminating the intensity modulation across the image.

Most antennas have a strong quadratic component in their beam pattern in the neighborhood of their mainlobe peak. Consider a simple model for an antenna beam mainlobe two-way field pattern as a quadratic of the form

$$y_{ideal}(x) = \max\left(1 - 2x^2, 0\right). \tag{199}$$

This is also the one-way beam power pattern. This antenna pattern obviously has nominal half-power one-way beamwidth of one. That is, $y(\pm 0.5) = 0.5$. The two-way power pattern would be $\left|y_{ideal}(x)\right|^2$.

Now suppose that there is an unknown pointing error x_ε. The actual antenna pattern is then

$$y_{actual}(x) = \max\left(1 - 2\left(x - x_\varepsilon\right)^2, 0\right). \tag{200}$$

We will henceforth assume that the SAR image is limited to the nonzero region of the antenna beam pattern.

Antenna beam pattern compensation assumes that we have the ideal pattern, and will compensate the illumination accordingly. Consequently, the net illumination in the SAR image is given by

$$y_{image}(x) = \frac{1-2(x-x_\varepsilon)^2}{1-2x^2}. \tag{201}$$

Notice that when the error is zero, the illumination in the image is constant, as desired. A series expansion of this yields

$$y_{image}(x) \approx \left(1-2x_\varepsilon{}^2\right) + 4x_\varepsilon x - 4x_\varepsilon{}^2 x^2 + 8x_\varepsilon x^3 - 84x_\varepsilon{}^2 x^4 + \ldots \tag{202}$$

From this we observe a strong linear component. This implies that the image itself, after the correction corresponding to an ideal pointing has been applied, will exhibit a strong linear illumination gradient increasing in the direction of the actual pointing, and that the gradient will be proportional to the pointing error. In spotlight SAR images this manifests as a superimposed intensity gradient across the SAR image. In a stripmap SAR image composed of contiguous spotlight images, this manifests as gradients in the individual patches with noticeable seams where the patches abut.

Equivalently, just because we don't see a peak in the illumination profile doesn't mean that the beam is centered outside the bounds of the image itself. That is, not appreciating the effects of antenna beam correction might lead us to conclude the error is bigger than it actually is.

For example, consider an error of ¼ beamwidth. The actual beam pattern and the ideal beam pattern are illustrated in Figure 10. Correcting the actual beam pattern with the ideal beam pattern yields the net magnitude illumination profile given in Figure 11.

Now suppose that our SAR image is constrained to only the middle 2/3 of the desired (ideal) antenna pattern, that is, between the vertical dotted lines. In this case we would see nearly a linear net illumination gradient across the image that varies by 9.8 dB from one edge to the other. This would be extremely noticeable and rather annoying in a mosaicked SAR stripmap composite image.

More generally, the image illumination variation can be plotted versus the antenna pointing error, and is done so in Figure 12. This plot shows that a 1/10 beamwidth error will yield a 3 dB illumination variation, and a 0.03 beamwidth error will yield a 0.9 dB illumination variation for the central 2/3 of the antenna beam.

Note that 0.03 beamwidths of a 3.2 degree beam corresponds to approximately 0.1 degrees of pointing error.

Anecdotal evidence suggests that a heading error of 1/30 of the antenna beamwidth is approximately the threshold for patches that occupy a large portion of the beamwidth.

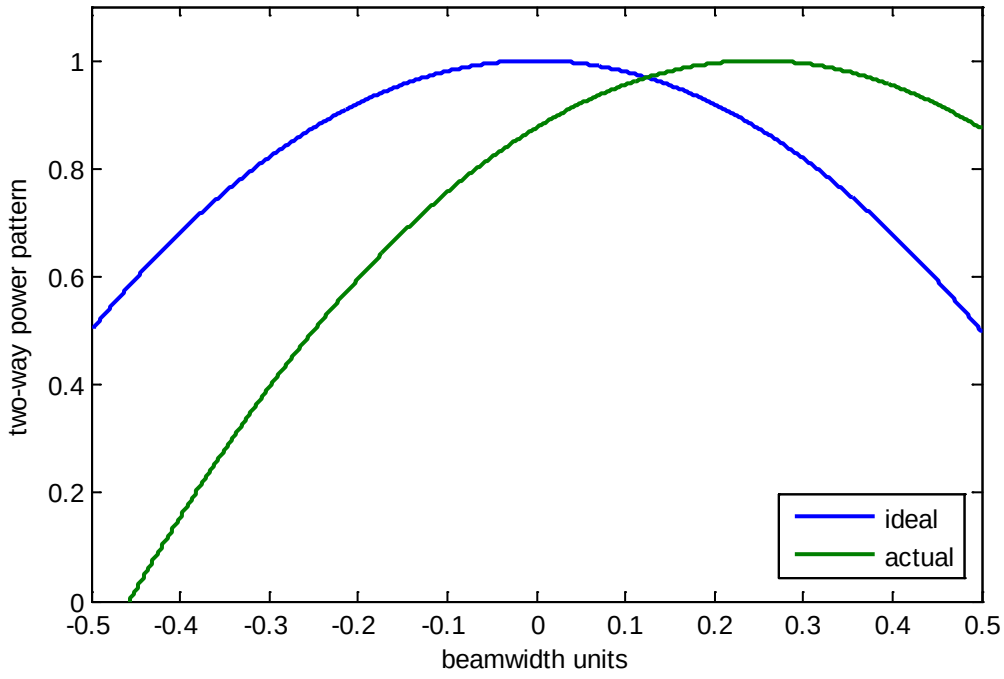

Figure 10. Example ideal (presumed) beam pattern and actual beam pattern with pointing error.

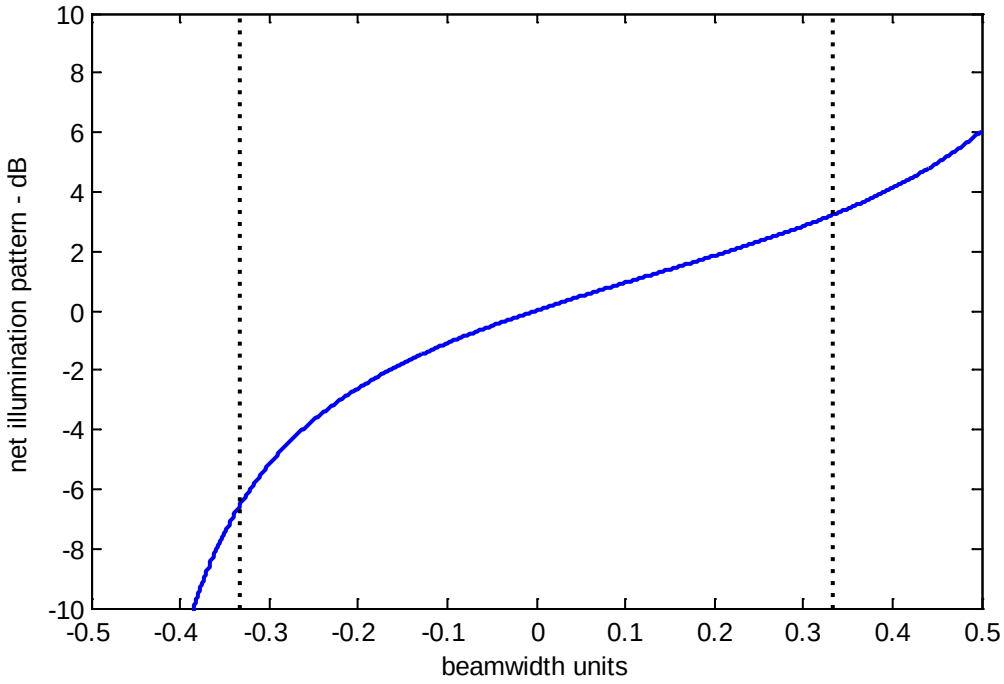

Figure 11. Illumination pattern in image for pointing error in Figure 10, normalized to the center of the image.

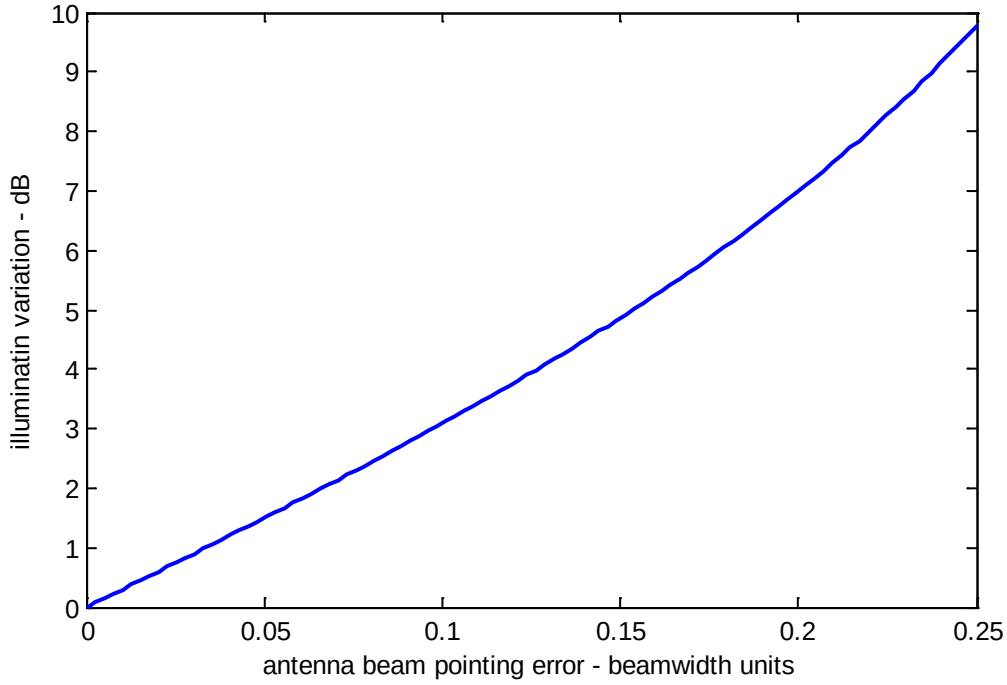

Figure 12. Illumination variation across central 2/3 of the beam pattern as a function of antenna pointing error.

This analysis has presumed that illumination correction applied was determined assuming no pointing error. A mitigation scheme for an unknown pointing error illumination might be to use data-driven techniques to measure the illumination function and correct for it as measured.[39,26,27]

5.2.2 Direction of Arrival Measurements

In some cases, SAR systems are required to provide Direction of Arrival (DOA) information based on interferometry measurements from multiple phase centers, or multiple antenna beams. Such systems include topographic mapping Interferometric SAR (IFSAR, or InSAR) systems, and clutter cancelling GMTI systems with algorithms that include Along-Track Interferometry (ATI), Displaced Phase Center Antenna (DPCA), and Space-Time Adaptive Processing (STAP).

Neglecting data-driven adaptive techniques, the fundamental goal is to steer a null towards a desired location. The ultimate location accuracy for the actual null placement is dependent on both the accuracy and precision with which the desired null direction is known, as well as the location accuracy of the radar position itself. For example, the right direction from the wrong spot will place the null in a wrong place. Nevertheless, we will hereafter assume that uncertainty in null steering is dominated by the accuracy of the direction information, that is, the ability to point the null in a specific direction. The null is steered via the antenna beam-steering mechanism, which depends on the fidelity of the radar antenna orientation information. Consequently, the null pointing accuracy is limited to the attitude knowledge accuracy of the motion measurement information.

We identify the azimuth-direction location error due to null steering as

$$s_{az,\varepsilon} = r_s(t_0)\theta_{az,\varepsilon}, \tag{203}$$

where

$$\theta_{az,\varepsilon} = \text{the azimuth-direction pointing accuracy.} \tag{204}$$

Likewise, we identify the elevation-direction location error due to null steering as

$$s_{el,\varepsilon} = r_s(t_0)\theta_{el,\varepsilon}, \tag{205}$$

where

$$\theta_{el,\varepsilon} = \text{the elevation-direction pointing accuracy.} \tag{206}$$

For example, if we require a worst-case 3 meter location accuracy at 10 km range, then pointing accuracy needs to be within 0.0172 degrees. This of course assumes perfect radar position information as well as perfect radar calibration.

As a final note we do not want to forget that the fields generated and received by the antenna will be affected by the antenna's environment. For example, any of the following will affect the accuracy of direction of arrival measurements.

- multipath and diffractive effects of structures in the vicinity of the radar,[40]
- refractive properties of radomes, including the radome shape,[41] and
- refractive properties of the atmosphere.[42,43]

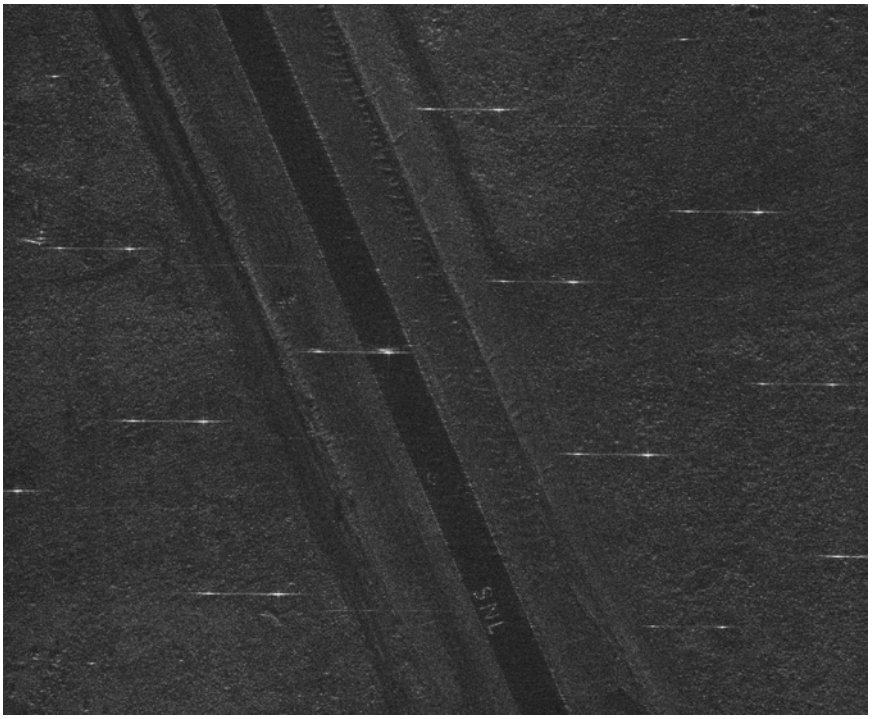

Figure 13. SAR image using conventional autofocus when range errors exceed the range resolution. Note the 'dumbbell' response of the corner reflectors.

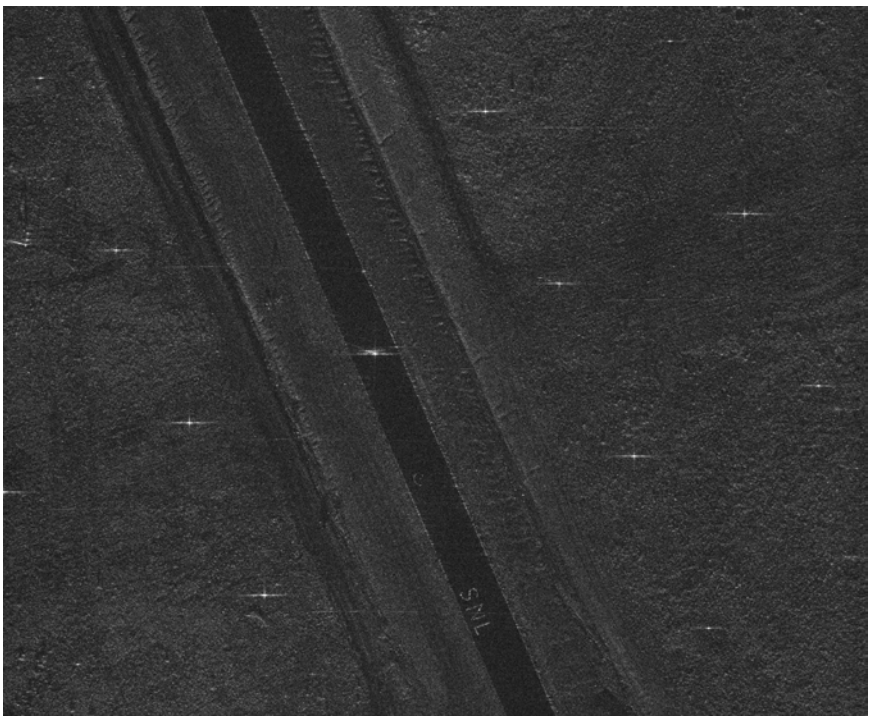

Figure 14. SAR image of Figure 13 when a migration correction autofocus was employed.

"Even though you are on the right track - you will get run over if you just sit there."
-- Will Rogers

6 So… How good does the IMU need to be?

In this section, we relate the navigator performance in Section 4 to the allowable radar position error in the previous section. This is a rather difficult task in that a number of options exist in both of these sections. Consequently we will make some assumptions to bound the problem. These include

1. We will assume that the IMU is un-aided during the synthetic aperture. To do otherwise requires knowledge of the aiding scheme and performance of the EKF. To avoid making this analysis implementation dependent, we make this somewhat pessimistic assumption.

2. We will assume that the IMU is perfectly aligned (without error) at the beginning of the synthetic aperture. This includes both position and orientation of the IMU. This is a somewhat optimistic assumption.

3. We will assume that navigator position corresponds directly to radar antenna phase center location. This neglects any influence of lever arms and any additional errors that might be encountered if this weren't so. We note that the location of an antenna's phase center is not always obvious, and generally also assumes a number of simplifications.[44]

4. We will assume that range errors are directly proportional to phase errors with known constant of proportionality. This implies that there are no atmospheric effects that would cause phase perturbations in addition to those of the mechanical motion itself.

5. We will assume that the range errors are dominated by nonlinear errors. We justify this by noting that the range errors are driven mainly by multiply integrated noise and biases.

6. We will assume that a Conventional Autofocus is used by the SAR. While better (more comprehensive) autofocus schemes exist, this level of performance is, as its descriptor implies, 'conventional'.

7. We will assume that the SAR antenna is a single phase center. Furthermore, pointing requirements are for illumination purposes only, and direction-of-arrival measurements with multiple antenna phase centers will not be made.

6.1 Navigator Position Error and Focus Limits

From the previous section we identified that a position error generates a range error, which in turn becomes a timing error that generates a phase error in addition to contributing excessive residual migration. The range error was calculated as

$$r_\varepsilon(t_n) \approx \mathbf{n}_s(t_n) \circ \mathbf{p}_\varepsilon(t_n) + \frac{|\mathbf{p}_\varepsilon(t_n)|^2}{2|\mathbf{r}_s(t_n)|}. \tag{207}$$

We will simplify this somewhat further and use only the line-of-sight component. That is, we will simplify this to

$$r_\varepsilon(t_n) \approx \mathbf{n}_s(t_n) \circ \mathbf{p}_\varepsilon(t_n). \tag{208}$$

From Section 4 we identified the *y*-axis position error model as

$$p_{y,\varepsilon}(t) = \begin{bmatrix} \int_0^t \int \left(\left| a_{y',t} \right| \mathrm{B}_{\max} + a_{y',\perp} \sin\left(\phi_m + \phi_n\right) + n_{y',a,0} + n_{y',a,1} + n_{y',a,2} \right) d\tau d\tau \\ + a_{z',t} \int_0^t \int \int \left(\begin{array}{l} \left| \omega_{x',t} \right| \Gamma_{\max} + \omega_{x',\perp} \sin\left(\varphi_m + \varphi_n\right) \\ + n_{x',\omega,0} + n_{x',\omega,1} + n_{x',\omega,2} \end{array} \right) d\tau d\tau d\tau \\ - a_{x',t} \int_0^t \int \int \left(\begin{array}{l} \left| \omega_{z',t} \right| \Gamma_{\max} + \omega_{z',\perp} \sin\left(\varphi_m + \varphi_n\right) \\ + n_{z',\omega,0} + n_{z',\omega,1} + n_{z',\omega,2} \end{array} \right) d\tau d\tau d\tau \end{bmatrix}. \tag{209}$$

If we align the *y*-axis with the line-of-sight vector to the target scene reference point, then we can approximate the range error at the end of a synthetic aperture, at time T_a, with

$$r_\varepsilon(T_a) = \begin{bmatrix} \int_0^{T_a} \int \left(\left| a_{y',t} \right| \mathrm{B}_{\max} + a_{y',\perp} \sin\left(\varphi_m + \varphi_n\right) + n_{y',a,0} + n_{y',a,1} + n_{y',a,2} \right) d\tau d\tau \\ + a_{z',t} \int_0^{T_a} \int \int \left(\begin{array}{l} \left| \omega_{x',t} \right| \Gamma_{\max} + \omega_{x',\perp} \sin\left(\phi_m + \phi_n\right) \\ + n_{x',\omega,0} + n_{x',\omega,1} + n_{x',\omega,2} \end{array} \right) d\tau d\tau d\tau \\ - a_{x',t} \int_0^{T_a} \int \int \left(\begin{array}{l} \left| \omega_{z',t} \right| \Gamma_{\max} + \omega_{z',\perp} \sin\left(\phi_m + \phi_n\right) \\ + n_{z',\omega,0} + n_{z',\omega,1} + n_{z',\omega,2} \end{array} \right) d\tau d\tau d\tau \end{bmatrix}. \tag{210}$$

Conventional autofocus requires that any residual uncompensated range migration be limited to less than the range resolution, namely such that

$$\max r_\varepsilon(t_n) - \min r_\varepsilon(t_n) < \rho_r \,. \tag{211}$$

In addition, sinusoidal phase errors need to be less than 1 degree (peak), and random phase errors need to be less than about 1 deg (RMS). The nature of the IMU errors suggests that instrument imperfections are more about drifting, alignments, and scale factors, which are then substantially low-pass filtered by the multiple integration stages.

Since our presumption is that we have perfect alignment at the beginning of the synthetic aperture, and errors grow from there, our motion measurement error requirement becomes

$$r_\varepsilon(T_a) < \rho_r \,. \tag{212}$$

There are two approaches available to us for relating IMU errors to the range error limit.

1. The first approach is to place a requirement on each and every component of the range error $r_\varepsilon(T_a)$. Such an approach might be to apply the maximum allowable error limit ρ_r to each and every component of $r_\varepsilon(T_a)$. That is, we will require each component of $r_\varepsilon(T_a)$ to be less than the range resolution ρ_r. While an apportioned error budget approach might seem more prudent, the question arises as to what the apportionment should be. It is likely that some IMU parameters will be more significant than others, and there is no guarantee that the order of significance won't change with time T_a.

2. The second approach is to begin with a particular IMU's parameter set, and calculate the bound on $r_\varepsilon(T_a)$. This is then compared to ρ_r to decide if the particular IMU is an acceptable candidate for the SAR system design.

Both approaches have merit. The first approach can be used to down-select the set of candidate IMUs, and the second approach can be used to perhaps down-select even further.

We will now examine the various components of $r_\varepsilon(T_a)$ in more detail, and calculate limits on them consistent with the first approach. To complete the geometry definitions for the following analysis, we will define the axes at the beginning of the synthetic aperture as follows

x'-axis = horizontal and orthogonal to the *y*'-axis

y'-axis = the line-of-sight direction to the target scene reference point

z'-axis = orthogonal to the *y*'-axis in a vertical plane

For a broadside SAR imaging system, the radar is traveling in the positive *x'* direction. This makes the *x'*-axis in this case the roll axis. Additionally, for shallow grazing angles, the *y'*-axis is nearly the pitch axis, and the *z'*-axis is nearly the yaw axis. A right-hand coordinate system is presumed.

6.1.1 Accelerometer Parameters

Here we are interested in the influence of accelerometer instrument parameters on the final range error. We define this particular collection of errors as

$$r_{\varepsilon,a}(T_a) = \left[\int_0^{T_a} \int \left(\left| a_{y',t} \right| \mathrm{B}_{\max} + a_{y',\perp} \sin(\varphi_m + \varphi_n) + n_{y',a,0} + n_{y',a,1} + n_{y',a,2} \right) d\tau d\tau \right]. \tag{213}$$

This can of course be expanded to

$$r_{\varepsilon,a}(T_a) = \left[\begin{array}{l} \int_0^{T_a} \int \left| a_{y',t} \right| \mathrm{B}_{\max} d\tau d\tau \\ + \int_0^{T_a} \int a_{y',\perp} \sin(\varphi_m + \varphi_n) d\tau d\tau \\ + \int_0^{T_a} \int n_{y',a,0} d\tau d\tau \\ + \int_0^{T_a} \int n_{y',a,1} d\tau d\tau \\ + \int_0^{T_a} \int n_{y',a,2} d\tau d\tau \end{array} \right]. \tag{214}$$

The individual terms in the square brackets are now examined in turn.

6.1.1.1 Scale Factor Errors

We define the component due to scale factor errors as

$$r_{\varepsilon,a1}(T_a) = \int_0^{T_a} \int \left| a_{y',t} \right| \mathrm{B}_{\max} d\tau d\tau \,. \tag{215}$$

This is evaluated as

$$r_{\varepsilon,a1}(T_a) = \left|a_{y',t}\right| \mathrm{B}_{\max} \frac{{T_a}^2}{2}. \tag{216}$$

Recall that the acceleration is presumed to be a constant, and dominated by gravity. While SAR does not normally operate looking straight down, so that $\left|a_{y',t}\right|$ is not identically equal to gravity, SAR may nevertheless look at some pretty steep depression angles. For example, at a 60 degree depression angle, the line of sight acceleration component due to gravity will be about 0.87*g*. This is close enough to 1 *g* that we allow the approximation

$$r_{\varepsilon,a1}(T_a) \approx g\ \mathrm{B}_{\max} \frac{{T_a}^2}{2}. \tag{217}$$

Consequently, the requirement on scale factor error becomes

$$\mathrm{B}_{\max} < 0.2 \frac{\rho_r}{{T_a}^2}. \tag{218}$$

This value would need to be multiplied by 10^6 if reported in PPM. In addition, for most long-range SAR systems, depression angles will be relatively shallow, meaning that gravity will couple less to the line-of-sight direction in these cases. This suggests that for long-range airborne systems we are likely to tolerate a scale factor error somewhat larger than the limit calculated above, say by an order of magnitude when depression angles are in the single-digit degrees.

Finally, we note that the scale factor error, and the performance limits SAR requires, are over the range of accelerations that are expected for the radar. IMUs are often specified over many *g* of operating range. It is not clear that the data sheet scale factors apply to the relatively benign accelerations expected for most SAR systems.

6.1.1.2 *Misalignment and Nonorthogonality Errors*

We define the range error component due to misalignment and nonorthogonality errors as

$$r_{\varepsilon,a2}(T_a) = \int_0^{T_a} \int a_{y',\perp} \sin(\varphi_m + \varphi_n) d\tau d\tau. \tag{219}$$

Since misalignment and nonorthogonality errors are constant, and we have presumed $a_{y',\perp}$ constant as well, the double integral evaluates to

$$r_{\varepsilon,a2}(T_a) = a_{y',\perp} \sin(\varphi_m + \varphi_n) \frac{{T_a}^2}{2}. \tag{220}$$

At shallow grazing angles, the acceleration component is approximately gravity, namely,

$$a_{y',\perp} \approx g \,. \tag{221}$$

Consequently,

$$r_{\varepsilon,a2}(T_a) \approx g \sin(\varphi_m + \varphi_n) \frac{{T_a}^2}{2} \,. \tag{222}$$

The requirement for the misalignment and nonorthogonality errors becomes

$$\sin(\varphi_m + \varphi_n) < 0.2 \frac{\rho_r}{{T_a}^2} \,. \tag{223}$$

6.1.1.3 White Noise Errors (Velocity Random Walk)

We define the range error component due to bias white noise as

$$r_{\varepsilon,a3}(T_a) = \int_0^{T_a} \int n_{y',a,0} \, d\tau \, d\tau \,. \tag{224}$$

Recall that $n_{y',a,0}$ is a random process with Power Spectral Density given by

$$S_N(f) = N^2 \quad (\mu g)^2 / Hz \;. \tag{225}$$

Accounting for unit conversions (μg to m/s^2), the expected variance after a double integration from Appendix B is

$$\sigma_{a3}^2 \approx \left(9.8 \times 10^{-6}\right)^2 N^2 \left(\frac{{T_a}^3}{3} \right). \tag{226}$$

This is a statistical measure that indicates the probability of the range error component falling within some value. We choose the seemingly reasonable criteria that two standard deviations should fall within the range error limit. Consequently

$$2\sigma_{a3} < \rho_r \,. \tag{227}$$

This implies the constraint

$$N < 8.8 \times 10^4 \frac{\rho_r}{{T_a}^{3/2}} \quad \mu g / \sqrt{Hz} \,. \tag{228}$$

6.1.1.4 Bias Instability Errors

We define the component due to bias instability as

$$r_{\varepsilon,a4}(T_a) = \int_0^{T_a} \int n_{y',a,1} d\tau d\tau \,. \tag{229}$$

Recall that $n_{y',a,1}$ is a random process with Power Spectral Density given by

$$S_B(f) = \frac{B^2}{2\pi|f|} \quad (\mu g)^2/Hz \,. \tag{230}$$

Accounting for unit conversions (μg to m/s^2), the expected variance after a double integration from Appendix C is

$$\sigma_{a4}^2 \approx \left(9.8\times10^{-6}\right)^2 \left(\frac{B^2}{2}\right) \frac{{T_a}^4}{4} \,. \tag{231}$$

As before we choose the seemingly reasonable criteria that two standard deviations should fall within the range error limit. Consequently

$$2\sigma_{a4} < \rho_r \,. \tag{232}$$

This implies the constraint

$$B < 1.4\times10^5 \frac{\rho_r}{{T_a}^2} \quad \mu g \,. \tag{233}$$

6.1.1.5 Acceleration Random Walk Errors

We define the component due to bias random walk as

$$r_{\varepsilon,a5}(T_a) = \int_0^{T_a} \int n_{y',a,2} d\tau d\tau \,. \tag{234}$$

Recall that $n_{y',a,2}$ is a random process with Power Spectral Density given by

$$S_K(f) = \frac{K^2}{(2\pi f)^2} \quad (\mu g)^2/Hz \,. \tag{235}$$

However, this error can itself be modeled as an integration of white noise with Power Spectral Density of K^2. Consequently, $r_{\varepsilon,a5}(T_a)$ is in fact a triple integration of white noise.

Accounting for unit conversions (μg to m/s^2), the expected variance after a triple integration of the white noise from Appendix B is

$$\sigma_{a5}^2 \approx \left(9.8\times10^{-6}\right)^2 K^2 \left(\frac{{T_a}^5}{20}\right). \tag{236}$$

As before we choose the seemingly reasonable criteria that two standard deviations should fall within the range error limit. Consequently

$$2\sigma_{a5} < \rho_r \,. \tag{237}$$

This implies the constraint

$$K < 2.3\times10^5 \frac{\rho_r}{{T_a}^{5/2}} \quad \mu g/\sqrt{s} \,. \tag{238}$$

6.1.2 Rate Gyro Parameters

Here we are interested in the influence of rate gyro instrument parameters on the final range error. We define this particular collection of errors as

$$r_{\varepsilon,\omega}(T_a) = \begin{bmatrix} a_{z',t} \int_0^{T_a}\int\int\left(\begin{matrix}\left|\omega_{x',t}\right|\Gamma_{\max} + \omega_{x',\perp}\sin(\phi_m+\phi_n)\\ + n_{x',\omega,0} + n_{x',\omega,1} + n_{x',\omega,2}\end{matrix}\right)d\tau d\tau d\tau \\ - a_{x',t} \int_0^{T_a}\int\int\left(\begin{matrix}\left|\omega_{z',t}\right|\Gamma_{\max} + \omega_{z',\perp}\sin(\phi_m+\phi_n)\\ + n_{z',\omega,0} + n_{z',\omega,1} + n_{z',\omega,2}\end{matrix}\right)d\tau d\tau d\tau \end{bmatrix}. \tag{239}$$

Consistent with earlier assumptions, we shall assume that gravity is the dominant acceleration, and we may simplify with

$$\begin{aligned} &a_{z',t} \approx g \text{ , and} \\ &a_{x',t} \approx 0 \,. \end{aligned} \tag{240}$$

This allows us to expand this range error component to

$$r_{\varepsilon,\omega}(T_a) = \begin{bmatrix} g\int_0^{T_a}\int\int\left|\omega_{x',t}\right|\Gamma_{\max}d\tau d\tau d\tau \\ +g\int_0^{T_a}\int\int\omega_{x',\perp}\sin(\phi_m+\phi_n)d\tau d\tau d\tau \\ +g\int_0^{T_a}\int\int n_{x',\omega,0}d\tau d\tau d\tau \\ +g\int_0^{T_a}\int\int n_{x',\omega,1}d\tau d\tau d\tau \\ +g\int_0^{T_a}\int\int n_{x',\omega,2}d\tau d\tau d\tau \end{bmatrix}. \quad (241)$$

The individual terms in the square brackets are now examined in turn.

6.1.2.1 Scale Factor Errors

We define the component due to scale factor errors as

$$r_{\varepsilon,\omega 1}(T_a) = g\int_0^{T_a}\int\int\left|\omega_{x',t}\right|\Gamma_{\max}d\tau d\tau d\tau . \quad (242)$$

If $\omega_{x',t}$ were a constant, then this would be evaluated as

$$r_{\varepsilon,\omega 1}(T_a) = g\left|\omega_{x',t}\right|\Gamma_{\max}\frac{T_a^3}{6}, \quad (243)$$

and the requirement on scale factor error would become

$$\Gamma_{\max} < \frac{6\rho_r}{g\left|\omega_{x',t}\right|T_a^3}. \quad (244)$$

However, it seems unreasonable to believe that $\omega_{x',t}$ is a constant over the course of the synthetic aperture. If we assume as in the examples of Section 3 that a roll and recovery is executed at the beginning of the synthetic aperture, then this implies that

$$\int_{0}^{0+} \left| \omega_{x',t} \right| dt \approx 2\Delta\theta_{d,x}, \tag{245}$$

where

$\Delta\theta_{d,x}$ = the accumulated angular roll displacement in one direction in radians. (246)

Consequently, we can calculate a bound on the accumulated range error as

$$r_{\varepsilon,\omega 1}(T_a) = g\Gamma_{\max}\Delta\theta_{d,x}T_a{}^2. \tag{247}$$

Clearly, the influence of angular rate scale factors depends heavily on the nature of the angular velocity measured. The more that the aircraft rolls back and forth during the synthetic aperture, the greater the contribution of scale factor errors. It is expected that even benign flight conditions will exhibit some angular displacements. The question becomes "What is reasonable to presume?" To move the analysis forward, we will make the presumption of a single roll and recovery of one radian each at the beginning of the synthetic aperture. This allows

$$\Delta\theta_{d,x} \approx 1 \quad \text{radian.} \tag{248}$$

Consequently,

$$r_{\varepsilon,\omega 1}(T_a) = g\Gamma_{\max}T_a{}^2. \tag{249}$$

Consequently, the requirement on scale factor error becomes

$$\Gamma_{\max} < 0.1\frac{\rho_r}{T_a{}^2}. \tag{250}$$

This value would need to be multiplied by 10^6 if reported in PPM.

Note that for a benign flight path with minimal roll motion, this limit might be easily be argued as very squishy.

6.1.2.2 *Misalignment and Nonorthogonality Errors*

We define the range error component due to misalignment and nonorthogonality errors as

$$r_{\varepsilon,\omega 2}(T_a) = g\int_{0}^{T_a}\int\int \omega_{x',\perp}\sin(\phi_m + \phi_n)d\tau d\tau d\tau. \tag{251}$$

As with acceleration, we shall assume misalignment and nonorthogonality errors are constant.

Note that for a broadside SAR geometry, $\omega_{x',\perp}$ is some combination of pitch angle and yaw angle. While we would expect pitch angle accumulations to be rather small, we can certainly reasonably envision a yaw angle change during the synthetic aperture, as when a heading change is undertaken.

If we assume as in the examples of Section 3 that a heading change is executed at the beginning of the synthetic aperture, then this implies that

$$\int_0^{0+} \omega_{x',\perp} dt \approx \Delta\theta_{d,x,\perp}, \tag{252}$$

where

$$\Delta\theta_{d,x,\perp} \approx \text{ the accumulated heading displacement in radians.} \tag{253}$$

Consequently, the range error becomes

$$r_{\varepsilon,\omega 2}(T_a) = g \sin(\phi_m + \phi_n)\Delta\theta_{d,x,\perp} \frac{{T_a}^2}{2}. \tag{254}$$

As before, we will assume that the heading change is limited to 1 radian. The requirement for the misalignment and nonorthogonality errors becomes

$$\sin(\phi_m + \phi_n) < 0.2 \frac{\rho_r}{{T_a}^2}. \tag{255}$$

6.1.2.3 White Noise Errors (Angle Random Walk)

We define the range error component due to bias white noise as

$$r_{\varepsilon,\omega 3}(T_a) = g \int_0^{T_a} \int\int n_{x',\omega,0} d\tau d\tau d\tau. \tag{256}$$

Recall that $n_{y',\omega,0}$ is a random process with Power Spectral Density given by

$$S_N(f) = 3600N^2 \quad (^\circ/h)^2/Hz \ . \tag{257}$$

Recall that N has units $^\circ/\sqrt{h}$. Accounting for unit conversions ($^\circ/h$ to rad/s), the expected variance after a triple integration from Appendix B is

$$\sigma_{\omega 3}^2 \approx \left(4.85\times10^{-6}\right)^2 (9.8)^2 3600 N^2 \left(\frac{T_a{}^5}{20}\right). \tag{258}$$

This is a statistical measure that indicates the probability of the range error component falling within some value. As with acceleration, we choose the seemingly reasonable criteria that two standard deviations should fall within the range error limit. Consequently

$$2\sigma_{\omega 3} < \rho_r . \tag{259}$$

This implies the constraint

$$N < 784 \frac{\rho_r}{T_a{}^{5/2}} \quad {}^\circ/\sqrt{h} . \tag{260}$$

6.1.2.4 Bias Instability Errors

We define the component due to bias instability as

$$r_{\varepsilon,\omega 4}(T_a) = g \int_0^{T_a} \int\int n_{x',\omega,1} d\tau d\tau d\tau . \tag{261}$$

Recall that $n_{y',\omega,1}$ is a random process with Power Spectral Density given by

$$S_B(f) = \frac{B^2}{2\pi|f|} \quad ({}^\circ/h)^2/Hz . \tag{262}$$

Recall that B has units ${}^\circ/h$. Accounting for unit conversions (${}^\circ/h$ to rad/s), the expected variance after a triple integration from Appendix C is

$$\sigma_{\omega 4}^2 \approx \left(4.85\times10^{-6}\right)^2 (9.8)^2 \left(\frac{B^2}{2}\right) \frac{T_a{}^6}{36} . \tag{263}$$

As before we choose the seemingly reasonable criteria that two standard deviations should fall within the range error limit. Consequently

$$2\sigma_{\omega 4} < \rho_r . \tag{264}$$

This implies the constraint

$$B < 8.93\times10^{4}\frac{\rho_r}{T_a{}^3}\quad {}^\circ/h\,. \tag{265}$$

6.1.2.5 Rate Random Walk Errors

We define the component due to bias random walk as

$$r_{\varepsilon,\omega5}(T_a) = g\int_0^{T_a}\int\int n_{x',\omega,2}\,d\tau\,d\tau\,d\tau\,. \tag{266}$$

Recall that $n_{y',\omega,2}$ is a random process with Power Spectral Density given by

$$S_K(f) = \frac{K^2}{3600(2\pi f)^2}\quad (^\circ/h)^2/Hz\,. \tag{267}$$

However, this error can itself be modeled as an integration of white noise with Power Spectral Density of $K^2/3600$. Consequently, $r_{\varepsilon,\omega5}(T_a)$ is in fact a fourth-order integration of white noise.

Accounting for unit conversions ($^\circ/h$ to rad/s), the expected variance after a fourth-order integration of the white noise from Appendix B is

$$\sigma_{\omega5}^2 \approx \left(4.85\times10^{-6}\right)^2(9.8)^2\frac{K^2}{3600}\left(\frac{T_a{}^7}{252}\right). \tag{268}$$

As before we choose the seemingly reasonable criteria that two standard deviations should fall within the range error limit. Consequently

$$2\sigma_{\omega5} < \rho_r\,. \tag{269}$$

This implies the constraint

$$K < 10^{7}\frac{\rho_r}{T_a{}^{7/2}}\quad {}^\circ/h^{3/2}\,. \tag{270}$$

6.2 Navigator Orientation Error and Pointing Limits

From Section 4 we recall that the angular displacement (orientation) error around the *z'* axis over a synthetic aperture is modeled as

$$\Delta\theta_{z',\varepsilon}(T_a) = \int_0^{T_a} \left(\left| \omega_{z',t} \right| \Gamma_{\max} + \omega_{z',\perp} \sin(\phi_m + \phi_n) + n_{z',\omega,0} + n_{z',\omega,1} + n_{z',\omega,2} \right) d\tau \, . \tag{271}$$

This orientation error will cause an illumination error in the scene being imaged, as shown in Section 5. We desire this orientation error to be some small fraction of the antenna beamwidth, say

$$\Delta\theta_{z',\varepsilon}(T_a) \le \beta \Theta_{z'} \, , \tag{272}$$

where

$\Theta_{z'}$ = the antenna beamwidth normal to the *z'* axis, and
β = the fraction of the antenna beamwidth for the allowed error. (273)

A reasonable number for β might be 0.03 for a 1 dB variation after correction for the central 2/3 of the antenna beam, as shown in Section 5.

The orientation error can be expanded to individual integrals as

$$\Delta\theta_{z',\varepsilon}(T_a) = \begin{bmatrix} \int_0^{T_a} \left| \omega_{z',t} \right| \Gamma_{\max} d\tau \\ + \int_0^{T_a} \omega_{z',\perp} \sin(\phi_m + \phi_n) d\tau \\ + \int_0^{T_a} n_{z',\omega,0} d\tau \\ + \int_0^{T_a} n_{z',\omega,1} d\tau \\ + \int_0^{T_a} n_{z',\omega,2} d\tau \end{bmatrix} . \tag{274}$$

As with position error, we will apply the criteria for $\Delta\theta_{z',\varepsilon}(T_a)$ to each of these components.

6.2.1 Scale Factor Errors

We apply the angular error limit to scale factor errors as

$$\int_0^{T_a} \left|\omega_{z',t}\right| \Gamma_{\max} d\tau < \beta \Theta_{z'} . \tag{275}$$

At shallow grazing angles, angular displacement around the z' axis is equivalent to a heading change, which is plausible during a synthetic aperture. Consequently we identify

$$\int_0^{T_a} \left|\omega_{z',t}\right| d\tau \approx \Delta\theta_{d,z'} \text{ = angular displacement.} \tag{276}$$

This allows us to calculate

$$\Gamma_{\max} \Delta\theta_{d,z'} < \beta \Theta_{z'} . \tag{277}$$

This can be manipulated to

$$\Gamma_{\max} < \frac{\beta \Theta_{z'}}{\Delta\theta_{d,z'}} . \tag{278}$$

As previously discussed for position error, we will make the presumption of a heading change of one radian during the synthetic aperture. This allows

$$\Gamma_{\max} < \beta \Theta_{z'} . \tag{279}$$

This also means that $\Theta_{z'}$ is reported in radians. This value would also need to be multiplied by 10^6 if reported in PPM.

Note that for a benign flight path with minimal heading changes, this limit might be easily be argued as very squishy.

In any case, this is expected to typically a much sloppier limit than that developed for position error concerns.

6.2.2 Misalignment and Nonorthogonality Errors

We apply the angular error limit to misalignment and nonorthogonality errors as

$$\int_0^{T_a} \omega_{z',\perp} \sin(\phi_m + \phi_n) d\tau < \beta \Theta_{z'} . \tag{280}$$

For shallow grazing angles, $\omega_{z',\perp}$ corresponds primarily to roll and pitch motions. Both of these tend to be maintained as constant during a synthetic aperture, that is, angular departures tend to be corrected by the aircraft controller. As a consequence, we expect this component to be negligible.

6.2.3 White Noise Errors (Angle Random Walk)

We apply the angular error limit to the white noise term as

$$\int_0^{T_a} n_{z',\omega,0} d\tau < \beta \Theta_{z'} . \tag{281}$$

Recall that $n_{y',\omega,0}$ is a random process with Power Spectral Density given by

$$S_N(f) = 3600 N^2 \quad (^\circ/h)^2 / Hz \ . \tag{282}$$

Recall that N has units $^\circ/\sqrt{h}$. Accounting for unit conversions ($^\circ/h$ to rad/s), the expected variance after integration from Appendix B is

$$\sigma_{\theta 3}^2 \approx \left(4.85 \times 10^{-6}\right)^2 3600 N^2 T_a . \tag{283}$$

This is a statistical measure that indicates the probability of the angular error component falling within some value. As with previous analysis, we choose the seemingly reasonable criteria that two standard deviations should fall within the error limit. Consequently

$$2\sigma_{\theta 3} < \beta \Theta_{z'} . \tag{284}$$

This implies the constraint

$$N < 1718 \frac{\beta \Theta_{z'}}{\sqrt{T_a}} \quad ^\circ/\sqrt{h} . \tag{285}$$

Note that $\Theta_{z'}$ is reported in radians.

6.2.4 Bias Instability Errors

We apply the angular error limit to the bias instability term as

$$\int_0^{T_a} n_{z',\omega,1} d\tau < \beta \Theta_{z'}. \tag{286}$$

Recall that $n_{y',\omega,1}$ is a random process with Power Spectral Density given by

$$S_B(f) = \frac{B^2}{2\pi|f|} \quad (^\circ/h)^2/Hz. \tag{287}$$

Recall that B has units $^\circ/h$. Accounting for unit conversions ($^\circ/h$ to rad/s), the expected variance after an integration from Appendix C is

$$\sigma_{\theta 4}^2 \approx \left(4.85\times10^{-6}\right)^2 \left(\frac{B^2}{2}\right) {T_a}^2. \tag{288}$$

As before we choose the seemingly reasonable criteria that two standard deviations should fall within the range error limit. Consequently

$$2\sigma_{\theta 4} < \beta \Theta_{z'}. \tag{289}$$

This implies the constraint

$$B < 1.46\times10^5 \frac{\beta \Theta_{z'}}{T_a} \quad ^\circ/h. \tag{290}$$

Note that $\Theta_{z'}$ is reported in radians.

6.2.5 Rate Random Walk Errors

We apply the angular error limit to the bias instability term as

$$\int_0^{T_a} n_{x',\omega,2} d\tau < \beta \Theta_{z'}. \tag{291}$$

Recall that $n_{y',\omega,2}$ is a random process with Power Spectral Density given by

$$S_K(f) = \frac{K^2}{3600(2\pi f)^2} \quad (^\circ/h)^2/Hz. \tag{292}$$

However, as with position error analysis, this bias instability error can itself be modeled as an integration of white noise with Power Spectral Density of $K^2/3600$. Consequently, the integration of bias instability noise is in fact a double integration of white noise.

Accounting for unit conversions ($^\circ/h$ to rad/s), the expected variance after a double integration of the white noise from Appendix B is

$$\sigma_{\theta 5}^2 \approx \left(4.85\times 10^{-6}\right)^2 \frac{K^2}{3600}\left(\frac{{T_a}^3}{3}\right). \tag{293}$$

As before we choose the seemingly reasonable criteria that two standard deviations should fall within the range error limit. Consequently

$$2\sigma_{\theta 5} < \beta\Theta_{z'}. \tag{294}$$

This implies the constraint

$$K < 1.07\times 10^7 \frac{\beta\Theta_{z'}}{{T_a}^{3/2}} \quad ^\circ/h^{3/2}. \tag{295}$$

Note that $\Theta_{z'}$ is reported in radians.

6.3 Summary of Instrument Parameter Limits

We summarize the results of the previous two sections in the following tables.

Table 2. Summary of accelerometer parameter limits affecting position error.

Parameter	***Criteria***	***Units***
Scale Factor Errors	$\mathrm{B}_{\max} < 2\times 10^5\, \rho_r / {T_a}^2$	PPM
Misalignment and Nonorthogonality	$\sin(\varphi_m + \varphi_n) < 0.2\, \rho_r / {T_a}^2$	
Acceleration White Noise (VRW)	$N < 8.8\times 10^4\, \rho_r / {T_a}^{3/2}$	$\mu g/\sqrt{Hz}$
Acceleration Bias Instability	$B < 1.4\times 10^5\, \rho_r / {T_a}^2$	μg
Acceleration Random Walk	$K < 2.3\times 10^5\, \rho_r / {T_a}^{5/2}$	$\mu g/\sqrt{s}$

Table 3. Summary of rate gyro parameter limits affecting position error.

Parameter	***Criteria***	***Units***
Scale Factor Errors	$\Gamma_{\max} < 10^5 \rho_r / T_a{}^2$	PPM
Misalignment and Nonorthogonality	$\sin(\phi_m + \phi_n) < 0.2 \rho_r / T_a{}^2$	
Rate White Noise (ARW)	$N < 784 \rho_r / T_a{}^{5/2}$	$^\circ/\sqrt{h}$
Rate Bias Instability	$B < 8.93 \times 10^4 \rho_r / T_a{}^3$	$^\circ/h$
Rate Random Walk	$K < 10^7 \rho_r / T_a{}^{7/2}$	$^\circ/h^{3/2}$

Table 4. Summary of rate gyro parameter limits affecting antenna pointing error.

Parameter	***Criteria***	***Units***
Scale Factor Errors	$\Gamma_{\max} < 10^6 \beta \Theta_{z'}$	PPM
Misalignment and Nonorthogonality	N/A	
Rate White Noise	$N < 1718 \beta \Theta_{z'} / \sqrt{T_a}$	$^\circ/\sqrt{h}$
Rate Bias Instability	$B < 1.46 \times 10^5 \beta \Theta_{z'} / T_a$	$^\circ/h$
Rate Random Walk	$K < 1.07 \times 10^7 \beta \Theta_{z'} / T_a{}^{3/2}$	$^\circ/h^{3/2}$

Note that $\Theta_{z'}$ is reported in radians.

6.4 Examples

We now examine three selected radar application scenarios, and compare IMU requirements to several commercial IMUs.

6.4.1 Example Scenario Definition

Scenario #1

In this scenario we model a Ku-band SAR imaging broadside at 10 km range with 0.3 m resolution while traveling at 70 m/s (consistent with a Twin Otter aircraft). The synthetic aperture time is slightly greater than 5 s. The antenna azimuth beamwidth is 3.2 degrees, and the pointing tolerance is 0.03 beamwidths.

Scenario #2

In this scenario we model a Ku-band SAR imaging broadside at 10 km range with 0.1 m resolution while traveling at 36 m/s (consistent with a Predator A aircraft). The synthetic aperture time is approximately 30 s. The antenna azimuth beamwidth is 3.2 degrees, and the pointing tolerance is 0.03 beamwidths.

Scenario #3

In this scenario we model a Ku-band SAR imaging at a 45 degree squint angle at 25 km range with 0.1 m resolution while traveling at 36 m/s (consistent with a Predator A aircraft). The synthetic aperture time is approximately 104 s. The antenna azimuth beamwidth is 3.2 degrees, and the pointing tolerance is 0.03 beamwidths.

6.4.2 IMU Performance Requirements and Candidates

The three aforementioned scenarios and their IMU requirements are tabulated in Table 5 along with some specifications of candidate IMUs. Candidate IMU performance specifications are from the best grade of each IMU, and were collected from manufacturer data sheets, and a variety of literature sources.[1,17,45] Laboratory measurements indicate that IMUs often perform better than their specifications, but are used in the table only when other sources couldn't be found. Note that not all parameters for which we have developed criteria have corresponding specifications for the different IMUs.

Table 5. Example radar scenarios IMU requirements compared to Candidate IMU specifications.

IMU Parameter Comparrison									
		Scenario			Candidate IMU				
Parameter	Units	#1	#2	#3	LN-200	HG-1700	HG-1900	HG-1930	HG-9900
wavelength	m	0.018	0.018	0.018					
resolution	m	0.3	0.1	0.1					
velocity	m/s	70	36	36					
range	m	10000	10000	25000					
window broadening		1.18	1.18	1.18					
squint angle	deg	90	90	45					
antenna azimuth beamwidth	deg	3.2	3.2	3.2					
fractional pointing error		0.03	0.03	0.03					
synthetic aperture time	s	5.1	29.5	104.3					
antenna pointing error limit	deg	0.1	0.1	0.1					
Accelerometers									
Scale Factor	PPM	2346.07	22.982	1.839	**300**	**300**	**300**	**700**	**100**
Misalignment & Nonorthogonality	mrad	2.35	0.023	0.002	0.1	0.5			
Bias	ug				**300**	**1000**	**1000**	**4000**	**25**
White Noise (VRW)	ug/sqrt(Hz)	2321.38	54.922	8.262	16	150		44	0.6
Bias Instability	ug	1642.25	16.087	1.287	3.1			10	
Random Walk	ug/sqrt(s)	1199.74	4.866	0.207					
Rate Gyros - Position Error Limits									
Scale Factor	PPM	1173.03	11.491	0.919	**100**	**150**	**150**	**300**	**5**
Misalignment & Nonorthogonality	mrad	2.35	0.023	0.002	0.1	0.5			
Bias	deg/h				**1.0**	**1.0**	**1.0**	**20.0**	**0.003**
White Noise (ARW)	deg/sqrt(h)	4.09	0.017	0.001	**0.07**	**0.125**	**0.1**	**0.15**	**0.002**
Bias Instability	deg/h	207.14	0.348	0.008	0.35	1.0	**0.3**	5.5	0.003
Random Walk	deg/h^3/2	10314.61	7.172	0.086				30	
Rate Gyros - Pointing Error Limits									
Scale Factor	PPM	1675.52	1675.516	1675.516	**100**	**150**	**150**	**300**	**5**
Misalignment & Nonorthogonality	deg/h				0.1	0.5			
Bias	deg/h				**1.0**	**1.0**	**1.0**	**20.0**	**0.003**
White Noise (ARW)	deg/sqrt(h)	1.28	0.530	0.282	**0.07**	**0.125**	**0.1**	**0.15**	**0.002**
Bias Instability	deg/h	48.37	8.292	2.345	0.35	1.0	**0.3**	5.5	0.003
Random Walk	deg/h^3/2	1576.43	111.892	16.831				30.0	
					Note: Bold entries are from Manufacturer Data Sheets. Other entries are from other sources.				

Of the candidate IMUs, the HG-9900 is a navigation grade IMU. The LN-200, HG-1700, and HG-1900 are tactical grade IMUs, and the HG-1930 is a MEMS grade IMU.

6.4.3 Comments on example scenarios and candidate IMUs

As previously stated, accelerometer and gyro constant biases are assumed to be compensated by the EKF, and therefore assumed not relevant to navigation error growth and ultimately SAR image quality.

In all cases, for our examples, gyro limits are constrained more by range (position) error limits rather than pointing error limits. Should a requirement arise for Direction of Arrival measurements (e.g. IFSAR, Endo-clutter GMTI, etc.) then the pointing error limits might change, and the overall driver for requirements might change.

Scenario #1

This scenario's parameter requirements are easily met by all candidate IMUs.

Bottom Line: Any of the IMUs are acceptable, including the lowest performance HG-1930.

Scenario #2

For this scenario, with respect the IMU instrument noise parameters, only the HG-9900 meets the required performance limits. The next best IMU is the LN-200, which misses the rate gyro white noise (ARW) performance requirement by a factor of four. It might be argued that with a 'good' aiding scheme that can correct for some of the effects of this error during a synthetic aperture, the LN-200 might be made to work somewhat better, perhaps even adequately. Anecdotal evidence suggests that this is indeed the case. Nevertheless, the LN-200 by itself is judged to at best be marginal for this scenario. The HG-1700 and HG-1900 performances are expected to be somewhat worse than the LN-200. Note that the HG-1700 fails the accelerometer white noise (VRW) criteria whereas the LN-200 betters it. The HG-1930 is more than twice as noisy as the LN-200.

Scale factors for the accelerometers are seemingly inadequate by a factor of 13 for the LN-200, HG-1700, and HG-1900, and by a factor of 30 for the HG-1930. The HG-9900 fails the accelerometer scale factor requirement by a factor of 5. In the previous discussions, scale factor error limits were deemed very 'squishy', and are justifiably relaxed for shallow grazing angles and benign flight paths. As a result, although not meeting this performance requirement should raise a warning flag for further analysis or testing, it does not automatically rule these IMUs out. Instead, qualifiers of geometry limits or maneuver limits might be imposed. The factor of 5 for the HG-9900 accelerometer scale factor is easily relaxed by limiting the 10 km range to somewhat shallower grazing angles. Doing so for the factor of 13 for the LN-200, HG-1700, and HG-1900 is a little more iffy, but the factor of 30 for the HG-1930 is very worrisome.

The scale factors for the rate gyros are seemingly inadequate by a factor of 9 to 13 for the LN-200, HG-1700, and HG-1900, and by a factor of 26 for the HG-1930. The HG-9900 meets the gyro scale factor requirement. Similarly, the rate gyro scale factors for the LN-200, HG-1700, and HG-1900 require a more benign flight path than was presumed for the requirement, and the HG-1930 requires a more benign flight path yet.

Bottom Line: The HG-9900 will likely work very well. The LN-200 is marginal, but is likely acceptable with good aiding. The HG-1700 and HG-1900 will perform worse. The HG-1930 should be considered unacceptable for this scenario.

Scenario #3

For this scenario, none of the IMUs strictly meet the performance requirements. The closest to meeting these is the HG-9900. The rate gyro white noise (ARW) performance of the HG-9900 is within a factor of two for being adequate for this scenario. With good aiding, this is likely adequate, although we might still expect occasional excessive motion

measurements errors due to gyro bias variations. The other IMUs are two orders of magnitude worse in this performance parameter, and it is difficult to conceive of an easy way to overcome this.

The HG-9900 accelerometer scale factor error specification is about 50 times greater than the requirement allows. The other IMUs are 3 to 7 times worse than the HG-9900. Even accounting for shallow grazing angles to relieve this requirement somewhat, it is likely that a good aiding scheme that operates during a synthetic aperture is still required for acceptable performance even from the HG-9900. Nevertheless, further testing and analysis is called for.

The HG-9900 IMU's rate gyro scale factor error specification is about 5 times too large for the requirement. The squishiness of this parameter suggests that by limiting the radar to benign flight paths, the HG-9900 is probably acceptable in this regard. The other IMUs are 20 to 60 times worse than the HG-9900, and again two orders of magnitude or more from the performance level desired.

Bottom Line: With good aiding, the HG-9900 is likely adequate. The other IMUs are not likely to yield acceptable performance. Very good aiding and enhanced autofocus techniques might be considered if tactical-grade IMUs are a constraint.

6.4.4 Some Final Comments

Clearly, while the foregoing analysis resulted in analytical parameter limits for IMU selections, care should be taken to appreciate the limitations of these criteria.

A number of approximations and simplifications were made to arrive at the analytical parameter limits. Consequently, these analytical parameter limits should themselves not be hard selection criteria between various IMUs. They might be employed to provide a basic first-order selection. Should an IMU not meet these requirements, depending on the degree of its inadequacy, a number of options exist that might yet tolerate its weaknesses, and still render useful navigation. Some of these options will be discussed later.

Furthermore, the degree and performance of aiding schemes may also have a significant impact on acceptable navigator performance. Alternatively, the results of the above analysis might indicate when a higher performance aiding scheme might be called for.

Finally, this analysis should not be used as a substitute for high fidelity simulations or extensive testing to validate the performance of an instrument or more generally the navigation sub-system. As the tables indicate, manufacturer data sheets are often incomplete. Consequently, after initial down-selection, the next step in navigator design is to acquire and comprehensively test candidate IMUs to fill in the knowledge gaps.

6.5 A Note About Simulations

Further insight into the behavior of IMUs for SAR applications can be had by simulating the IMU with high fidelity for the various scenarios under consideration. As with all simulations in general, any one simulation is merely one member of an ensemble of possible outcomes for a number of random variables and processes. Consequently, for simulations to be valuable, many trials need to be run with various parameter variations, i.e. a Monte Carlo analysis, for a good statistical measure. Nevertheless, extending the comparison of this report, a high-fidelity simulation would be expected to allow for the complex interactions of various IMU characteristics with a full 3-D IMU excitation.

Furthermore, a simulation can be expanded to incorporate any IMU aiding scheme and evaluate complete navigation performance. This was, for example, the approach taken by Pedlar and Coe.[46]

However, the criteria for which a simulation result is evaluated remains unchanged from that of our analytical results. That is, the allowable range error for the navigator needs to be within the capabilities of what a SAR autofocus algorithm can correct. For a conventional autofocus, this means that the allowable nonlinear range error variation during a synthetic aperture be limited to less than the range resolution of the SAR.

We also retain the following criteria for SAR,

Sinusoidal Phase Error less than 1 degree (peak), and

Random phase error less than 1 degree standard deviation.

6.6 More Comments About S-turns – How Often?

We have ignored aiding the IMU in the development of parameter limits thus far, for the reasons cited previously. We briefly digress now to one aspect of GPS-aiding discussed in Section 3, namely heading error accumulation. As shown, reducing uncertainty in this error requires maneuvers with large extended horizontal accelerations, as with S-turns. The question we address now is "How often do we need to perform S-turns (or other suitable maneuvers)?"

The heading error uncertainty is simply an accumulated orientation (angle) error uncertainty. We will adopt a very simple criterion for the period between S-turns, namely

1. to initiate an S-turn, the accumulated heading error uncertainty needs to exceed some upper threshold for the pointing error for the antenna, and

2. S-turns are employed to reduce the heading error uncertainty to below some lower threshold.

We note that over the scale of minutes to tens of minutes, the significant rate gyro noise sources include white noise (ARW) and bias instability. Due to published parameter availability, we confine ourselves to these two noise sources. Consequently, the total standard deviation in the angle error due to the combined noise sources is

$$\sigma_\theta = \sqrt{{\sigma_{\theta 3}}^2 + {\sigma_{\theta 4}}^2} \,. \tag{296}$$

Of course, this can be expanded and related to time as

$$\sigma_\theta = 4.85 \times 10^{-6} \sqrt{3600 N^2 t + \left(\frac{B^2}{2} \right) t^2} \qquad \text{rad} \,. \tag{297}$$

The time it takes to achieve a particular total uncertainty can be solved for using the quadratic formula as

$$t = \frac{-3600 N^2 + \sqrt{1.296 \times 10^7 N^4 + 8.503 \times 10^{10} B^2 {\sigma_\theta}^2}}{B^2} \qquad \text{s.} \tag{298}$$

If we define heading uncertainty limits as follows:

$$\begin{aligned} \sigma_\theta = \sigma_{\theta,upper} &= \text{condition for initiating an S-turn maneuver, and} \\ \sigma_\theta = \sigma_{\theta,lower} &= \text{condition for ceasing an S-turn maneuver,} \end{aligned} \tag{299}$$

then the time period between S-turns can be calculated as

$$T_{\text{S-turn}} = \frac{\left[\sqrt{1.296\times10^{7}N^{4} + 8.503\times10^{10}B^{2}\sigma_{\theta,upper}^{2}} - \sqrt{1.296\times10^{7}N^{4} + 8.503\times10^{10}B^{2}\sigma_{\theta,lower}^{2}}\right]}{B^{2}} \quad \text{s.} \tag{300}$$

The question becomes "What are good heading uncertainty limits for initiating and ending S-turns?"

Anecdotal evidence suggests that reasonable performance is obtained if

$$\begin{aligned} &\sigma_{\theta,upper} \approx 70\% \text{ of } \beta\Theta_{z'}, \text{ and} \\ &\sigma_{\theta,lower} < 70\% \text{ of } \sigma_{\theta,upper}. \end{aligned} \tag{301}$$

Recall that $\beta\Theta_{z'}$ is the pointing error limit in radians.

Example: LN-200 IMU

The LN-200 IMU specifications are given in Table 5. A sample IMU was measured to have values for *N* and *B* of approximately half the specification. The time to reach a particular heading uncertainty is plotted in Figure 15, for both an IMU operating at the limit of the specification, and the sample IMU.

We choose uncertainty thresholds of

$$\begin{aligned} &\sigma_{\theta,upper} = 0.00122 \text{ rad} = 0.07 \text{ deg, and} \\ &\sigma_{\theta,lower} = 0.00087 \text{ rad} = 0.05 \text{ deg.} \end{aligned} \tag{302}$$

We can then calculate

$$\begin{aligned} &T_{\text{S-turn}} \approx 5 \text{ minutes for the specification, and} \\ &T_{\text{S-turn}} \approx 10 \text{ minutes for the sample IMU.} \end{aligned} \tag{303}$$

Of course, there is no guarantee that the heading error will grow to the limit in the time calculated, as the calculation is just a statistical expected value. Nevertheless, we should not be surprised at these heading uncertainty growth rates based on the IMU's performance parameters.

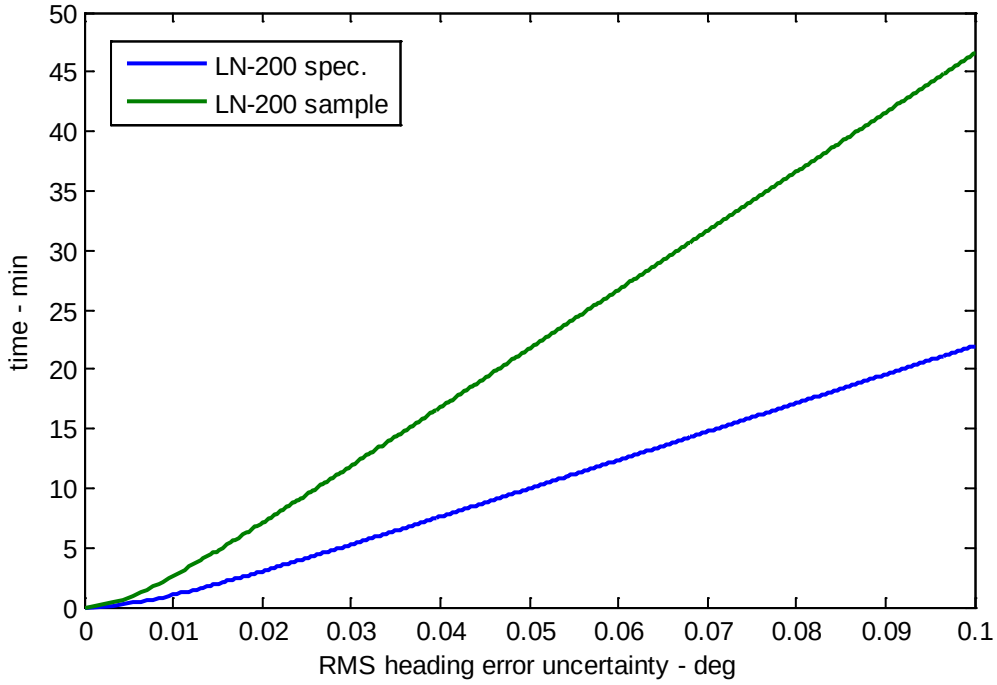

Figure 15. Heading uncertainty growth from perfect alignment.

Example: Other IMUs

Using the same criteria as for the LN-200, the other IMUs in Table 5 were also assessed for S-Turn recommended periods. These are summarized as

LN-200	~5 minutes
HG-1700	~2 minutes
HG-1900	~5 minutes
HG-1930	~20 seconds
HG-9900	~9 hours

Note that this presumes the IMUs performing at the limit of their respective specifications. We would generally expect a sample IMU to perform better than the limit, but of course this cannot be guaranteed. In addition, other rate gyro noise terms become significant over longer integration times. These have not been included in the S-turn period requirement, but would serve to reduce the given times somewhat.

6.7 What if we can't get a good enough IMU?

The choice of an IMU for a SAR system will often depend on many factors in addition to navigation performance, including size, weight, cost, delivery, etc. Indeed, scenarios can be conjured where even the best IMU will not be guaranteed to perform 'good enough' for high-quality SAR image formation. Sometimes you just can't get the IMU you want. Consequently, it is useful to examine some alternatives for dealing with otherwise inadequate IMU performance.

1. As previously indicated, the manifestation of acceleration scale factor errors in SAR image quality depends on imaging geometry, having a lesser influence at shallower grazing angles. Likewise, rate gyro scale factor errors depends on the degree of maneuver during the synthetic aperture, having a lesser influence for benign flight paths. Consequently, limiting imaging geometry or aircraft maneuver would allow using a lesser quality IMU (with respect to scale factor errors) that what would otherwise be required.

2. The IMU performance requirements assumed no aiding of the IMU during a synthetic aperture. Incorporating such intra-aperture aiding might mitigate the position errors somewhat before they are accumulated. Aiding during a synthetic aperture must avoid adding any discontinuities in the phase error, and preferably none in the phase gradient either. This is required because the autofocus algorithms conventionally used have great difficulty dealing with high-frequency components in the phase error.

3. The range error limits used to develop the IMU instrument error requirements presumed a conventional autofocus for SAR. Employing a more general autofocus that corrects residual migrations greater than the range resolution would allow relaxing the requirements for the IMU.

4. Limiting radar geometry and motion so as to fly the synthetic aperture quicker would allow a shorter aperture time, thereby allowing less instrument drift. Basically this means to fly faster and closer to the target scene.

6.8 Other Frequently Asked Questions

We address some residual frequently asked questions.

Will better GPS help keep down heading uncertainty?

Probably not – From the earlier analysis, the problem is that the orientation of the IMU about the vertical axis is not observable in straight and level flight. Consequently, even with perfect GPS measurements, nothing changes about the observability of the necessary error. However, since multiple GPS observations are requires during an S-turn, or comparable maneuver, for among other things to beat down the noise in GPS measurements, a higher-fidelity set of GPS measurements might allow shorter measurement times with lesser horizontal accelerations to suffice. Basically, this might allow bringing down errors during an S-turn quicker due to less noisy GPS measurements, but not reduce the need for them.

Will a calibrated IMU reduce the need for S-turns?

Probably not – IMU orientation uncertainty is driven by rate gyro noise. Since the noise is random, it is unpredictable, except in a statistical sense. Nevertheless, the noise is not controllable, and consequently knowledge of its statistics cannot mitigate the heading error or its growth. However, understanding the noise statistics via a calibration procedure does help us predict bounds on the error growth better, but not make its growth slower. Knowledge of the growth statistics will however help us 'tune' the EKF for better overall navigation performance.

Can we have good navigation for SAR and nevertheless have bad antenna pointing?

Possibly yes – For SAR focusing and target location, the navigation accuracy required is principally in the relative positions from which the data is collected, that is, the translational motion of the radar. For target scene illumination, the navigation accuracy required includes accurate translational motion, but also the rotational orientation of the radar antenna. From the earlier analysis, in straight and level flight, translational motion can be measured and corrected, but heading angle cannot. Consequently, it is conceivable that the SAR image can be well focused and with good location accuracy, but antenna pointing is still unacceptably 'off'.

Can slewing the gimbal substitute for (or aid) S-turns?

Probably not – to estimate heading error, the IMU needs an extended period of accelerations with sufficiently large horizontal motion to also be measurable by the GPS instrument. Gimbal slewing is unlikely to provide either.

Is calibrating the IMU worthwhile?

Mixed bag – With noise characteristics, we get what we get, but calibration can tell us what we do get to help tune the EKF. With scale factors, a short term improvement can sometimes be had, but the 'better' numbers are generally unstable over time.[†]

Is there any reason why IMU or navigator performance should be different in different radar modes, e.g. SAR and GMTI?

Not really – This is true for antenna pointing. A case could be made that with aiding during a synthetic aperture, that target location accuracy may be somewhat better for longer synthetic apertures, e.g. finer resolutions.

Can even the best IMU be not good enough sometimes?

Yes – As previously mentioned, for this development we have assumed an atmosphere between radar and target scene that relates phase exactly proportional to range, which in fact is generally not true. The atmosphere does distort the 'electrical range' so that even perfect motion measurement cannot prevent phase errors manifesting in the SAR image.[29] Denny & Scott[47] claim that "the performance of future high-resolution SAR modes will be limited by anomalous propagation effects, rather than by platform measurement errors or focusing algorithm limitations, or RF wavelength." Their evidence suggests that ranges of 25 km or so will already at times cause an atmosphere-induced apparent range error variation exceeding 0.1 m, judged debilitating based on conventional autofocus for these fine resolutions. This implies that a more general autofocus might be required even with error-free motion measurement.

Can multiple antenna phase centers or beams help?

Yes – multiple phase centers or beams allow, depending how they are arranged, independent measures of DOA. These measures can be compared with Doppler-derived DOA estimates to align the antenna with respect to heading error. For SAR, this is described in a report by Doerry.[26] In GMTI, this is sometimes referred to as "Cal on Clutter."

[†] Ted Kim, of Sandia Natinal Laboratories, opines that calibrating rate gyro scale factors "Maybe can improve short term performance by 2x". (email sent Tuesday, September 23, 2008 12:46 PM)

7 Conclusions

7.1 Summary Comments

The following summary points are worth repeating.

- IMUs are comprised of inertial sensing instruments with limited precision and accuracy. The degree of variation in precision and accuracy across the various IMUs offered by vendors is quite large.

- The precision and accuracy of the accelerometers and rate gyros that typically make up an IMU are limited by a variety of scale factor errors, misalignment and nonorthogonality of the instruments, and a variety of noise terms.

- The various error sources in the accelerometers and rate gyros can be analytically related to an accumulated position error, which in turn provides a range error between radar and target, and ultimately manifests as a phase error to the radar, thereby degrading the data quality.

- Autofocus techniques can mitigate phase errors to some limited extent. Different autofocus techniques and implementations can mitigate phase errors to different extents. Conventional autofocus techniques can mitigate phase errors up to a corresponding range error equal to the range resolution of the SAR. In this case, motion measurement needs to provide fidelity sufficient to not vary the range error more than the range resolution of the SAR during its synthetic aperture.

- The allowable range error variation over a synthetic aperture can be related to limits on various error sources of the IMU instruments. These limits on various IMU instrument error sources define a minimum level of precision and accuracy of the IMU, and can be used to provide initial selection criteria for candidate IMUs for a specific SAR performance parameter space.

- The analysis that leads to analytical qualifications does make a number of approximations and assumptions, just to make the task tractable. While the analytical results might be useful for initial selection criteria between candidate IMUs, they do not substitute for extensive testing and high-fidelity simulations to assess likely performance.

7.2 Design Recommendations

Based on the analysis in this report, we suggest the following design procedure for a SAR system, including its motion measurement capabilities.

1. From basic SAR system performance requirements, select an IMU using the criteria developed above in this report. Presume the use of conventional autofocus for SAR image formation. Candidate IMUs should be extensively tested and simulated as part of the navigation subsystem.

2. Design an aiding scheme for the IMU. This should include attention to operational concepts and limitations regarding, for example, any S-turns or other relevant procedures. The entire navigation subsystem should be extensively tested and simulated to facilitate performance prediction for the entire SAR system.

3. Examine the larger operational parameter space for the SAR system for deficient performance by the IMU and the larger navigation subsystem with respect to excessive range error variations. Select conditions for which migration corrective autofocus needs to be employed, and design in this autofocus capability with perhaps triggers for its optional employment.

4. Examine the larger operational parameter space for the SAR system for deficient performance by the IMU with respect to antenna pointing due to heading errors. Select conditions for which data-driven antenna pattern correction is needed, and design in this capability with perhaps triggers for its optional employment.

Appendix A – Allan Variance

The Allan variance, named after David W. Allen, also known as two-sample variance, is a measurement of stability. Originally developed for measuring clock frequency stability, it is readily applicable to measuring the stability of IMU parameters.

A number of references are listed on David Allen's own web site.[‡] A number of other independent references also exist, and are easily found in the literature. This includes an IEEE Standard with an Appendix describing Allan variance measurements.[48]

The Allan variance is calculated via the following procedure:

1. Collect contiguous samples x_n for $1 \le n \le N_{total}$ at a sampling rate f_s.

2. Divide the N_{total} samples into groups of contiguous samples of length N_{group}. Note that N_{group} represents a time interval of

$$\tau = N_{group} / f_s \tag{A1}$$

and there are K total groups where

$$K = \text{floor}\left(N_{total} / N_{group}\right). \tag{A2}$$

3. Calculate the mean value for each group, and collect the results. That is

$$y_k(\tau) = \frac{1}{N_{group}} \left(\sum_{n=(k-1)N_{group}+1}^{kN_{group}} x_n \right) \text{ for } 1 \le k \le K. \tag{A3}$$

4. Calculate the Allen variance for this specific τ as

$$AVAR(\tau) = \frac{2}{2(K-1)} \sum_{k=1}^{K-1} \left(y_{k+1}(\tau) - y_k(\tau) \right)^2. \tag{A4}$$

5. Repeat for new N_{group}.

6. Plot $\sqrt{AVAR(\tau)}$ versus τ typically on a Log-Log plot.

[‡] http://www.allanstime.com/AllanVariance/

Note that if τ is such that K is less than 10 or so, then the statistics become somewhat unreliable.

The square root of Allan variance is often referred to as Allan deviation. This is what is typically plotted on the log-log scale.

A low Allan variance is a characteristic of a clock with good stability over the measured period. A typical Allan variance plot for an angular rate sensor is given in Figure 16.

The various slopes and features of the plot indicate different instability mechanisms as dominating at the various time scales. An Allan variance curve is typically U-shaped in the log-log plot.

> A slope of –1 indicates a region dominated by 'quantization noise' due to digital encoding of the sensor outputs.
>
> A slope of –1/2 indicates a region dominated by a 'random walk' component. The source seems to be white noise in the rate-gyro in the case of angular random walk, and the accelerometers themselves for a velocity random walk.
>
> A slope of 0 indicates a region dominated by 'bias instability'. This is generally at the bottom of the 'U'. This seems to be generally attributed to flicker noise in the electronic components.
>
> A slopes of +1/2 indicates a region dominated by a 'rate random walk'.
>
> A slopes of +1 indicates a region dominated by a 'drift rate ramp'.

Figure 17 summarizes the expected locations of these various instability manifestations on an Allan variance plot.

Furthermore, we note that the Allan variance is related to the two-sided Power Spectral Density (PSD) of the error as follows

$$AVAR(\tau) = 4\int_0^\infty S(f)\frac{\sin^4(\pi f\tau)}{(\pi f\tau)^2}df \ . \tag{A5}$$

where

$S(f)$ = two-sided PSD of the error signal. (A6)

Finally, we note that the application of Allan variance analysis to accelerometer and rate-gyro noise parameters is also well documented in the literature.[13,49,50]

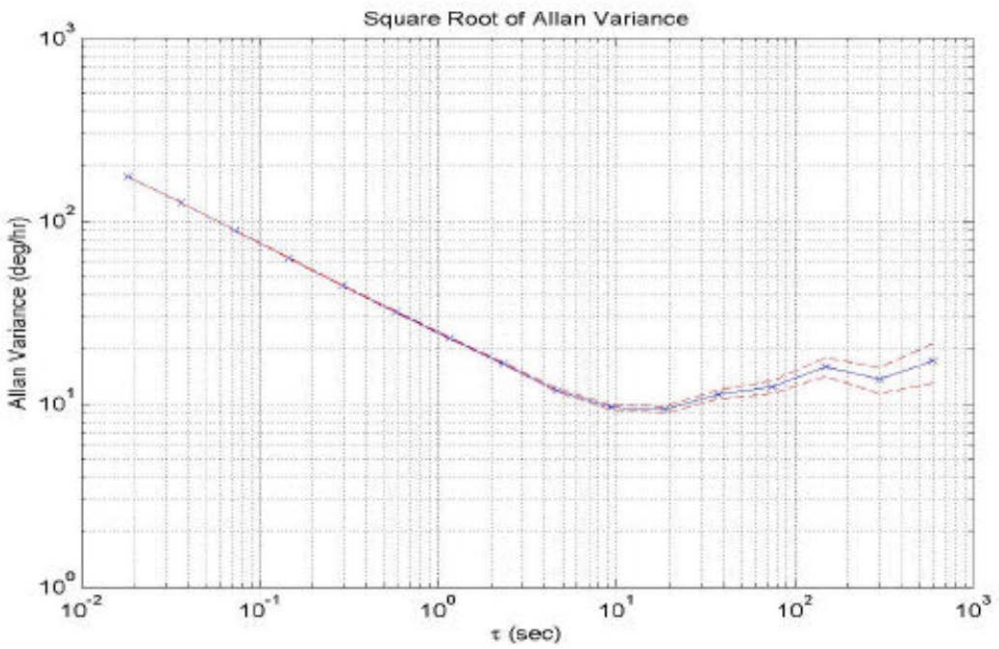

Figure 16. Typical Allan variance curve for an angular rate sensor. (Courtesy Dr. Walter Stockwell, Crossbow Technology, Inc., http://www.xbow.com)

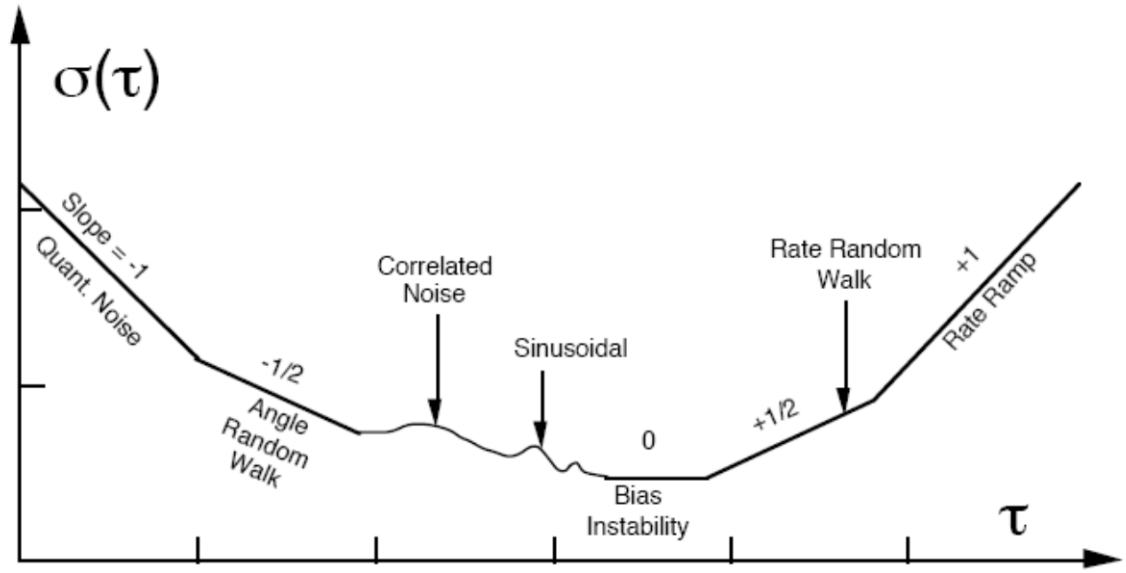

Figure 17. Typical Allan variance regions corresponding to specific instability sources for a Fiber Optic Gyro (FOG). Both axes are logarithmic. (Fig. C.8 in IEEE Std 952-1997 [48])

"I wish I had an answer to that because I'm tired of answering that question."
-- Yogi Berra

Appendix B – Random Walk

The term Random Walk (RW) denotes a process whereby a trajectory is generated by taking random steps (perhaps in size and or direction). This model finds utility in a wide variety of applications. There are many variations on the basic theme, with different probability distributions to describe the steps. Random Walk processes also go by a variety of other names, some of which are quite colorful, e.g. drunkards walk, Levy flight, etc. In the limit, a Random Walk describes Brownian Motion. Most Random Walk processes are related to Markov Processes, and Markov Chains.

We will discuss here a very specific Random Walk model; one generated by integrating White Gaussian Noise (WGN).

Consider sampled data of a zero-mean WGN process, with the following parameters.

f_S = the sampling frequency,

σ_x^2 = the variance of each individual sample. (B1)

Furthermore, we can calculate

$T_S = 1/f_S$ = the sample period, and

$N_0/2 = T_S\sigma_x^2$ = the Power Spectral Density of the noise process. (B2)

We denote the individual samples as

x_i = sample with index *i*, where $i \geq 1$. (B3)

Consequently, an ensemble of samples define the random sequence

$x_1, x_2, x_3, x_4, x_5, \ldots$ = random sequence. (B4)

Integrating (accumulating) this sequence generates the Random Walk. The number of times it is integrated denotes the order of the Random Walk.

Discrete-Time First Order Random Walk

Consider the random process generated as follows.

$$y_1(T) = T_S \sum_{i=1}^{I} x_i \,. \tag{B5}$$

where

$T = IT_S$ = the time over which the integration takes place. (B6)

This can be expanded to

$$\begin{aligned} y_1(T_s) &= T_s(x_1) \\ y_1(2T_s) &= T_s(x_1 + x_2) \\ y_1(3T_s) &= T_s(x_1 + x_2 + x_3) \\ y_1(4T_s) &= T_s(x_1 + x_2 + x_3 + x_4). \end{aligned} \tag{B7}$$

This integration of WGN is termed a 'First Order' Random Walk.

Since we are accumulating zero-mean WGN samples, $y_1(T)$ is also zero-mean and Gaussian, but no longer white, i.e. no longer uncorrelated samples. The variance of $y_1(T)$ is dependent on *T* and is calculated as follows.

$$\sigma_{y_1}^2 = E\left\{ \left| y_1(T) \right|^2 \right\} = T_s^2 \sum_{i=1}^{I} \sigma_x^2 = T_s^2 I \sigma_x^2 = T_s T \sigma_x^2. \tag{B8}$$

Note also that this can be written in terms of PSD as

$$\sigma_{y_1}^2 = T(N_0/2). \tag{B9}$$

The important point to note here is that the variance $\sigma_{y_1}^2$ grows linearly with *T*. This is more often stated as the standard deviation σ_{y_1} grows as $\sqrt{T}$. Figure 18 illustrates several cases of a First Order Random Walk, all with input noise using the same sampling and statistics parameters.

Discrete-Time Second Order Random Walk

Consider the random process generated by double-accumulating the noise samples, namely

$$y_2(T) = T_s \sum_{i=1}^{I} \left(T_s \sum_{j=1}^{i} x_j \right). \tag{B10}$$

This can be expanded to

$$\begin{aligned} y_2(T_s) &= T_s^2(x_1) \\ y_2(2T_s) &= T_s^2(2x_1 + x_2) \\ y_2(3T_s) &= T_s^2(3x_1 + 2x_2 + x_3) \\ y_2(4T_s) &= T_s^2(4x_1 + 3x_2 + 2x_3 + x_4). \end{aligned} \tag{B11}$$

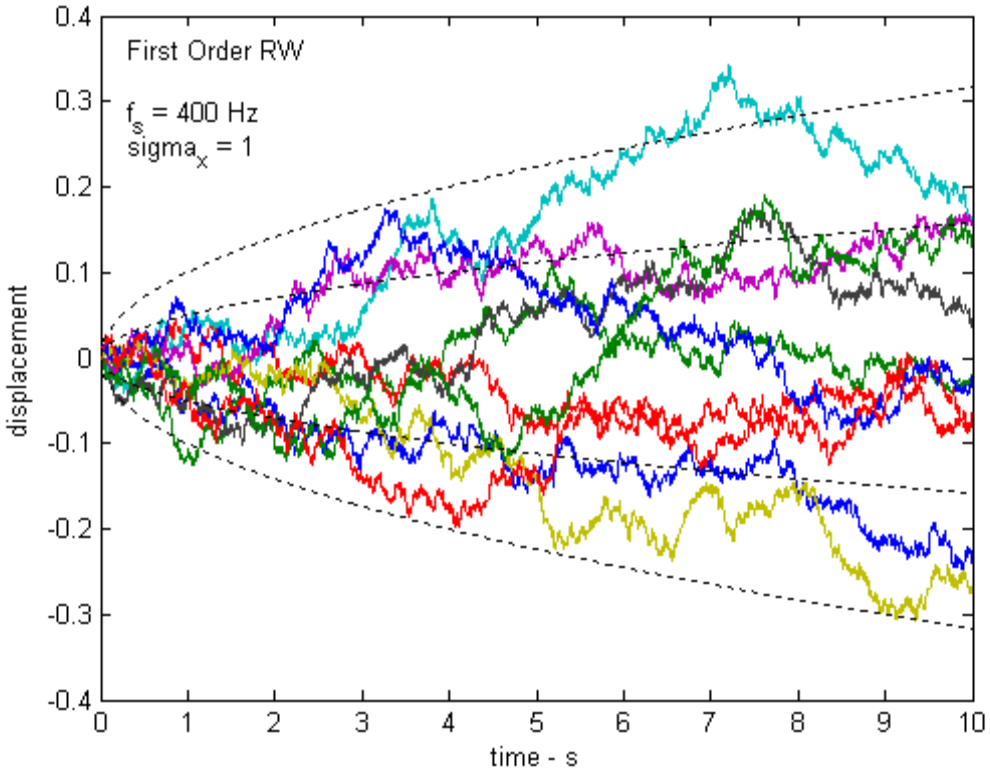

Figure 18. Ten examples of a First Order RW. Dotted lines show one and two standard deviations of the expected displacement.

This defines the 'Second Order' Random Walk. This can be reformulated to the summation

$$y_2(T) = T_s^2 \sum_{i=1}^{I} (I - i + 1) x_i \,. \tag{B12}$$

The variance of $y_2(T)$ is calculated to be

$$\sigma_{y_2}^2 = T_s^4 \sum_{i=1}^{I} (I - i + 1)^2 \sigma_x^2 = T_s^4 \left(\frac{I(I+1)(2I+1)}{6} \right) \sigma_x^2 \,. \tag{B13}$$

This is approximated for large I as

$$\sigma_{y_2}^2 = T_s^4 \left(\frac{I^3}{3} \right) \sigma_x^2 = \frac{1}{3} T^3 T_s \sigma_x^2 \,. \tag{B14}$$

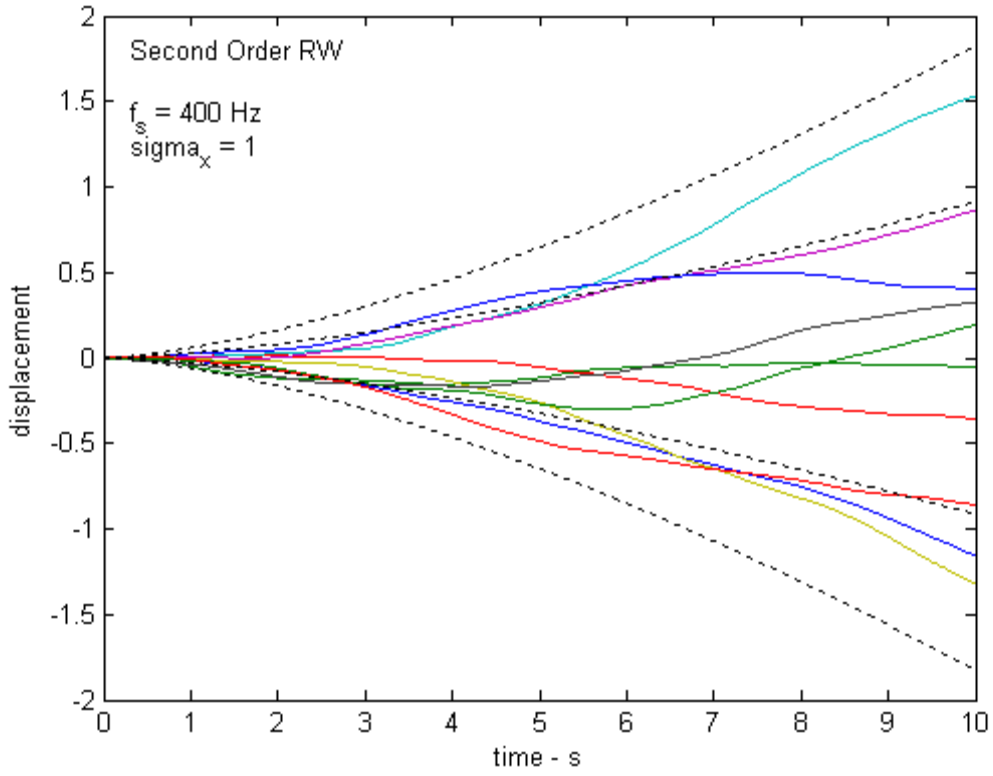

Figure 19. Ten examples of a Second Order RW. Dotted lines show one and two standard deviations of the expected displacement.

In terms of the PSD, this becomes

$$\sigma_{y_2}^2 = \frac{1}{3}T^3(N_0/2). \tag{B15}$$

The important point to note here is that the variance $\sigma_{y_2}^2$ grows with T^3. This is more often stated as the standard deviation σ_{y_2} grows as $T^{3/2}$. Figure 19 illustrates several cases of a Second Order Random Walk, all with input noise using the same sampling and statistics parameters.

<u>Discrete-Time Third Order Random Walk</u>

Consider the random process generated by triple-accumulating the noise samples, namely

$$y_3(T) = T_s \sum_{i=1}^{I} \left(T_s \sum_{j=1}^{i} \left(T_s \sum_{k=1}^{j} x_k \right) \right). \tag{B16}$$

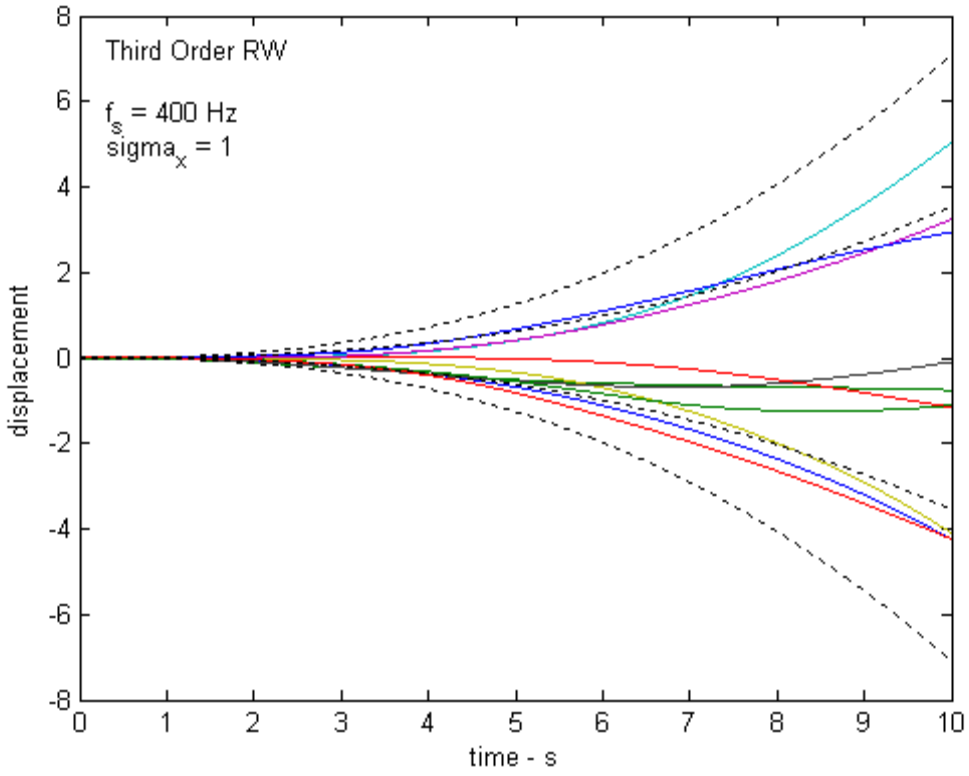

Figure 20. Ten examples of a Third Order RW. Dotted lines show one and two standard deviations of the expected displacement.

This can be expanded to

$$\begin{aligned} y_3(T_s) &= T_s^3(x_1) \\ y_3(2T_s) &= T_s^3(3x_1 + x_2) \\ y_3(3T_s) &= T_s^3(6x_1 + 3x_2 + x_3) \\ y_3(4T_s) &= T_s^3(10x_1 + 6x_2 + 3x_3 + x_4). \end{aligned} \tag{B17}$$

This defines the 'Third Order' Random Walk. This can be reformulated to the summation

$$y_3(T) = T_s^3 \sum_{i=1}^{I} \left(\frac{(I-i+1)(I-i+2)}{2} \right) x_i \,. \tag{B18}$$

The variance of $y_3(T)$ is calculated to be

$$\sigma_{y_3}^2 = T_s^6 \sum_{i=1}^{I} \left(\frac{(I-i+1)(I-i+2)}{2} \right)^2 \sigma_x^2 = T_s^6 \left(\frac{I(I+1)(I+2)\left(3I^2+6I+1\right)}{60} \right) \sigma_x^2 . \tag{B19}$$

This is approximated for large I as

$$\sigma_{y_3}^2 = T_s^6 \left(\frac{I^5}{20} \right) \sigma_x^2 = \frac{1}{20} T^5 T_s \sigma_x^2 . \tag{B20}$$

In terms of the PSD, this becomes

$$\sigma_{y_3}^2 = \frac{1}{20} T^5 (N_0/2). \tag{B21}$$

The important point to note here is that the variance $\sigma_{y_3}^2$ grows with T^5. This is more often stated as the standard deviation σ_{y_3} grows as $T^{5/2}$. Figure 20 illustrates several cases of a Third Order Random Walk, all with input noise using the same sampling and statistics parameters.

<u>Discrete-Time Fourth Order Random Walk</u>

Consider the random process generated by 4-stage accumulating the noise samples, namely

$$y_4(T) = T_s \sum_{i=1}^{I} \left(T_s \sum_{j=1}^{i} \left(T_s \sum_{k=1}^{j} \left(T_s \sum_{l=1}^{k} x_l \right) \right) \right). \tag{B22}$$

This can be expanded to

$$\begin{aligned} y_4(T_s) &= T_s^4 (x_1) \\ y_4(2T_s) &= T_s^4 (4x_1 + x_2) \\ y_4(3T_s) &= T_s^4 (10x_1 + 4x_2 + x_3) \\ y_4(4T_s) &= T_s^4 (20x_1 + 10x_2 + 4x_3 + x_4). \end{aligned} \tag{B23}$$

This defines the 'Fourth Order' Random Walk. This can be reformulated to the summation

$$y_4(T) = T_s^4 \sum_{i=1}^{I} \left(1 + \frac{(I-i)\left(11-6i+i^2+6I-2Ii+I^2\right)}{6} \right) x_i . \tag{B24}$$

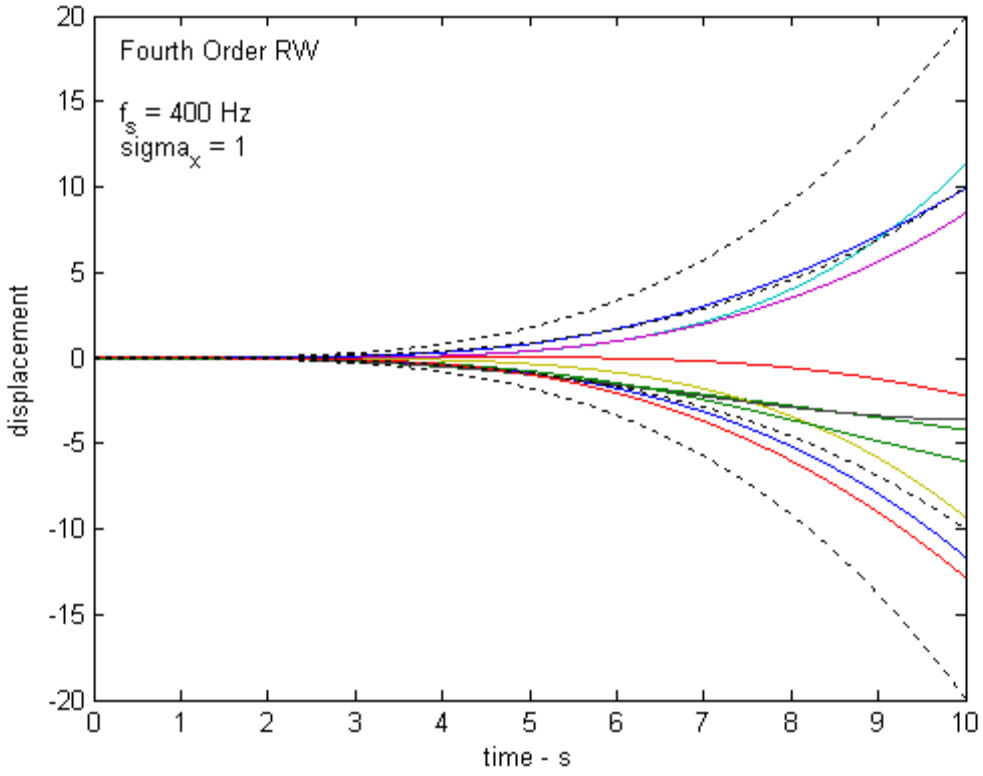

Figure 21. Ten examples of a Fourth Order RW. Dotted lines show one and two standard deviations of the expected displacement.

The variance of $y_4(T)$ is calculated to be

$$\begin{aligned}\sigma_{y_4}^2 &= T_s^8 \sum_{i=1}^{I} \left(1 + \frac{(I-i)\left(11 - 6i + i^2 + 6I - 2Ii + I^2\right)}{6}\right)^2 \sigma_x^2 \\ &= T_s^8 \left(\frac{I\left(10I^6 + 105I^5 + 427I^4 + 420I^3 - 1725I^2 - 4305I + 7578\right)}{2520}\right)\sigma_x^2 .\end{aligned} \tag{B25}$$

This is approximated for large I as

$$\sigma_{y_4}^2 = T_s^8 \left(\frac{I^7}{252}\right)\sigma_x^2 = \frac{1}{252} T^7 T_s \sigma_x^2 . \tag{B26}$$

In terms of the PSD, this becomes

$$\sigma_{y_4}^2 = \frac{1}{252} T^7 (N_0/2). \tag{B27}$$

The important point to note here is that the variance $\sigma_{y_4}^2$ grows with T^7. This is more often stated as the standard deviation σ_{y_4} grows as $T^{7/2}$. Figure 21 illustrates several cases of a Fourth Order Random Walk, all with input noise using the same sampling and statistics parameters.

Discrete-Time General Comments

In general, an M^{th} order accumulation will yield at time $T = T_s I$ the series

$$y_M(T_s I) = T_s^M \left(C_1(M,I)x_1 + C_2(M,I)x_2 + C_3(M,I)x_3 + ... + C_I(M,I)x_I\right). \quad \text{(B28)}$$

We identify

$$C_i(M,I) = C_i(M,I-1) + C_i(M-1,I), \quad \text{(B29)}$$

and the properties

$$\begin{aligned} &C_i(M,I) = 0 \text{ for } i > I, \\ &C_i(M,i) = 1, \\ &C_i(1,I) = 1. \end{aligned} \quad \text{(B30)}$$

The variance $\sigma_{y_M}^2$ from such a series will grow with T^{2M-1}. This is more often stated as the standard deviation σ_{y_M} grows as $T^{M-1/2}$. Generally, as the order of integration increases, the variance will grow faster with time.

Continuous Time

The same results can be calculated in continuous time.

Consider a White Gaussian Random Process defined as

$$x(t) = \text{input random process}, \quad \text{(B31)}$$

with autocorrelation function

$$R(t_1,t_2) = \frac{N_0}{2}\delta(t_1 - t_2). \quad \text{(B32)}$$

Continuous-Time First Order Random Walk

We calculate the First Order Random Walk as

$$y_1(T) = \int_0^T x(t)dt\,. \tag{B33}$$

The output variance is calculated as

$$\sigma_{y_1}^2 = E\left\{\left|y_1(T)\right|^2\right\} = E\left\{\int_0^T x(t_1)dt_1 \int_0^T x(t_2)dt_2\right\}, \tag{B34}$$

which becomes

$$\sigma_{y_1}^2 = \int_0^T\int_0^T E\{x(t_1)x(t_2)\}dt_1dt_2 = \int_0^T\int_0^T R(t_1,t_2)dt_1dt_2\,. \tag{B35}$$

This can be expanded to

$$\sigma_{y_1}^2 = \int_0^T\int_0^T \frac{N_0}{2}\delta(t_1-t_2)dt_1dt_2\,. \tag{B36}$$

Performing the integrations yields

$$\sigma_{y_1}^2 = \int_0^T \frac{N_0}{2}dt_2 = \frac{N_0}{2}T\,. \tag{B37}$$

This corresponds exactly with the earlier result using sampled data.

Continuous-Time Second Order Random Walk

We calculate the Second Order Random Walk as

$$y_2(T) = \int_0^T\left(\int_0^\tau x(t)dt\right)d\tau\,. \tag{B38}$$

This needs to eventually be written as a single integration over *t*, which necessitates changing the order of integration. Consequently, we do this with appropriate changes in integration limits and get

$$y_2(T) = \int_0^T \left(\int_0^\tau x(t)dt \right) d\tau = \int_0^T \left(x(t) \int_t^T d\tau \right) dt = \int_0^T x(t)(T-t)dt \,. \tag{B39}$$

The output variance is calculated as

$$\sigma_{y_2}^2 = E\left\{ \int_0^T x(t_1)(T-t_1)dt_1 \int_0^T x(t_2)(T-t_2)dt_2 \right\}, \tag{B40}$$

which becomes

$$\sigma_{y_2}^2 = \int_0^T \int_0^T (T-t_1)(T-t_2)R(t_1,t_2)dt_1 dt_2 \,. \tag{B41}$$

This can be expanded to

$$\sigma_{y_2}^2 = \int_0^T \int_0^T (T-t_1)(T-t_2)\frac{N_0}{2}\delta(t_1-t_2)dt_1 dt_2 \,. \tag{B42}$$

Performing the integrations yields

$$\sigma_{y_2}^2 = \int_0^T \frac{N_0}{2}(T-t_2)^2 dt_2 = \frac{N_0}{2}\left(\frac{T^3}{3}\right). \tag{B43}$$

This also corresponds exactly with the earlier result using sampled data.

<u>Continuous-Time Third Order Random Walk</u>

We calculate the Third Order Random Walk as

$$y_3(T) = \int_0^T \left(\int_0^{\tau_2} \left(\int_0^{\tau_1} x(t)dt \right) d\tau_1 \right) d\tau_2 \,. \tag{B44}$$

This also needs to eventually be written as a single integration over *t*, which again necessitates changing the order of integration. Consequently, we do this with appropriate changes in integration limits and ultimately get

$$y_3(T) = \int_0^T x(t)\frac{(T-t)^2}{2}dt \,. \tag{B45}$$

The output variance is calculated as

$$\sigma_{y_3}^2 = E\left\{\int_0^T x(t_1)\frac{(T-t_1)^2}{2}dt_1 \int_0^T x(t_2)\frac{(T-t_2)^2}{2}dt_2\right\}, \tag{B46}$$

which becomes

$$\sigma_{y_3}^2 = \int_0^T\int_0^T \frac{(T-t_1)^2(T-t_2)^2}{4} R(t_1,t_2)dt_1dt_2 . \tag{B47}$$

This can be expanded to

$$\sigma_{y_3}^2 = \int_0^T\int_0^T \frac{(T-t_1)^2(T-t_2)^2}{4} \frac{N_0}{2}\delta(t_1-t_2)dt_1dt_2 . \tag{B48}$$

Performing the integrations yields

$$\sigma_{y_3}^2 = \int_0^T \frac{N_0}{2}\frac{(T-t_2)^4}{4}dt_2 = \frac{N_0}{2}\left(\frac{T^5}{20}\right). \tag{B49}$$

This also corresponds exactly with the earlier result using sampled data.

<u>Continuous-Time Fourth Order Random Walk</u>

We calculate the Fourth Order Random Walk as

$$y_4(T) = \int_0^T\left(\int_0^{\tau_3}\left(\int_0^{\tau_2}\left(\int_0^{\tau_1} x(t)dt\right)d\tau_1\right)d\tau_2\right)d\tau_3 . \tag{B50}$$

This also needs to eventually be written as a single integration over *t*, which again necessitates changing the order of integration. Consequently, we do this with appropriate changes in integration limits and ultimately get

$$y_4(T) = \int_0^T x(t)\frac{(T-t)^3}{6}dt . \tag{B51}$$

The output variance is calculated as

$$\sigma_{y_4}^2 = E\left\{\int_0^T x(t_1)\frac{(T-t_1)^3}{6}dt_1 \int_0^T x(t_2)\frac{(T-t_2)^3}{6}dt_2\right\}, \tag{B52}$$

which becomes

$$\sigma_{y_4}^2 = \int_0^T\int_0^T \frac{(T-t_1)^3(T-t_2)^3}{36} R(t_1,t_2)dt_1dt_2 \,. \tag{B53}$$

This can be expanded to

$$\sigma_{y_4}^2 = \int_0^T\int_0^T \frac{(T-t_1)^3(T-t_2)^3}{36}\frac{N_0}{2}\delta(t_1-t_2)dt_1dt_2 \,. \tag{B54}$$

Performing the integrations yields

$$\sigma_{y_4}^2 = \int_0^T \frac{N_0}{2}\frac{(T-t_2)^6}{36}dt_2 = \frac{N_0}{2}\left(\frac{T^7}{252}\right). \tag{B55}$$

This also corresponds exactly with the earlier result using sampled data.

<u>Continuous-Time General Order Random Walk</u>

We calculate the K^{th} Order Random Walk as

$$y_K(T) = \int_0^T x(t)\left[\frac{(T-t)^{(K-1)}}{(K-1)!}\right]dt \,. \tag{B56}$$

The quantity in the square brackets describes a measure of the enclosed space of a $(K-1)$ dimensional hypertetrahedron. For example, for a 2-D hypertetrahedron the measure is an area of a triangle, and for a 3-D hypertetrahedron the measure is a volume of a tetrahedron. The general hypertetrahedron is formed from a hypercube with edges of length $(T-t)$, where the hypertetrahedron contains one apex vertex and all other adjacent vertices which are a distance $(T-t)$ away. Examples are shown in Figure 22. Note that all 2-D projections are triangles, and all triangles have the same apex.

The output variance is calculated as

$$\sigma_{y_K}^2 = E\left\{\int_0^T x(t_1)\frac{(T-t_1)^{(K-1)}}{(K-1)!}dt_1 \int_0^T x(t_2)\frac{(T-t_2)^{(K-1)}}{(K-1)!}dt_2\right\}, \tag{B57}$$

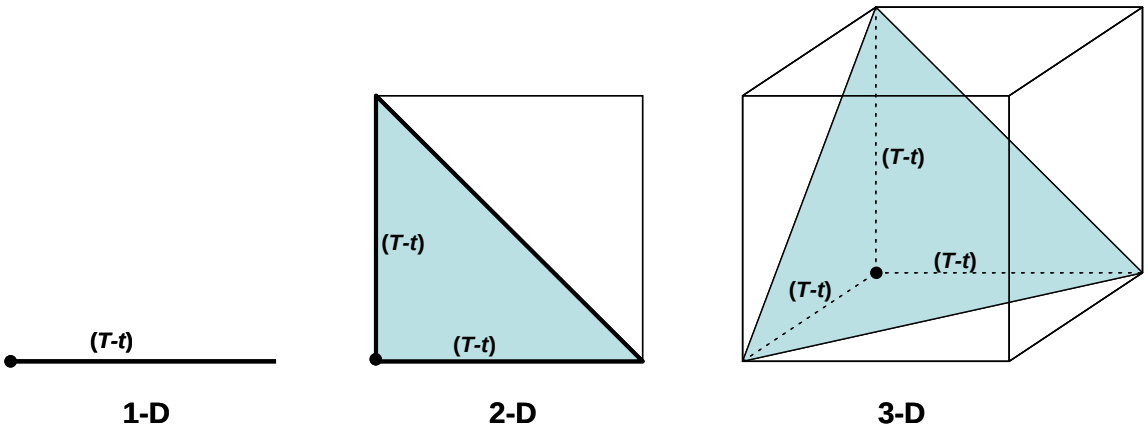

Figure 22. Hypertetrahedrons formed from vertices of hypercubes.

which becomes

$$\sigma_{y_K}^2 = \int_0^T \int_0^T \frac{(T-t_1)^{(K-1)}(T-t_2)^{(K-1)}}{((K-1)!)^2} R(t_1,t_2)dt_1 dt_2 \,. \tag{B58}$$

This can be expanded to

$$\sigma_{y_K}^2 = \int_0^T \int_0^T \frac{(T-t_1)^{(K-1)}(T-t_2)^{(K-1)}}{((K-1)!)^2} \frac{N_0}{2}\delta(t_1-t_2)dt_1 dt_2 \,. \tag{B59}$$

Performing the integrations yields

$$\sigma_{y_K}^2 = \int_0^T \frac{N_0}{2} \frac{(T-t_2)^{2(K-1)}}{((K-1)!)^2} dt_2 = \frac{N_0}{2}\left(\frac{T^{(2K-1)}}{(2K-1)((K-1)!)^2} \right). \tag{B60}$$

A Special Note

The expression for variance

$$\sigma_{y_K}^2 = \int_0^T \int_0^T \frac{(T-t_1)^{(K-1)}(T-t_2)^{(K-1)}}{((K-1)!)^2} R(t_1,t_2)dt_1 dt_2 \,, \tag{B61}$$

does not yet presume any particular noise autocorrelation function, and hence is applicable to noise with other than 'white' characteristics.

“Do what you can, with what you have, where you are. “
-- Theodore Roosevelt

Appendix C – 1/f Noise

1/*f* noise is also known as 'flicker' noise, or 'pink' noise. This specifically refers to noise with a Power Spectral Density (PSD) with a form

$$S(f) = \frac{C}{|2\pi f|^{\alpha}}. \tag{C1}$$

where

C = some constant, and
α = a constant most often where $0 < \alpha < 2$. (C2)

The usual case, and the case of interest to this report, is when $\alpha = 1$. Henceforth we will concern ourselves with

$$S(f) = \frac{C}{|2\pi f|}. \tag{C3}$$

Noise with this characteristic was first identified in 1925, and random behavior with this characteristic is found widely in nature. This characteristic represents behavior somewhere in between that of white noise ($\alpha = 0$), and a first-order random walk ($\alpha = 2$). As a consequence, it cannot be generated generally by integrating white noise, as can random walks. However, it is possible to get this behavior over limited bandwidths by appropriately filtering white noise.

The autocorrelation function is directly calculated to be

$$R(t) = -\frac{C\left(\gamma + \mathrm{Ln}\left(|t|\right)\right)}{\pi}, \tag{C4}$$

where

γ = Euler's Constant Gamma, $\gamma \approx 0.5772$. (C5)

Note that $R(t)$ is infinite at $t = 0$. It is somewhat disconcerting that $R(t)$ grows increasingly negative as $|t|$ gets very large.

Unlike random walks, it is not possible to generate flicker noise by integrating white noise. However, Barnes and Allen[51] have shown how to generate flicker noise from white noise using the method of fractional order of integration.

Approximations to PSD

For our purposes, we only need the 1/*f* characteristic over some finite bandwidth, and for some finite time. To generate a suitable approximation of this we construct a random process by filtering and adding a number of uncorrelated white noise processes.

$$n(t) = \sum_{k-1}^{K} h_k(t) * n_k(t), \tag{C6}$$

where

$h_k(t)$ = independent filters' impulse response, and
$n_k(t)$ = independent WGN sources. (C7)

The filters have transfer functions that are the Fourier Transforms of their respective impulse responses, namely

$$h_k(t) \Leftrightarrow H_k(f). \tag{C8}$$

We stipulate that each noise source $n_k(t)$ has an equivalent white PSD, that is

$$S_0(f) = \frac{N_0}{2}. \tag{C9}$$

The output PSD is then the input PSD modified by the sum of the various filters, that is

$$S(f) = S_0(f) \sum_{k=1}^{K} \left| H_k(f) \right|^2. \tag{C10}$$

Our design criteria is that we desire

$$S(f) \approx \frac{B^2}{2\pi |f|} \quad \text{for} \quad f_1 \le |f| \le f_2. \tag{C11}$$

We assume f_1 and f_2 are positive and furthermore greater than zero. Reasonable frequency limits for the band of interest are from something less than (observation time)$^{-1}$ up to the sampling frequency. Outside this band of interest, we will accept anything less than the 1/*f* characteristic. For example, for $|f| < f_1$ a constant value would suffice, and for $|f| > f_2$ we will accept zero, or perhaps a 1/f^2 characteristic.

In general, we desire $H_k(f)$ to be a low-pass filter where

$$\left|H_k(f)\right|^2 = C_0^2 \left(\frac{f_{\text{ref}}}{f_{c,k}}\right) W\left(\frac{f}{f_{c,k}}\right), \tag{C12}$$

where

$f_{c,k}$ = the corner frequency of the k^{th} filter,
f_{ref} = specific reference frequency for which gain is desired
C_0^2 = constant gain factor, and
$W(f)$ = filter function template. (C13)

We require $W(f)$ to be a low-pass function with unity DC gain, and unity corner frequency. Departures from this will be handled via frequency and amplitude scaling. Consequently, the approximated PSD is given by

$$S(f) = \frac{N_0}{2} C_0^2 \sum_{k=1}^{K} \left(\frac{f_{\text{ref}}}{f_{c,k}}\right) W\left(\frac{f}{f_{c,k}}\right). \tag{C14}$$

Note that we require the reference frequency to be within the range of interest,

$$f_1 \le f_{\text{ref}} \le f_2 \tag{C15}$$

and we desire proper scaling of the approximation, namely

$$S(f_{\text{ref}}) = \frac{N_0}{2} C_0^2 \sum_{k=1}^{K} \left(\frac{f_{\text{ref}}}{f_{c,k}}\right) W\left(\frac{f_{\text{ref}}}{f_{c,k}}\right) = \frac{B^2}{2\pi f_{\text{ref}}}. \tag{C16}$$

This implies that the constant gain factor can be calculated as

$$C_0^2 = \frac{B^2}{2\pi f_{\text{ref}} \left(\frac{N_0}{2}\right) \sum_{k=1}^{K} \left(\frac{f_{\text{ref}}}{f_{c,k}}\right) W\left(\frac{f_{\text{ref}}}{f_{c,k}}\right)}. \tag{C17}$$

We will assume a logarithmic distribution for $f_{c,k}$ as a matter of convenience. We consequently define

$$f_{c,k} = f_1 f_\Delta{}^{k-1}, \tag{C18}$$

where the corner frequency increment factor is calculated to be

$$f_\Delta = \left(\frac{f_2}{f_1} \right)^{\frac{1}{K-1}}. \tag{C19}$$

This implies that the individual corner frequencies can be found by

$$f_{c,k} = f_1 \left(\frac{f_2}{f_1} \right)^{\frac{k-1}{K-1}}. \tag{C20}$$

The choice of filter template $W(f)$ allows some latitude. For example, any of the following may find some utility.

$$W(f) = \frac{1}{1+(f)^2}, \tag{C21}$$

$$W(f) = \text{rect}\left(\frac{f}{2} \right), \tag{C22}$$

$$W(f) = \text{sinc}^2\left(\frac{f}{2} \right), \text{ or} \tag{C23}$$

$$W(f) = \text{sinc}\left(\frac{f}{2} \right), \tag{C24}$$

where

$$\text{rect}(z) = \begin{cases} 1 & |z| \le 1/2 \\ 0 & else \end{cases}, \text{ and} \tag{C25}$$

$$\text{sinc}(z) = \frac{\sin(\pi z)}{\pi z}. \tag{C26}$$

One might develop some angst in the fact that $W(f)$ in some cases may contain negative values. However, the requirement is in fact for $S(f) \ge 0$ for the frequency ranges of interest, and not necessarily for each component member. Whether or not the individual filters are realizable is not material to this analysis.

The autocorrelation function for the accumulated PSDs is given by the accumulation of Fourier Transforms of the individual components of the PSD. That is

$$R(t_1,t_2)=\sum_{k=1}^{K}R_k(t_1-t_2), \tag{C27}$$

where the autocorrelation component functions have Fourier Transform

$$R_k(t)\Leftrightarrow\frac{N_0}{2}C_0^2\left(\frac{f_{\text{ref}}}{f_{c,k}}\right)W\left(\frac{f}{f_{c,k}}\right). \tag{C28}$$

Consequently, we identify the component autocorrelation functions as

$$R_k(t)=\frac{N_0}{2}C_0^2 f_{\text{ref}}\,w\left(f_{c,k}t\right), \tag{C29}$$

where we identify the Fourier Transform pair

$$w(t)\Leftrightarrow W(f). \tag{C30}$$

Putting these together yields the composite autocorrelation function

$$R(t_1,t_2)=\frac{N_0}{2}C_0^2 f_{\text{ref}}\sum_{k=1}^{K}w\left(f_{c,k}(t_1-t_2)\right) \tag{C31}$$

PSD Approximation Example

We now examine the PSD based on a specific model. For the case

$$W(f)=\frac{1}{1+(f)^2}, \tag{C32}$$

we identify the k^{th} noise component filter as

$$H_k(f)=\frac{C_0\sqrt{f_{\text{ref}}/f_{c,k}}}{1+j\dfrac{f}{f_{c,k}}}. \tag{C33}$$

The filter's impulse response is in fact

$$h_k(t)=C_0\sqrt{\frac{f_{\text{ref}}}{f_{c,k}}}\left(2\pi f_{c,k}\right)e^{-2\pi f_{c,k}t}U(t), \tag{C34}$$

where we employ the unit step function

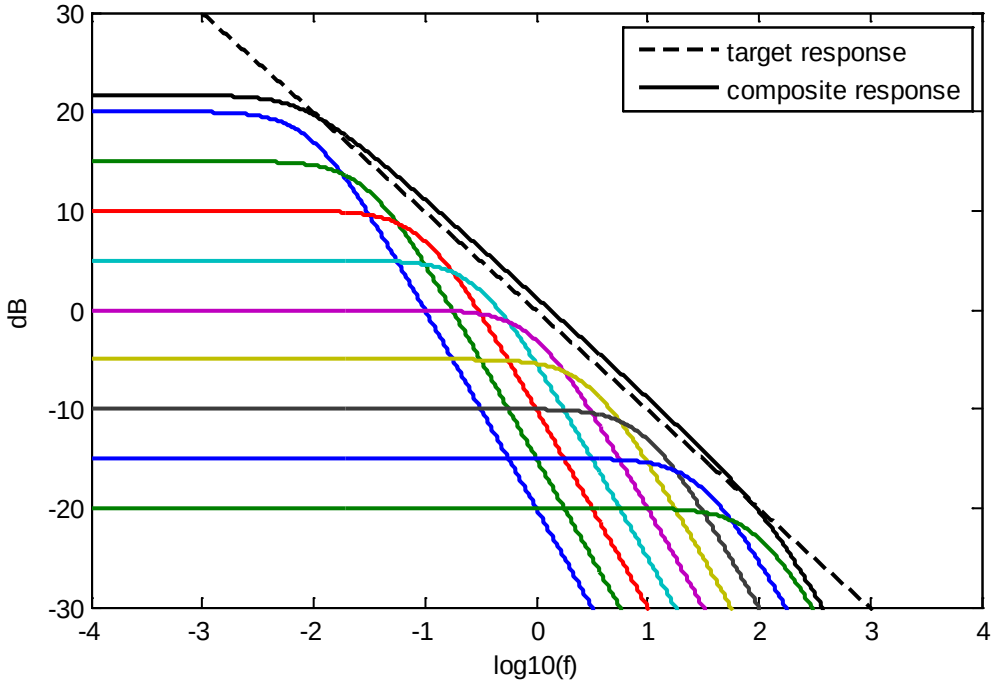

Figure 23. PSD of approximation to 1/f noise. In this example, $K = 9$**, and** $f_\Delta = \sqrt{10}$**.**

$$U(t) = \begin{cases} 1 & t \geq 0 \\ 0 & else \end{cases}. \tag{C35}$$

Figure 23 illustrates an example where several noise sources each with unit PSD distributed between 0.01 Hz and 100 Hz are added to form a composite random process with 1/*f* roll-off between these limits, and normalized to unit PSD at *f* = 1 Hz.

Note that this approximation can be made arbitrarily accurate by choosing an appropriate number and spacing of the corner frequencies. Note also that each filter dominates some region of frequency nearest to its corner frequency.

Clearly, at this point we have a way to filter white noise to achieve an arbitrarily accurate approximation to 1/*f* noise over whatever bandwidth we may choose. Furthermore, the filters are linear, and in fact realizable. We could build this if needed.

The autocorrelation function is then simply the Inverse Fourier Transform of the composite PSD, namely

$$R(t_1, t_2) = \frac{N_0}{2} C_0^2 f_{\text{ref}} \sum_{k=1}^{K} \pi e^{-2\pi f_1 f_\Delta{}^{k-1} |t_1 - t_2|}. \tag{C36}$$

For this example, we note that the scale factors ahead of the summation equate to

$$\frac{N_0}{2}C_0^2 f_{\text{ref}} = \frac{B^2}{\left(2\pi f_{\text{ref}}\right)\sum_{k=1}^{K}\left(\frac{1}{f_{c,k}}\right)W\left(\frac{f_{\text{ref}}}{f_{c,k}}\right)}. \tag{C37}$$

With respect to the summation, if the corner frequencies are not too bunched together, then we can approximate the summation with the contribution from the dominant filter. Consequently, the summation at the reference frequency can be approximated as

$$\sum_{k=1}^{K}\left(\frac{1}{f_{c,k}}\right)W\left(\frac{f_{\text{ref}}}{f_{c,k}}\right) \approx \left(\frac{1}{f_{\text{ref}}}\right). \tag{C38}$$

This allows the approximation

$$\frac{N_0}{2}C_0^2 f_{\text{ref}} = \frac{B^2}{2\pi}. \tag{C39}$$

The autocorrelation function for this model can then be simplified somewhat to

$$R\left(t_1,t_2\right) = \left(\frac{B^2}{2}\right)\sum_{k=1}^{K} e^{-2\pi\frac{f_1}{f_\Delta}\left|t_1-t_2\right|f_\Delta{}^k}. \tag{C40}$$

Note that this autocorrelation function is always positive. However, its behavior is difficult to discern because we have no closed form solution to the summation.

<u>Autocorrelation of PSD Approximation</u>

To analyze the behavior of the autocorrelation function with time, we use a slightly different model where now

$$W\left(f\right) = \text{sinc}\left(\frac{f}{2}\right). \tag{C41}$$

For this function, the Inverse Fourier Transform is identified via the transform pair

$$\text{sinc}\left(\frac{f}{2}\right) \Leftrightarrow 2\,\text{rect}\left(2t\right). \tag{C42}$$

Consequently, the autocorrelation function is identified by

$$R(t_1,t_2)=\frac{N_0}{2}C_0^2 f_{\text{ref}}\,2\sum_{k=1}^{K}\text{rect}\left(2\frac{f_1}{f_\Delta}\,{f_\Delta}^k(t_1-t_2)\right). \tag{C43}$$

Observe that the summation is of a series of rect() functions of different widths. The summation can be rewritten as

$$R(t_1,t_2)=\frac{N_0}{2}C_0^2 f_{\text{ref}}\,2\sum_{k=1}^{K}\text{rect}\left(\frac{(t_1-t_2)}{2\left(\frac{f_\Delta}{4f_1}\right)\left({\tau_\Delta}^k\right)}\right), \tag{C44}$$

where

$$\tau_\Delta = 1/f_\Delta\,. \tag{C45}$$

Since $f_\Delta > 1$, then $\tau_\Delta < 1$. Consequently, as *k* increases, the rect() functions get narrower. The widest rect() function is for $k=1$. This yields the observation for this model that $R(t_1,t_2)$ has a finite span, namely

$$R(t_1,t_2)=0 \quad \text{for } |t_1-t_2|>\frac{1}{4f_1}. \tag{C46}$$

As $|t_1-t_2|$ decreases from $(4f_1)^{-1}$, the rect() functions begin stacking up. In fact,

$$\sum_{k=1}^{K}\text{rect}\left(\frac{(t_1-t_2)}{2\left(\frac{f_\Delta}{4f_1}\right)\left({\tau_\Delta}^k\right)}\right)=k \quad \text{for } |t_1-t_2|=\left(\frac{f_\Delta}{4f_1}\right)\left({\tau_\Delta}^k\right). \tag{C47}$$

Solving the condition for *k* sets up the equation that evaluates the summation as

$$\sum_{k=1}^{K}\text{rect}\left(\frac{(t_1-t_2)}{2\left(\frac{f_\Delta}{4f_1}\right)\left({\tau_\Delta}^k\right)}\right)=\frac{\ln\left(|t_1-t_2|\right)-\ln\left(\frac{f_\Delta}{4f_1}\right)}{\ln\tau_\Delta} \quad \text{for } |t_1-t_2|\le\frac{1}{4f_1}. \tag{C48}$$

While this is only strictly true for very specific values of $|t_1-t_2|$, this is adequate to observe the behavior of which we are interested. Thus, we identify the autocorrelation function as

$$R(t_1,t_2)=\begin{cases}\dfrac{N_0}{2}C_0^2 f_{\text{ref}}\,2\left(\ln\left(|t_1-t_2|\right)-\ln\left(\dfrac{f_\Delta}{4f_1}\right)\right)\Big/\ln\tau_\Delta & |t_1-t_2|\le\dfrac{1}{4f_1}\\ 0 & |t_1-t_2|>\dfrac{1}{4f_1}\end{cases}. \quad \text{(C49)}$$

Some additional algebra yields

$$R(t_1,t_2)=\begin{cases}\dfrac{N_0}{2}C_0^2 f_{\text{ref}}\,2\left(\ln\left(\dfrac{f_\Delta}{4f_1}\right)-\ln\left(|t_1-t_2|\right)\right)\Big/\ln f_\Delta & |t_1-t_2|\le\dfrac{1}{4f_1}\\ 0 & |t_1-t_2|>\dfrac{1}{4f_1}\end{cases}. \quad \text{(C50)}$$

We note two important characteristics here

- $R(t_1,t_2)$ is non-negative.
- $R(t_1,t_2)$ decreases with a logarithmic dependence on $|t_1-t_2|$.

<u>First-Order Integration of 1/f Noise</u>

From the previous Appendix, we recall that the variance after arbitrary orders of integration can be calculated as

$$\sigma_{y_K}^2=\int_0^T\int_0^T\frac{(T-t_1)^{(K-1)}(T-t_2)^{(K-1)}}{\left((K-1)!\right)^2}R(t_1,t_2)dt_1dt_2\,. \quad \text{(C51)}$$

To investigate integration of 1/*f* noise we will return to the model where

$$W(f)=\frac{1}{1+(f)^2}, \quad \text{(C52)}$$

and recall that

$$R(t_1,t_2)=\left(\frac{B^2}{2}\right)\sum_{k=1}^{K}e^{-2\pi\frac{f_1}{f_\Delta}|t_1-t_2|f_\Delta{}^k}\,. \quad \text{(C53)}$$

We are interested in integrating the noise over time period *T*, where we limit *T* such that

$$f_1<<1/T<<f_2\,. \quad \text{(C54)}$$

For one level of integration over time period *T* we calculate the output variance as

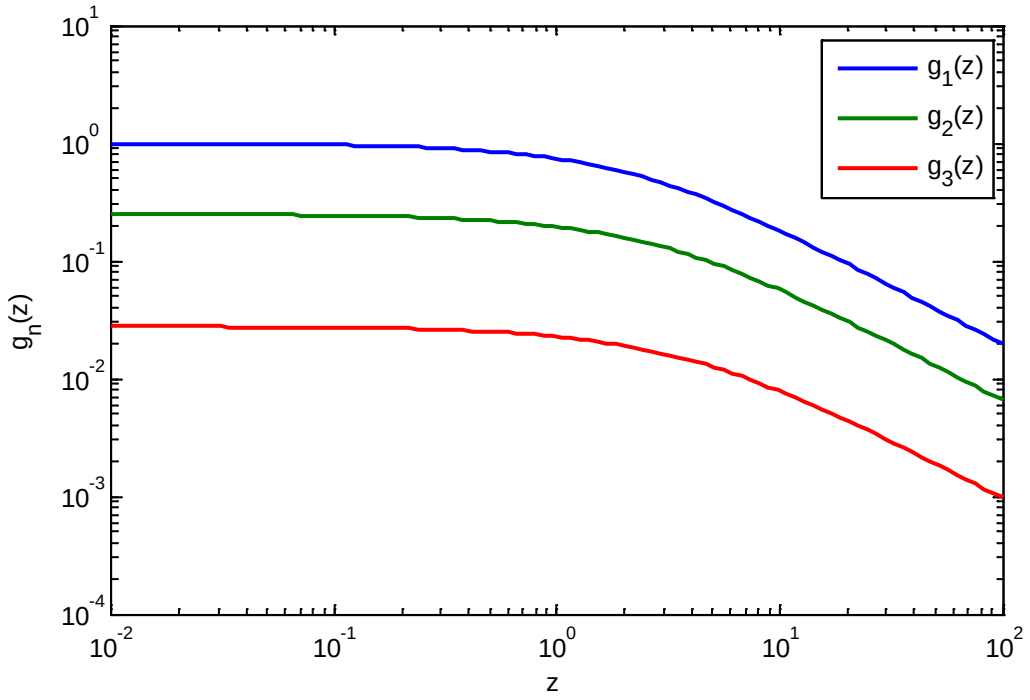

Figure 24. Plots of various $g_n(x)$.

$$\sigma_{y_1}^2 = \left(\frac{B^2}{2}\right) T^2 \sum_{k=1}^{K} 2\left(\frac{e^{-a_k T} - (1 - a_k T)}{(a_k T)^2}\right), \tag{C55}$$

where

$$a_k = 2\pi\left(f_1 / f_\Delta\right) {f_\Delta}^k = 2\pi f_1 {f_\Delta}^{k-1}. \tag{C56}$$

Let us now examine the behavior of the function

$$g_1(z) = 2\left(\frac{e^{-z} - (1 - z)}{z^2}\right). \tag{C57}$$

This is plotted in Figure 24. Note that this has a 'low-pass' behavior with respect to z. We note the following asymptotic behaviors

$$\begin{aligned} &g_1(z << 1) \approx 1, \text{ and} \\ &g_1(z >> 1) \approx 2/z. \end{aligned} \tag{C58}$$

This implies a corner frequency at $z = 2$, and lets us proceed with the approximation

$$g_1(z) \approx \text{rect}\left(z/4\right). \tag{C59}$$

The calculation for variance can then be transmogrified to

$$\sigma_{y_1}^2 = \left(\frac{B^2}{2}\right) T^2 \sum_{k=1}^{K} \text{rect}\left(\frac{2\pi\left(f_1/f_\Delta\right) {f_\Delta}^k T}{4}\right). \tag{C60}$$

As with the autocorrelation calculation, this describes a set of stacked rect() functions of progressively narrower widths. In particular

$$\sum_{k=1}^{K} \text{rect}\left(\frac{2\pi\left(f_1/f_\Delta\right) {f_\Delta}^k T}{4}\right) = k \quad \text{for} \left(\frac{2\pi\left(f_1/f_\Delta\right) {f_\Delta}^k T}{4}\right) = \frac{1}{2}. \tag{C61}$$

This can be rewritten as

$$\sum_{k=1}^{K} \text{rect}\left(\frac{2\pi\left(f_1/f_\Delta\right) {f_\Delta}^k T}{4}\right) = \left(1 - \frac{\ln\left(\pi f_1 T\right)}{\ln f_\Delta}\right). \tag{C62}$$

Consequently, the variance can be written as

$$\sigma_{y_1}^2 = \left(\frac{B^2}{2}\right) T^2 \left(1 - \frac{\ln\left(\pi f_1 T\right)}{\ln f_\Delta}\right). \tag{C63}$$

A further examination of the quantity $\left(1 - \ln\left(\pi f_1 T\right)/\ln f_\Delta\right)$ for some likely parameters yields the following exemplar behavior. For long time durations,

$$\left(1 - \frac{\ln\left(\pi f_1 T\right)}{\ln f_\Delta}\right) = 1 \quad \text{for } T = \frac{1}{\pi f_1} \tag{C64}$$

For T equal to 1/10 this value, and for $f_\Delta = \sqrt{10}$,

$$\left(1 - \frac{\ln\left(\pi f_1 T\right)}{\ln f_\Delta}\right) = 3 \quad \text{for } T = \frac{1}{10\pi f_1}. \tag{C65}$$

This factor is dwarfed by the T^2 dependence of $\sigma_{y_1}^2$. Consequently, we can arguably approximate the variance as

$$\sigma_{y_1}^2 \approx \left(\frac{B^2}{2}\right) T^2. \tag{C66}$$

Second-Order Integration of 1/f Noise

For two levels of integration over time period *T* we calculate the output variance as

$$\sigma_{y_2}^2 = \left(\frac{B^2}{2}\right) T^4 \sum_{k=1}^{K} \left(\frac{\left(6 - 3(a_k T)^2 + 2(a_k T)^3 - (6 + 6a_k T) e^{-a_k T}\right)}{3(a_k T)^4} \right). \tag{C67}$$

Let us now examine the behavior of the function

$$g_2(z) = \left(\frac{6 - 3z^2 + 2z^3 - (6 + 6z) e^{-z}}{3z^4} \right). \tag{C68}$$

Note in Figure 24 that this also has a 'low-pass' behavior with respect to *z*, with the following asymptotic behaviors

$$g_2(z << 1) \approx 1/4 \text{, and}$$
$$g_2(z >> 1) \approx 2/(3z). \tag{C69}$$

This implies a corner frequency at $z = 8/3$ and lets us proceed with the approximation

$$g_2(z) \approx \frac{1}{4} \text{rect}\left(\frac{z}{16/3} \right). \tag{C70}$$

The calculation for variance can then be transmogrified to

$$\sigma_{y_2}^2 = \left(\frac{B^2}{2}\right) T^4 \frac{1}{4} \sum_{k=1}^{K} \text{rect}\left(\frac{2\pi (f_1 / f_\Delta) {f_\Delta}^k T}{16/3} \right). \tag{C71}$$

As with the autocorrelation calculation, this describes a set of stacked rect() functions of progressively narrower widths. In particular

$$\sum_{k=1}^{K} \text{rect}\left(\frac{2\pi (f_1 / f_\Delta) {f_\Delta}^k T}{16/3} \right) = k \quad \text{for} \left(\frac{2\pi (f_1 / f_\Delta) {f_\Delta}^k T}{16/3} \right) = \frac{1}{2}. \tag{C72}$$

This can be rewritten as

$$\sum_{k=1}^{K} \text{rect}\left(\frac{2\pi (f_1 / f_\Delta) {f_\Delta}^k T}{16/3} \right) = \left(1 - \ln\left(\frac{2}{8/3} \pi f_1 T \right) \Big/ \ln f_\Delta \right). \tag{C73}$$

This expansion overtly shows the contribution of the $8/3$ corner frequency. Consequently, the variance can be written as

$$\sigma_{y_2}^2 = \left(\frac{B^2}{2}\right)\frac{T^4}{4}\left(1-\ln\left(\frac{3}{4}\pi f_1 T\right)\Big/\ln f_\Delta\right). \tag{C74}$$

Following the analysis of the single integration, this variance is dominated by the T^4 dependence. Consequently, we can arguably approximate the variance as

$$\sigma_{y_2}^2 \approx \left(\frac{B^2}{2}\right)\frac{T^4}{4}. \tag{C75}$$

<u>Third-Order Integration of 1/f Noise</u>

For three levels of integration over time period *T* we calculate the output variance as

$$\sigma_{y_3}^2 = \left(\frac{B^2}{2}\right)T^6\sum_{k=1}^{K}\left(\frac{\left(\begin{array}{l}-120+20\left(a_kT\right)^3-15\left(a_kT\right)^4+6\left(a_kT\right)^5\\+\left(120+120a_kT+60\left(a_kT\right)^2\right)e^{-a_kT}\end{array}\right)}{60\left(a_kT\right)^6}\right). \tag{C76}$$

Let us now examine the behavior of the function

$$g_3(z) = \left(\frac{-120+20z^3-15z^4+6z^5-\left(120+120z+60z^2\right)e^{-z}}{60z^6}\right). \tag{C77}$$

Note in Figure 24 that this also has a 'low-pass' behavior with respect to *z*, with the following asymptotic behaviors

$$\begin{aligned} &g_3(z<<1) \approx 1/36\text{, and}\\ &g_3(z>>1) \approx 1/(10z). \end{aligned} \tag{C78}$$

This implies a corner frequency at $z = 18/5$, and lets us proceed with the approximation

$$g_3(z) \approx \frac{1}{36}\text{rect}\left(\frac{z}{36/5}\right). \tag{C79}$$

The calculation for variance can then be transmogrified to

$$\sigma_{y_3}^2 = \left(\frac{B^2}{2}\right) T^6 \frac{1}{36} \sum_{k=1}^{K} \text{rect}\left(\frac{2\pi\left(f_1/f_\Delta\right) {f_\Delta}^k T}{36/5}\right). \tag{C80}$$

The summation can be rewritten as

$$\sum_{k=1}^{K} \text{rect}\left(\frac{2\pi\left(f_1/f_\Delta\right) {f_\Delta}^k T}{36/5}\right) = \left(1 - \ln\left(\frac{2}{18/5}\pi f_1 T\right) \Big/ \ln f_\Delta\right). \tag{C81}$$

Consequently, the variance can be written as

$$\sigma_{y_3}^2 = \left(\frac{B^2}{2}\right) \frac{T^6}{36} \left(1 - \ln\left(\frac{5}{9}\pi f_1 T\right) \Big/ \ln f_\Delta\right). \tag{C82}$$

Following the earlier analysis, this variance is dominated by the T^6 dependence. Consequently, we can arguably approximate the variance as

$$\sigma_{y_3}^2 \approx \left(\frac{B^2}{2}\right) \frac{T^6}{36}. \tag{C83}$$

<u>n^{th}-Order Integration of 1/f Noise</u>

We can extrapolate that for *n* levels of integration of flicker noise over time period *T* we calculate the output variance as predominantly

$$\sigma_{y_n}^2 \approx \left(\frac{B^2}{2}\right) \frac{T^{2n}}{(n!)^2}. \tag{C84}$$

Note that this result has a similarity with the results for random walks.

Appendix D – Phase Error Effects on Impulse Response

The net Impulse Response (IPR) of a SAR system is the ideal point reflector target response convolved with the impulse response of a filter exhibiting a phase function that is in fact the error. IPR is discussed in some detail in a prior report.[52] Consequently, without loss of generality, we can assume that the impulse response of a radar system with phase errors is the impulse response of the errors themselves constrained by the limits (duration or bandwidth) of the ideal signals. That is, the system IPR in some dimension (range or azimuth) is given in general by the Fourier Transform of the phase error factor

$$x(u) = \int_{-\infty}^{\infty} \text{rect}\left(\frac{t}{T}\right) e^{j\phi_\varepsilon(t)} e^{-j2\pi ut} dt \ , \tag{D1}$$

where

$$\text{rect}(z) = \begin{cases} 1 & z \le 1/2 \\ 0 & else \end{cases} \ ,$$

T = the duration of the input signal, and

$\phi_\varepsilon(t)$ = the phase error function. (D2)

If window functions are employed for sidelobe control, and they usually are, then this is modified to

$$x(u) = \int_{-\infty}^{\infty} w\left(\frac{t}{T}\right) \text{rect}\left(\frac{t}{T}\right) e^{j\phi_\varepsilon(t)} e^{-j2\pi ut} dt \tag{D3}$$

where

$w(z)$ = the window function, defined for $|z| \le 1/2$. (D4)

A common window function is the Taylor window.[53] It is also discussed in some detail by Doerry.[54]

Clearly, the nature of $\phi_\varepsilon(t)$ profoundly impacts the system IPR. Furthermore, the exact influence of $\phi_\varepsilon(t)$ on the IPR also depends on the window function $w(z)$. We now examine specific components, or characteristics of $\phi_\varepsilon(t)$.

Quadratic Phase Error

We now examine the case of a quadratic phase error, namely when

$$\phi_\varepsilon(t) = \phi_\varepsilon^q \left(\frac{2t}{T}\right)^2 \quad = \text{the phase error function,} \tag{D5}$$

where

$$\phi_\varepsilon^q \quad = \text{the peak quadratic phase error in the relevant interval } T. \tag{D6}$$

The IPR is then calculated by evaluating

$$x(u) = \int_{-\infty}^{\infty} w\left(\frac{t}{T}\right) \text{rect}\left(\frac{t}{T}\right) e^{j\phi_\varepsilon^q (2/T)^2 t^2} e^{-j2\pi ut} dt \ . \tag{D7}$$

A closed form solution is not possible, so we resort to numerical solutions. Figure 25 shows the IPR for various values of ϕ_ε^q. Note that the IPR gets progressively broader as ϕ_ε^q increases. The broadening of the –3 dB width is shown in Figure 26.

Cubic Phase Error

We now examine the case of a cubic phase error, namely when

$$\phi_\varepsilon(t) = \phi_\varepsilon^c \left(\frac{2t}{T}\right)^3 \quad = \text{the phase error function,} \tag{D8}$$

where

$$\phi_\varepsilon^c \quad = \text{the peak cubic phase error in the relevant interval } T. \tag{D9}$$

As with the quadratic phase error, we resort to numerical solutions. Figure 27 shows the IPR for various values of ϕ_ε^c. Note that the IPR gets slightly broader as ϕ_ε^c increases, but more significantly a problematic sidelobe emerges, and grows rather rapidly. There is also a subtle shift in the location of the mainlobe peak.

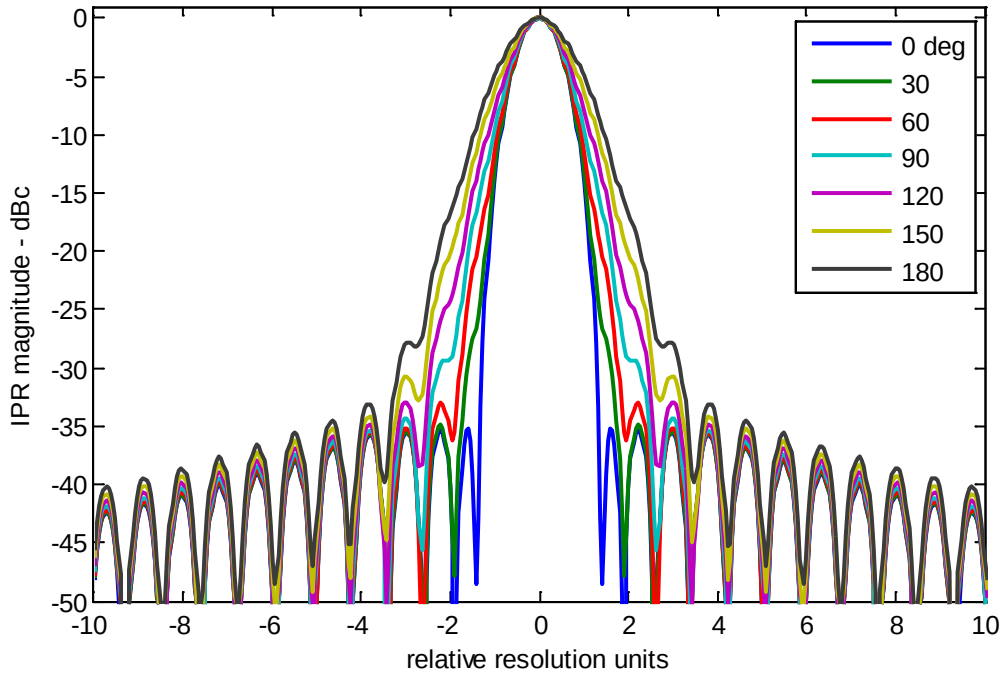

Figure 25. Close-up of IPR mainlobe for various amounts of peak quadratic phase error. Legend specifies peak quadratic phase error in degrees. Data was processed with a Taylor window (−35 dB sidelobes, nbar = 4).

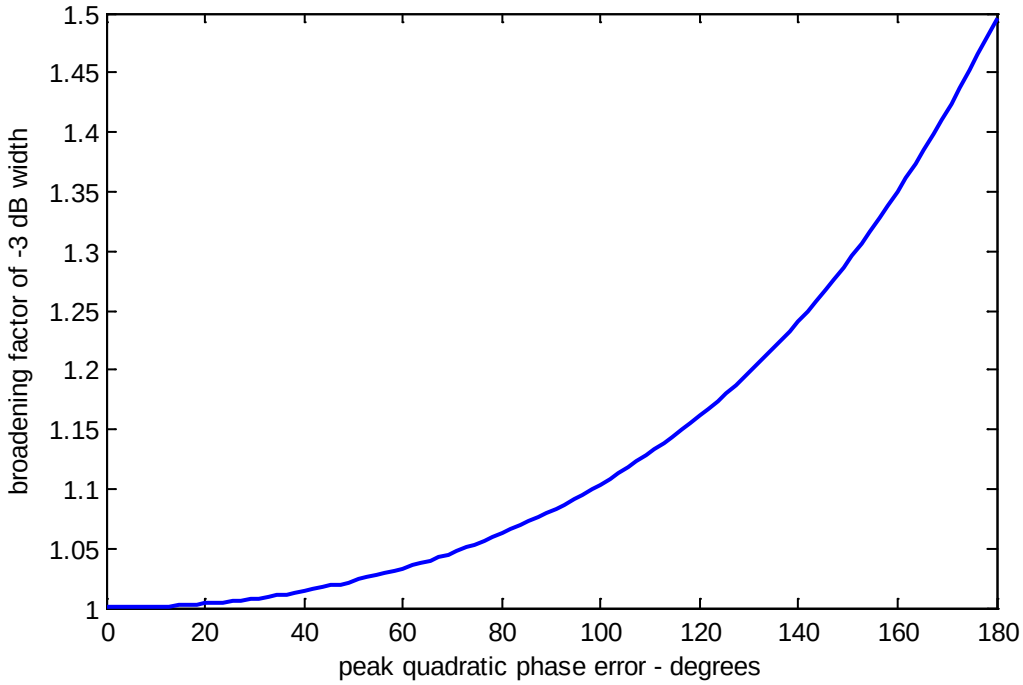

Figure 26. Broadening of IPR mainlobe due to quadratic phase error. Data was processed with a Taylor window (−35 dB sidelobes, nbar = 4).

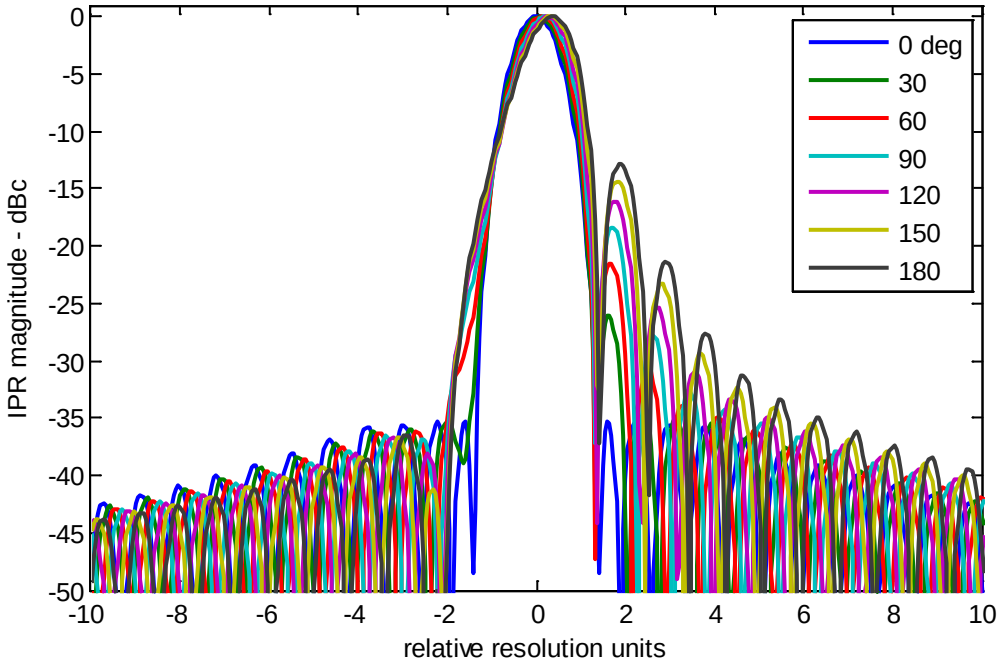

Figure 27. Close-up of IPR mainlobe for various amounts of peak cubic phase error. Legend specifies peak cubic phase error in degrees. Data was processed with a Taylor window (–35 dB sidelobes, nbar = 4).

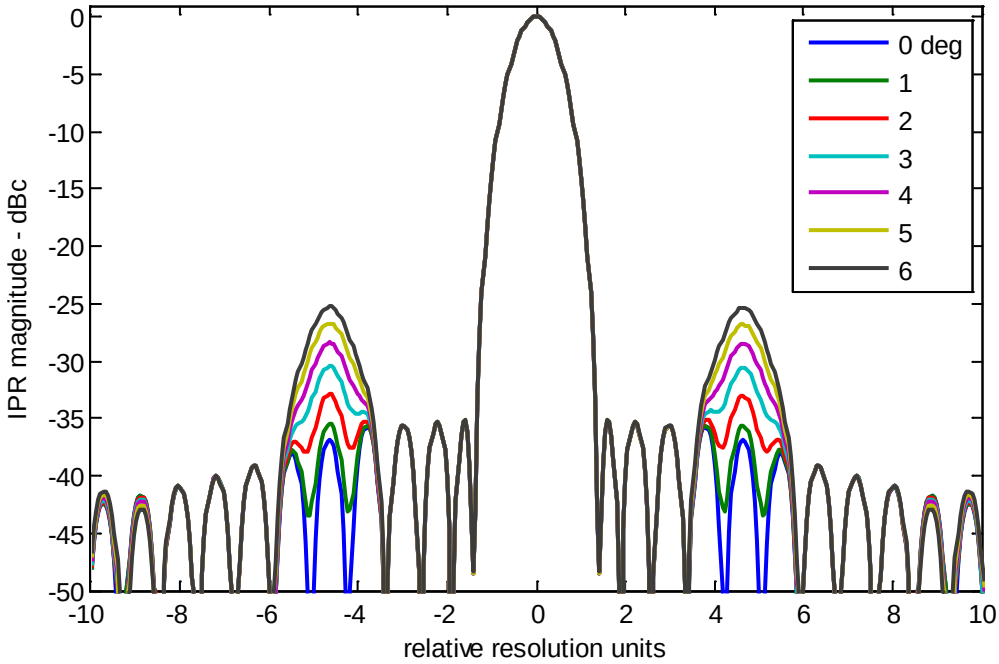

Figure 28. Close-up of IPR mainlobe for various amounts of peak sinusoidal phase error. Legend specifies peak sinusoidal phase error in degrees. Sinusoidal modulation represents 5.5 cycles per period. Data was processed with a Taylor window (–35 dB sidelobes, nbar = 4).

Sinusoidal Phase Error

We now examine the case of a sinusoidal phase error, namely when

$$\varphi_\varepsilon(t) = \varphi_\varepsilon^S \sin\left(\frac{2\pi f_m t}{T}\right) \quad = \text{the phase error function,} \tag{D10}$$

where

ϕ_ε^S = the peak sinusoidal phase error in the relevant interval *T*, and
f_m = the frequency of the sinusoidal phase modulation in cycles per period *T*. (D11)

The IPR is then calculated by evaluating

$$x(u) = \int_{-\infty}^{\infty} w\left(\frac{t}{T}\right)\text{rect}\left(\frac{t}{T}\right)e^{j\varphi_\varepsilon^S \sin\left(\frac{2\pi f_m t}{T}\right)}e^{-j2\pi ut}dt \ . \tag{D12}$$

We note that for small peak phase errors, we can approximate

$$e^{j\phi_\varepsilon^S \sin\left(\frac{2\pi f_m t}{T}\right)} \approx 1 + j\phi_\varepsilon^S \cos\left(\frac{2\pi f_m t}{T}\right). \tag{D13}$$

This allows us to readily identify the IPR as having a strong otherwise unaltered mainlobe, but with the addition of two sidelobes spaced on either side of the mainlobe a distance corresponding to $\pm f_m$ away from the mainlobe. Furthermore, the peak sidelobe level is readily calculated at a level

$$PSL = \phi_\varepsilon^S / 2, \tag{D14}$$

with respect to the mainlobe peak.

Figure 28 shows the IPR for various values of ϕ_ε^S and $f_m = 5.5$ cycles per period. Note that even low-single-digit degrees of peak phase error raise sidelobes substantially.

Random Phase Error

We now examine the case of a random phase error. We shall presume a zero-mean, band-limited Gaussian random process with standard deviation of ϕ_ε^r. The actual phase error modulation is given by

$$\phi_\varepsilon(t) = \phi_\varepsilon^r n(t) \text{ = the phase error function,} \tag{D15}$$

where

$$n(t) \text{ = zero-mean, unit-variance, band-limited Gaussian random process.} \tag{D16}$$

The process needs to be band-limited to keep the standard deviation finite.

As with the sinusoidal phase error, the phase transfer function can be approximated for small phase errors as

$$e^{j\phi_\varepsilon^r n(t)} \approx 1 + j\phi_\varepsilon^r n(t) \; . \tag{D17}$$

This is interpreted as equating a small phase noise to a small additive noise, thereby allowing easier analysis. Any signal with this random phase modulation will exhibit a Signal to Noise Ratio (SNR) of

$$SNR = \left(\phi_\varepsilon^r\right)^{-2} \; . \tag{D18}$$

Our interest is more in sampled data systems. In such a system, the input noise is band-limited to the sampling frequency, and the output of a Discrete Fourier Transform (DFT) will improve SNR by the number of data samples less some small amount due to the inefficiency of using a window function for sidelobe control. In this model, ϕ_ε^r is the standard deviation of the phase error in each of the samples. Furthermore, time period *T* represents some finite number of samples such that

$$T = M / f_s \; , \tag{D19}$$

where

$$\begin{aligned} f_s &= \text{the sampling frequency, and} \\ M &= \text{number of samples taken.} \end{aligned} \tag{D20}$$

The output of the DFT will exhibit a SNR gain to an improved SNR that represents a peak signal to an expected sidelobe level calculated as

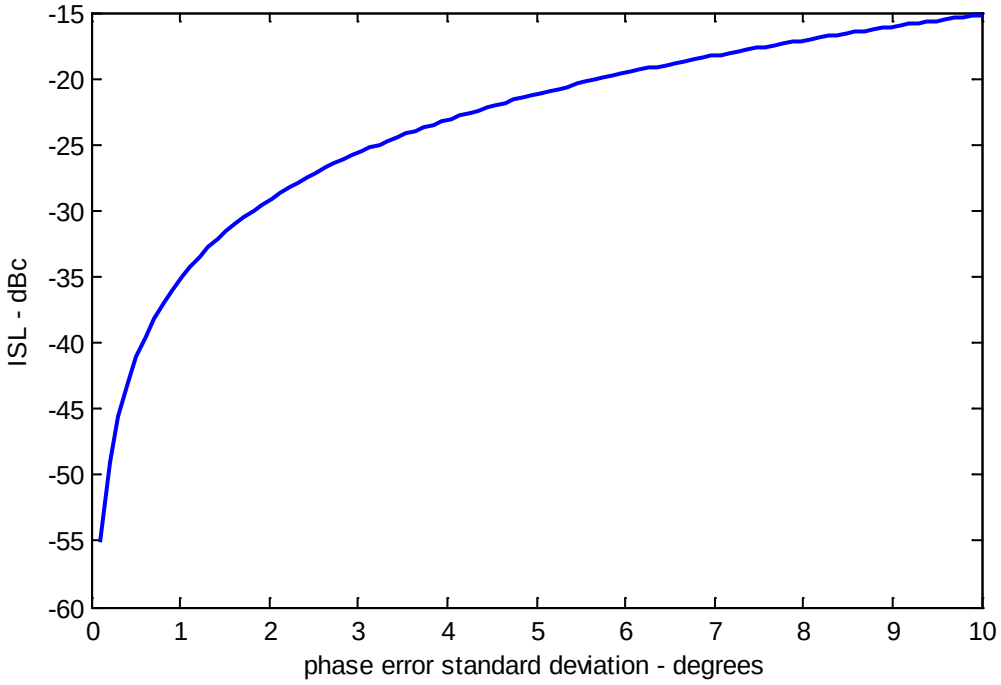

Figure 29. Integrated Sidelobe Level due to random phase errors.

$$SNR_{output} = \frac{M}{\left(\phi_{\varepsilon}^{r}\right)^{2}} \ . \tag{D21}$$

However, there will be noise energy at all possible sidelobe locations. The total energy in all sidelobes is captured in the Integrated Sidelobe Level (ISL), which is the inverse of the input SNR, or

$$ISL = \left(\phi_{\varepsilon}^{r}\right)^{2} \ . \tag{D22}$$

Note that ISL is really a relative power measurement, that is, relative to the power in the IPR mainlobe peak.

Figure 29 illustrates ISL as a function of random phase error standard deviation.

“We must find a way, or we will make one.”
-- Albert Einstein

Appendix E – SAR Azimuth Location Error with Constrained Linear Drift

Herein we estimate the SAR image cross-range (azimuth) target location error due to non-ideal motion measurement, albeit constrained in deviation from truth.

The navigator contributes to location error by two principal mechanisms:

1. The inherent position error of the radar, i.e. "own-ship position error," from which the relative measurements are made, and
2. The 'alignment' of the synthetic aperture, i.e. the relative position error from one pulse to the next; principally the linear component of the line-of-sight own-ship range error.

In this appendix we examine the second of these. We will treat this as a pointing error of the synthetic antenna.

Discussion

A typical navigation subsystem is comprised of a GPS-aided Inertial Navigation System (INS). The principal instrument in the INS is the Inertial Measurement Unit (IMU), itself typically comprised of three orthogonal accelerometers, and three orthogonal rate-gyros.

The IMU itself, due to measurement noise, will exhibit a drift in its velocity and position solution. The navigator will, however, generally constrain this drift, ultimately bounded by GPS measurement errors. Our simplified model for this analysis is then given in Figure 30.

With this model, we examine two cases

1. Aperture tilt bounded by GPS as in Figure 31, and
2. Aperture tilt bounded by IMU as in Figure 32.

We will limit our attention to the broadside imaging case (at least for now).

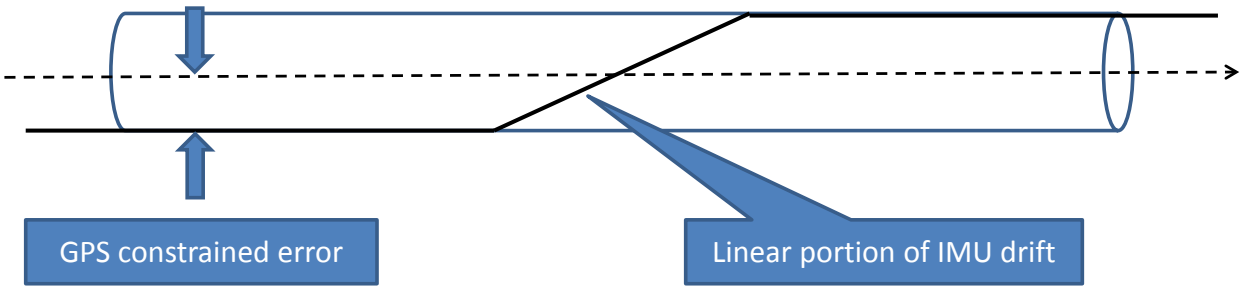

Figure 30. Simplified model for GPS-constrained navigator drift.

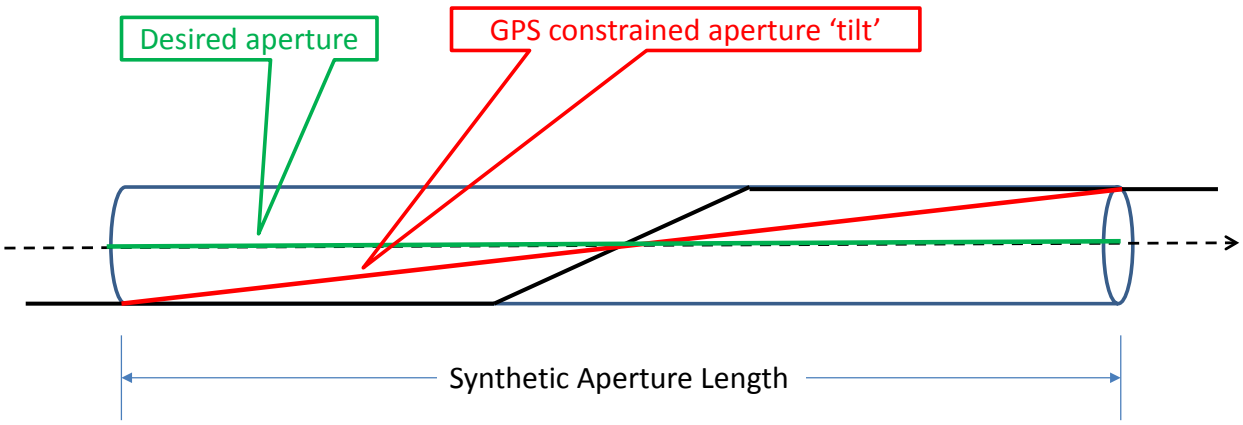

Figure 31. Aperture tilt bounded by GPS.

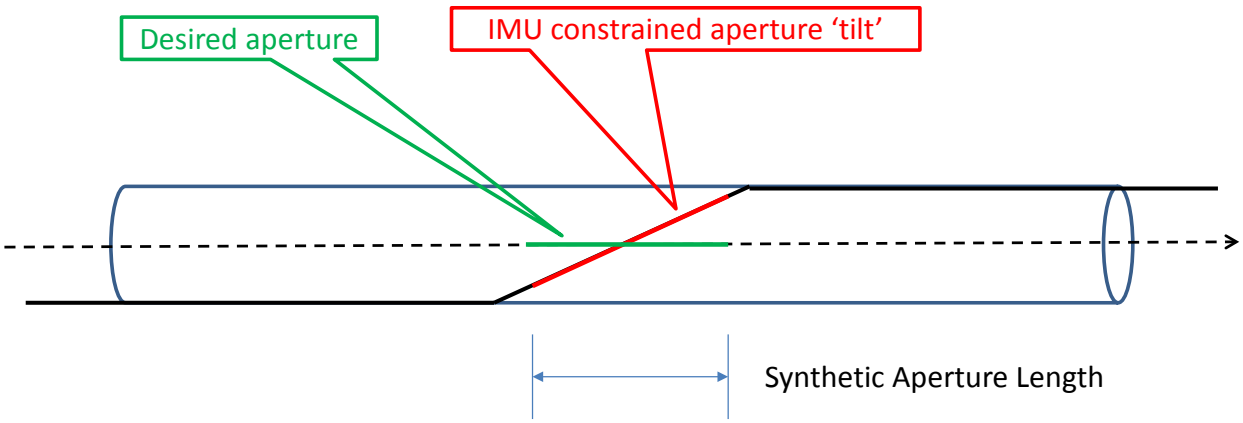

Figure 32. Aperture tilt bounded by IMU.

We define the tilt error two ways. In terms of position errors, the tilt error is calculated as the angle

$$\phi_{pos} = \text{atan}\left(\frac{2\varepsilon_{pos}}{L}\right) \approx \frac{2\varepsilon_{pos}}{L}\ , \tag{E1}$$

where

L = synthetic aperture length, and
ε_{pos} = the maximum radar position measurement error from nominal flight path.

(E2)

The synthetic aperture length is calculated via the familiar formula as

$$L = \frac{a_{wa}\lambda R}{2\rho_a}\ , \tag{E3}$$

where

λ = nominal radar wavelength,
R = nominal radar slant range,
ρ_a = nominal azimuth resolution, and
a_{wa} = azimuth window function IPR broadening factor. (E4)

Note also that aperture length is the product of radar platform velocity and aperture time, namely

$$L = v_a T_a \ , \tag{E5}$$

where

v_a = nominal radar forward velocity, and
T_a = synthetic aperture time interval. (E6)

A typical RMS position variation for a navigator might be 5 cm. Note that this is the relative error, and does not include any constant bias during the synthetic aperture.

In terms of velocity errors, the tilt error is calculated as the angle

$$\phi_{vel} = \text{atan}\left(\frac{\varepsilon_{vel}}{v_a} \right) \approx \frac{\varepsilon_{vel}}{v_a} \ , \tag{E7}$$

where

ε_{vel} = line-of-sight velocity error. (E8)

A typical RMS velocity error limit for a navigator might be 2 cm/s.

The two synthetic aperture tilt errors are equal when

$$\varepsilon_{vel} \, T_a = 2\varepsilon_{pos} \ . \tag{E9}$$

This also means that there is a critical aperture time that marks the boundary between the realms where either IMU or GPS errors dominate, this calculated for fixed error limits as

$$T_a = \frac{2\varepsilon_{pos}}{\varepsilon_{vel}} \ . \tag{E10}$$

For the typical error parameters given above, this critical aperture time is about 5 seconds.

This limitation can be expanded in terms of other parameters as

$$\frac{R}{\rho_a v_a} = \frac{4}{a_{wa}\lambda}\frac{\varepsilon_{pos}}{\varepsilon_{vel}} \ . \tag{E11}$$

This means that GPS limitations increase in significance when apertures are longer in time duration, as when

1. Resolutions are finer,
2. Velocities are slower,
3. Ranges are farther,

and IMU limitations increase in significance otherwise.

The SAR image azimuth location error is calculated from the synthetic aperture tilt angle error as

$$\varepsilon_x = R\sin(\phi) \approx R\,\phi \ . \tag{E12}$$

Synthetic Aperture Tilt Bounded by GPS

Where GPS errors dominate, that is, where position errors dominate, the expected azimuth target location error is

$$\varepsilon_{x,pos} \approx \frac{4\rho_a}{a_{wa}\lambda}\varepsilon_{pos} \ . \tag{E13}$$

This is true for synthetic aperture durations greater than the critical aperture time. Note that this error is proportional to resolution but independent of range.

Aperture Tilt Bounded by IMU

Where IMU errors dominate, that is, where velocity errors dominate, the expected azimuth target location error is

$$\varepsilon_{x,\mathrm{vel}} \approx \frac{R}{v_a}\varepsilon_{vel} \ . \tag{E14}$$

This is true for synthetic aperture durations less than the critical aperture time. Note that this error is proportional to range but independent of resolution.

Example

For nominal conditions where

$$\lambda = 0.018 \text{ m},$$
$$a_{wa} = 1.1822,$$
$$\rho_a = 0.3048 \text{ m},$$
$$v_a = 100 \text{ m/s},$$
$$R = 15 \text{ km},$$
$$\varepsilon_{pos} = 5 \text{ cm, and}$$
$$\varepsilon_{vel} = 2 \text{ cm/s}, \qquad \text{(E15)}$$

we note that the actual synthetic aperture duration is 5.24 seconds, whereas the critical aperture time is 5.0 seconds. Consequently we would expect the GPS error constraints to dominate.

We calculate the RMS azimuth location error due to GPS constraints as 2.9 m, and the RMS azimuth location error due to IMU drift as 3.0 m. Note that the GPS constraint is less, as predicted.

Comments

We now offer some general comments.

- The expected RMS error is taken here as the lesser of the errors due to GPS constraints, and IMU drift. We stipulate that there is probably a more intelligent way to combine these.
- The calculated azimuth location error does not account for own-ship position error.
- The analysis herein does not account for squint angles. We comment that imaging at a non-broadside squint angle has the effect of reducing the effective velocity, as the velocity v_a herein is assumed to be a tangential (cross-range component) velocity of the radar.
- There is no accommodation herein for layover effects due to inadequate target height information, which can be significant at non-broadside imaging geometries.
- The analysis herein does not account for any atmospheric refraction effects.
- Beyond the critical aperture time, GPS accuracy dominates the target location accuracy. In this realm the target location error does not depend on range, but does depend on resolution.
- The results herein are to first order consistent with Fig. 17 in the paper by Kim, et al.[1]

“Fast is fine, but accuracy is everything.”
-- Wyatt Earp

Appendix F – Some Useful Fourier Transform Pairs

There are many sources in the literature for Fourier Transform Pairs. We define the Fourier Transform herein as

$$X(f) = \int_{-\infty}^{\infty} x(t)\, e^{-j2\pi ft} dt \tag{E1}$$

and the Inverse Fourier Transform as

$$x(t) = \int_{-\infty}^{\infty} X(f)\, e^{j2\pi ft} df\,. \tag{E2}$$

The notation identifying a transform pair is

$$x(t) \Leftrightarrow X(f). \tag{E3}$$

We also note that Power Spectral Density $S(f)$ is related to Autocorrelation $R(t)$ as

$$R(t) \Leftrightarrow S(f). \tag{E4}$$

Of special interest to this report are the following transform pairs

$$\delta(t) \Leftrightarrow 1 \quad \text{(PSD of white noise)}, \tag{E5}$$

$$-\frac{\gamma + \mathrm{Ln}(|t|)}{\pi} \Leftrightarrow \frac{1}{|2\pi f|} \quad \text{(PSD of pink noise, or flicker noise)}, \tag{E6}$$

where γ = Euler's Constant Gamma, $\gamma \approx 0.5772$, and

$$\frac{-|t|}{2} \Leftrightarrow \frac{1}{(2\pi f)^2} \quad \text{(PSD of red noise, or Brownian noise)}. \tag{E7}$$

“Always live up to your standards - by lowering them, if necessary.”
-- Mignon McLaughlin, The Second Neurotic's Notebook, 1966

Appendix G – Unit Conversions

Linear Measures

1 inch = 0.0254 m

Acceleration Measures

1 g ≈ 9.8 m/s^2

1 μg ≈ 9.8 x 10^{-6} m/s^2

Angular Measures

1 rad. = $180/\pi$ deg. ≈ 57.3 deg.

1 deg. = 60 min. = 3600 arcsec.

Angular Rate Measures

1 $^\circ/h$ = π/648000 rad/s ≈ 4.85 x 10^{-6} rad/s

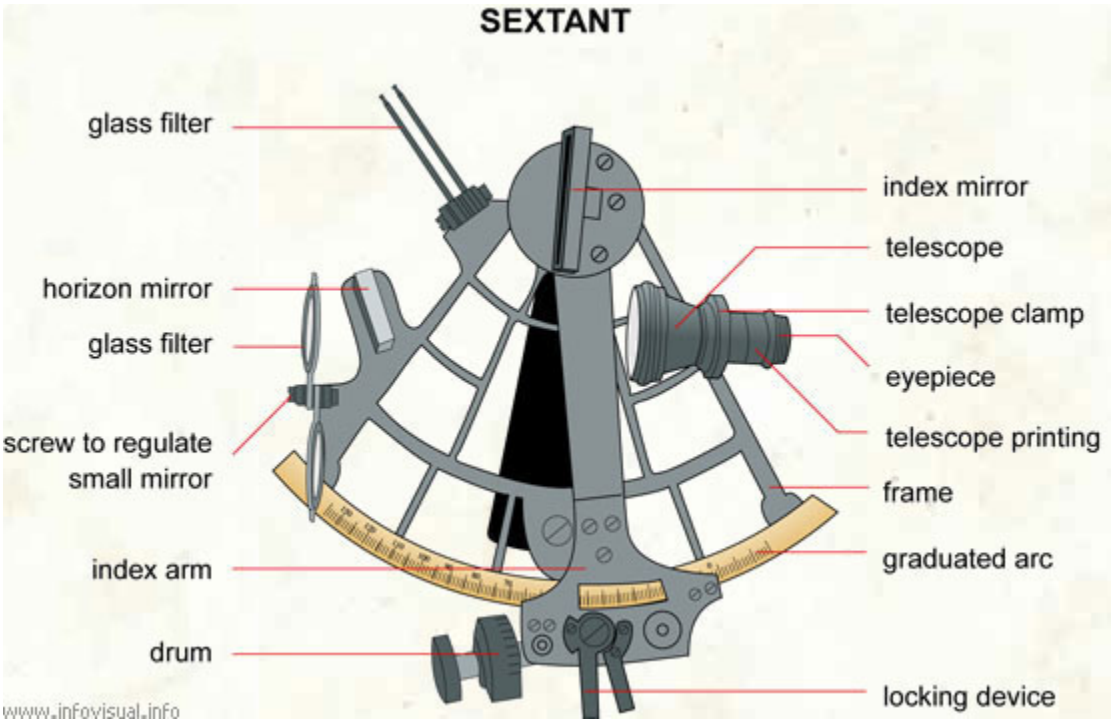

Figure 33. The sextant is an historic instrument used to facilitate celestial navigation. (Image courtesy *The Visual Dictionary*, http://www.infovisual.info/)

References

[1] Theodore J. Kim, J. Rick Fellerhoff, Stewart M. Kohler, "An Integrated Navigation System Using GPS Carrier Phase for Real-Time Airborne Synthetic Aperture Radar (SAR)," *Navigation*, Vol. 48, no. 1, 2001.

[2] Oliver J. Woodman, "An introduction to inertial navigation," Technical Report, Number 696, UCAM-CL-TR-696, ISSN 1476-2986, University of Cambridge Computer Laboratory, August 2007.

[3] Morris M. Kuritsky, Murray S. Goldstein, "Inertial Navigation," *Proceedings of the IEEE*, Vol. 71, No. 10, pp. 1156-1176, October 1983.

[4] D. H. Titterton, J. L. Weston, *Strapdown Inertial Navigation Technology (Progress in Astronautics and Aeronautics)*, second edition, ISBN 1-56347-693-2, American Institute of Aeronautics & Astronautics (AIAA), 2005.

[5] Christian Hirt, Sten Claessens, Thomas Fecher, Michael Kuhn, Roland Pail, Moritz Rexer1, "New ultrahigh-resolution picture of Earth's gravity field," Geophysical Research Letters, Vol. 40, pp. 4279–4283, doi:10.1002/grl.50838, August 2013.

[6] "HG 9900 IMU," data sheet, Honeywell International, Inc., 2004.

[7] "LN-200 FOG Family," data sheet, Northrop Grumman Systems Corporation, 2013.

[8] "HG1700 Inertial Measurement Unit," data sheet, Honeywell Aerospace, 2012.

[9] "HG1900 Inertial Measurement Unit," data sheet, Honeywell Aerospace, 2012.

[10] "HG1930 Inertial Measurement Unit," data sheet, Honeywell Aerospace, 2012.

[11] George A. Pavlath, "Development of Inertial-Grade Fiber Gyros," AIAA-1995-3231, American Institute of Aeronautics and Astronautics (AIAA) Guidance, Navigation and Control Conference, pp. 536-540, Baltimore, MD, Aug 7-10, 1995.

[12] Anthony Lawrence, *Modern Inertial Technology, Navigation, Guidance, and Control*, second edition, ISBN 0-387-98507-7, Springer-Verlag, 1998.

[13] Warren S. Flenniken IV, Hohn H. Wall, David M. Bevly, "Characterization of Various IMU Error Sources and the Effect on Navigation Performance," *Proceedings of the 2005 ION GNSS Conference*, Long Beach, CA ,13-16 September 2005.

[14] Warren S. Flenniken IV, *Modeling Inertial Measurement Units and Analyzing the Effect of their Errors in Navigation Applications*, Master's Thesis, Auburn University, December 16, 2005.

[15] Joseph M. Strus, Michael Kirkpatrick, James W. Sinko, "GPS/IMU Development of a High Accuracy Pointing System for Maneuvering Platforms," *Inside GNSS Magazine*, pp 30-37, March/April 2008.

[16] Joseph M. Strus, Michael Kirkpatrick, James W. Sinko, "Development of a High Accuracy Pointing System for Maneuvering Platforms," Proceedings of the ION GNSS International Technical Meeting of the Satellite Division, pp. 2541-2549, Fort Worth, TX, 25-28 September 2007.

[17] Warren S. Flenniken, Christopher Hamm, Final Report to Dan Lawrence – Phase IV Systems, Inc., Auburn University Mechanical Engineering Department, GPS & Vehicle Dynamics Laboratory, March 26, 2004.

[18] "IMU User's Manual," Revision B, Document 7430-0003-03, Crossbow Technology, Inc., February 2007.

[19] Kevin J. Walchko, Paul A. C. Mason, "Inertial Navigation," Proceedings of the 2002 Florida Conference on Recent Advances in Robotics, 2002.

[20] George M. Siouris, *Aerospace Avionics Systems*, ISBN 0-12-646890-7, Academic Press, Inc., 1993.

[21] Elliott D. Kaplan, Christopher J. Hegarty, *Understanding GPS Principles and Applications*, second edition, ISBN 978-1-58053-894-7, Artech House, Inc., 2006.

[22] Mohinder S. Grewal, Lawrence R. Weill, Angus P. Andrews, *Global Positioning Systems, Inertial Navigation, and Integration* – second edition, ISBN-13 978-0-470-04190-1, John Wiley & Sons, Inc., 2007.

[23] Cao Fuxiang, Bao Zheng, "Analysis and Simulation of GPS/SINU Integrated System for Airborne SAR Motion Compensation," Proceedings of the 2001 CIE International Conference on Radar, pp. 1173-1177, Beijing, China, 15-18 October 2001.

[24] Thomas A. Kennedy, "The Design of SAR Motion Compensation Systems Incorporating Strapdown Inertial Measurement Units," Proceedings of the 1988 IEEE National Radar Conference, pp. 74-78, Ann Arbor, MI, USA, 20-21 April 1988.

[25] Thomas A. Kennedy, "Strapdown Inertial Measurement Units for Motion Compensation for Synthetic Aperture Radars," *IEEE AES Magazine*, Vol. 3, Issue 10, pp. 32-35, October 1988.

[26] Armin W. Doerry, "Estimating IMU Heading Error from SAR Images," Sandia Report SAND2009-0183, Unlimited Release, March 2009.

[27] Brandeis Marquette, John Miller, J. Doug Jordan, Ted Kim, Armin Doerry, "SAR Image Feedback for Improved Inertial Measurement Unit Alignment," Proceedings of the 2010 IEEE Radar Conference, pp. 684-688, Crystal Gateway Marriott, Washington DC, USA, May 10 -14, 2010.

[28] Armin W. Doerry, Volker Horndt, Douglas L. Bickel, Richard M. Naething, "Estimating Radar Velocity using Direction of Arrival Measurements," Sandia Report SAND2014-17277, Unlimited Release, September 2014.

[29] Fred M. Dickey, Armin W. Doerry, Louis A. Romero, "Degrading effects of the lower atmosphere on long range airborne SAR imaging," *IET Proceedings on Radar, Sonar & Navigation*, Vol. 1, No. 5, pp. 329–339, October 2007.

[30] Armin W. Doerry, "Radar Range Measurements in the Atmosphere," Sandia National Laboratories Report SAND2013-1096, Unlimited Release, February 2013.

[31] Armin W. Doerry, "Anatomy of a SAR Impulse Response," Sandia report SAND2007-5042, Unlimited Release, August 2007.

[32] C. V. Jakowatz Jr., D. E. Wahl, P. H. Eichel, D. C. Ghiglia, P. A. Thompson, *Spotlight-Mode Synthetic Aperture Radar: A Signal Processing Approach*, ISBN 0-7923-9677-4, Kluwer Academic Publishers, 1996.

[33] B. L. Burns, J. T. Cordaro, "SAR image formation algorithm that compensates for the spatially variant effects of antenna motion," SPIE Proceedings, Vol 2230, SPIE's International Symposium on Optical Engineering in Aerospace Sensing, Orlando, 4-8 April 1994.

[34] Armin W. Doerry, "Autofocus Correction of Excessive Migration in Synthetic Aperture Radar Images," Sandia Report SAND2004-4770, September 2004.

[35] A. Doerry, "Autofocus correction of SAR images exhibiting excessive residual migration," SPIE 2005 Defense & Security Symposium, Radar Sensor Technology X, Vol. 5788, Orlando FL, 28 March - 1 April 2005.

[36] John C. Kirk, Jr., Russ Lefevre, Randy van Daalen Wetters, Don Woods, Brendan Sullivan, "Signal Based Motion Compensation (SBMC)," The Record of the IEEE 2000 International Radar Conference, pp. 463-468, 7-12 May 2000.

[37] Armin W. Doerry, "Ship Dynamics for Maritime ISAR Imaging," Sandia Report SAND2008-1020, Unlimited Release, February 2008.

[38] A. W. Doerry, "What maritime ISAR designers should know about ship dynamics," SPIE 2012 Defense, Security & Sensing Symposium, Radar Sensor Technology XVI, Vol. 8361, Baltimore MD, 23-27 April 2012.

[39] Armin W. Doerry, "Automatic Compensation of Antenna Beam Roll-off in SAR Images," Sandia Report SAND2006-2632, Unlimited Release, April 2006.

[40] R. H. Graham, D. L. Bickel, W. H. Hensley, "The Rapid Terrain Visualization Interferometric Synthetic Aperture Radar Sensor," SPIE 2003 Optics & Photonics Symposium, Earth Observing Systems VIII, Vol. 5151, pp. 106-115, San Diego, California, USA, 3 August 2003.

[41] D. J. Kozakoff, *Analysis of Radome-Enclosed Antennas*, 2nd Ed., (U) Artech House, Boston, MA, 2010.

[42] Armin W. Doerry, "Earth Curvature and Atmospheric Refraction Effects on Radar Signal Propagation," Sandia Report SAND2012-10690, Unlimited Release, January 2013.

[43] Armin W. Doerry, "Radar Range Measurements in the Atmosphere", Sandia National Laboratories Report SAND2013-1096, Unlimited Release, February 2013.

[44] Armin W. Doerry, "Just Where Exactly is the Radar? (a.k.a. The Radar Antenna Phase Center)," Sandia National Laboratories Report SAND2013-10635, Unlimited Release, December 2013.

[45] Alison K. Brown, "Test Results of a GPS/Inertial Navigation System using a Low Cost MEMS IMU," Proceedings of 11th Annual Saint Petersburg International Conference on Integrated Navigation System, Saint Petersburg, Russia, May 2004.

[46] D. N. Pedlar, D. J. Coe, "Target geolocation using SAR," *IEE Proceedings on Radar, Sonar, and Navigigation*, Vol. 152, No. 1, pp. 35-42, February 2005.

[47] M. Denny, I. Scott, "Anomalous Propagation Limitations to High-Resolution SAR Performance," Proceedings of the 2002 IEEE Radar Conference, Long Beach, CA, USA, p. 249-254, 22-25 April 2002.

[48] IEEE Std 952-1997, "Guide and Test Procedure for Single Axis Interferometric Fiber Optic Gyros," IEEE, p.63, 1997.

[49] Naser El-Sheimy, Haiying Hou, Xiaoji Niu, "Analysis and Modeling of Inertial Sensors Using Allan Variance," *IEEE Transactions on Instrumentation and Measurement*, Vol. 57, No. 1, pp. 140-149, January 2008.

[50] Lawrence C. Ng, Darryll J. Pines, "Characterization of Ring Laser Gyro Performance Using the Allan Variance Method," *Journal of Guidance, Control, and Dynamics*, American Institute of Aeronautics and Astronautics, Vol. 20, No. 1, pp. 211-214, 1997.

[51] J. A. Barnes, D. W. Allen, "A Statistical Model of Flicker Noise," *Proceedings of the IEEE*, Vol. 54, No. 2, pp 176-178, February 1966.

[52] Armin W. Doerry, "Anatomy of a SAR Impulse Response," Sandia report SAND2007-5042, Unlimited Release, August 2007.

[53] T. T. Taylor, "Design of Line-Source Antenna for Narrow Beamwidth and Low Side Lobes," *IRE Transactions - Antenna and Propagation*, p. 16, January, 1955.

[54] Armin W. Doerry, *Synthetic Aperture Radar Processing with Tiered Subapertures*, Ph.D. Dissertation, University of New Mexico, Albuquerque, New Mexico, May, 1995.

Distribution

Unlimited Release

1	MS 0519	J. A. Ruffner	5349	
1	MS 0519	A. W. Doerry	5349	
1	MS 0519	L. Klein	5349	
1	MS 0532	J. J. Hudgens	5240	
1	MS 0899	Technical Library	9536	(electronic copy)


Sandia National Laboratories